OPTOFLUIDIC PHOTONIC CRYSTAL PLATFORM FOR LABEL-FREE DETECTION AND GAS SENSING

by

SHULING WANG

Presented to the Faculty of the Graduate School of

The University of Texas at Arlington in Partial Fulfillment

of the Requirements

for the Degree of

DOCTOR OF PHILOSOPHY

THE UNIVERSITY OF TEXAS AT ARLINGTON

May 2016

Acknowledgements

It would be not possible for me to complete this dissertation without the help and guidance of those people who have offered their valuable assistance and insight generously during my Ph.D. study. First and foremost, I would like to express my greatest gratitude to my academic supervisor, Professor Yuze (Alice) Sun, for her instruction, inspiration, and support on my journey of Ph.D. study. Her knowledge, critical insights, and stringent scientific methods helped me overcome various difficulties in the projects I worked on and finish this dissertation finally. I cannot express enough thank for her consistence patience and generous time supervising me through my research.

I would also like to thank other members of my doctoral committee: Professor Yi Hong, Professor Robert Magnusson, Professor Michael Vasilyev, and Professor Weidong Zhou, for their interest and useful suggestions for my work included in this dissertation. I wish to thank my graduate advisor Dr. William E. Dillon for his tireless advices and suggestions in the past six years.

I would like to gratefully acknowledge our collaborator, Professor Weidong Zhou, for the remarkable collaboration on photonic crystal simulation and fabrication, as well as providing characterization system. I would like to express my special thanks to Dr. Deyin Zhao for his work on the sensor design and simulation. I appreciate his useful advices when I got hard time in my study. I am fortunate enough to be shared with him from research to life. Thanks to Yonghao Liu and Shihchia Liu for their work on the fabrication. I am indebted to Yonghao Liu for his contribution on device fabrication. Thanks to Dr. Hongjun Yang for his discussions on the characterization system.

I acknowledge Department of Electrical Engineering in University of Texas at Arlington (UTA) for bestowing me with the STEM scholarship. I thank to the staffs in the department, Terri Earle, Ann Lewiston, Janice Moore, Pauline Mason, and Gail Paniuski for their help. I also thank to Nanotechnology Research Center in UTA and Microelectronics Research Center in University of Texas at Austin for the facilities and support they provided. I am grateful for the funding support from National Science Foundation program. Without the sponsorship, nothing could have happened in my research.

I would like to express my heartfelt thanks to all my friends in Arlington who made my time here funny and memorable, from working at late nights in the lab, hanging out during weekends, to celebrating festivals. The true friendship is the treasure that I would like to own and appreciate forever.

Lastly but most importantly, I wish to express my deepest gratitude to my family for their unconditional love and support during the journey of my life. I thank them for having a strong faith in me to pursue the higher education in United States. I would have not made it so far without their love, care, and inspiration.

March 28, 2016

Abstract

OPTOFLUIDIC PHOTONIC CRYSTAL PLATFORM

FOR LABEL-FREE DETECTION

AND GAS SENSING

Shuling Wang, PhD

The University of Texas at Arlington, 2016

Supervising Professor: Yuze (Alice) Sun

Photonic crystals (PhCs) based label-free sensing technology has great potential as a highly sensitive, high-throughput, and compact that has vast applications in biomedical research, healthcare, pharmaceuticals, environmental security, and battlefield to detect target analytes in either liquid or vapor phase. The PhC refers to a heterogeneous structure composed of a periodic arrangement of low-loss dielectric materials with contrasting refractive index (RI). Such a structure constrains the light propagation in certain ways such that the optical properties of the PhC are particularly sensitive to changes in RI, which in turn makes them useful for sensing purposes, since the interaction of target analytes with light causes the change of local RI.

Most of the studies reported so far involved micro-cavities into PhCs to achieve high quality factor, and hence better sensing performance. The in-plane light coupling method associated with micro-cavities increased the alignment challenge and made it difficult for system miniaturization. To meet this challenge, two-dimensional (2D)

photonic crystal slab (PCS) is studied in this dissertation. In 2D PCS, light can be confined to in-plane guided modes by the higher RI dielectric material without coupling to externally incident beam, or can be confined to guided resonance modes in the slab where coupling to externally incident beam is allowed. Fano resonance in 2D PCS arises from the coupling of in-plane guided resonance modes above the light line to the out-of-the-plane radiation modes due to phase-matching provided by the periodic lattice structure. It is promising to employ Fano resonance in 2D PCS for sensing applications, since it provides an efficient way to channel light from within the slab to the external environment. Furthermore, Fano resonance results in asymmetric Fano lineshape in the reflection and transmission spectrum, featuring a sharp peak-to-dip transition in contrast to the conventional symmetric Lorentzian lineshape in other resonance sensors. This sharp transition in Fano lineshape is advantageous for extracting small spectral shift induced from small RI change, hence, more sensitive detection can be achieved.

For bulk liquid sensing, both single-layer and coupled double-layer PCS are simulated using Fourier modal method (FMM) and finite-difference time-domain (FDTD) method, which provides guidelines for future sensor design. And then the optofluidic sensing platform based on both single-layer and coupled double-layer PCS is built and the sensor performance is characterized with various concentrations of ethanol/deionized water mixture using surface normal measurement system.

In the chemical vapor detection, PCS vapor sensing platform is developed by coating vapor sensitive polymer onto PCS surface. The interaction between polymer and vapor analytes results in the polymer thickness and/or RI change, which leads to Fano resonance spectral shift. The capability of vapor sensing is demonstrated with

representative vapor analytes, and the detection specificity is realized by coating PCS with different vapor absorbing polymers. Moreover, theoretical analysis using FMM and FDTD method is performed which gives guidelines to optimize the future designs of the PCS based vapor sensor.

Table of Contents

List of Illustrations

List of Tables

Chapter 1

Introduction

1.1 Motivation

In the past decades, optical biomedical and chemical sensors have received extensive investigation, which is to a large extent driven by its vast applications in biomedical research, healthcare, pharmaceuticals, environmental monitoring, homeland security, and battlefield.[1-7] Optical detection techniques have a number of distinctive advantages, such as immune to electromagnetic interference, capable of performing remote sensing and multiplexing sensing within a single chip. In general, there are two sensing protocols employed in optical sensing: label-based sensing and label-free sensing. In label-based sensing, either target molecules or biorecognition molecules are labeled with fluorescent tags or radioactive molecules, such as dyes[8]; the intensity of fluorescent or radioactive signal indicates the presence of target molecules as well as the interaction strength between target and biorecognition molecules. Although label-based sensing is extremely sensitive[9] and some sensing techniques have already been commercialized with high throughput, there are several potential problems associated with the labels. For example, prior knowledge on the target's presence has to be known, and the target molecules have to be modified in order to incorporate the labels which is a laborious process and may change or inhibit the functionality of the molecules under investigation, and thus making it unsuitable for certain in vivo applications. Furthermore, quantitative analysis is difficult due to the unpredictability of the fluorescence efficiency and the inability of acquiring kinetics information from an assay. In contrast, in label-free sensing, target molecules are not labeled and light interrogates the analyte in noninvasive

way.[10] They usually measure the physical properties of the target analyte, such as mass, polarization, dielectric permittivity, and conductivity. The label-free sensor works as a transducer which converts one of these physical properties into a quantifiable signal that can be measured by an instrument (such as a photodetector). Label-free sensing is cost-efficient and easy to perform, and allows for quantitative and kinetic analysis of analytes. Although still in formative stage, optical label-free sensing technology possesses unique and advantageous properties over the state-of-the-art, emerging as a promising sensing technology.

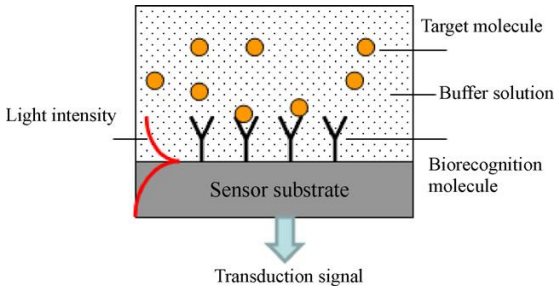

Figure 1-1 Conceptual illustration of an optical label-free sensor.[4]

Optical label-free sensors can be implemented through a variety of signal transduction pathways based on photonic attributes that include absorbance, transmission, polarization, reflectivity, refractive index (RI), and Raman scattering. In particular, RI based sensors are popular, become fast-paced technology for biological and chemical analysis in recent years, and can realize with diversely optical structures, such as surface plasmon resonance (SPR)[11-16], interferometers[4, 17-19], waveguide[20], optical fibers[21], metallic nanohole-array based resonance[22], photonic crystals (PhCs)[23, 24], ring resonators[25-28], and so on. As illustrated in Figure 1-1, RI based sensors can measure the RI change of bulk solution and the RI change induced from analytes binding

on the surface; thus it is particularly attractive for those applications with ultra-small detection volume as RI sensing signal scales with the analyte bulk concentration or surface density, rather than with the total amount of analyte.

The most widely used structure for label-free sensing is SPR, which has been commercialized by Biacore.[29] As illustrated in Figure 1-2(a), a typical SPR sensor is composed of a dielectric prism with a thin-layer of metal coating on the top surface.[30] When light is incident onto the dielectric/metal interface at a particular angle, it can cause a bound electromagnetic mode on the metal's surface, provided the k-vector of this mode is matched to that of the incident light. This phenomenon is known as SPR. As a result of surface plasmon excitation, the reflection spectrum for light propagating through the prism exhibits a dip, which will shift in wavelength when there is a RI change happened near the surface of metal, as shown in Figure 1-2(b).[30] As a kind of label-free sensors, SPR sensors can measure RI changes occurring at the surface of metal film that supports surface plasmon. A change in RI of the dielectric gives rise to a change in the propagation constant of the surface plasmon, which through the coupling condition alters the characteristics of the light wave coupled to the surface plasmon, such as coupling angle, coupling wavelength, intensity, and phase. Therefore, several detection approaches have been used in SPR sensors, including measurement of the intensity of optical wave near resonance[12], angular[13] and wavelength[14] interrogation, as well as exploration of polarization[15] and phase[16] change associated with SPR. SPR sensors are very sensitive, with the bulk RI sensitivity as large as 10^3 nm/RIU (refractive index unit).[31] However, owing to strong absorption in the metal film, the SPR resonance mode is very broad, as a result of low quality (Q) factor (a few hundred), which restricts its detection

limit (DL) and precludes its use for applications that require detection of very small molecules.

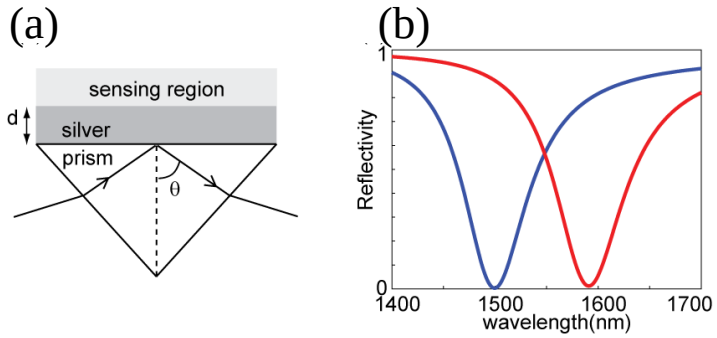

Figure 1-2 (a) Schematic of a SPR sensor. (b) Reflectivity spectra when the index perturbation $\Delta n = 0.001$ is absent (blue) and present (red). The index change is applied to the sensing region (assumed to be air) above the silver film.[30]

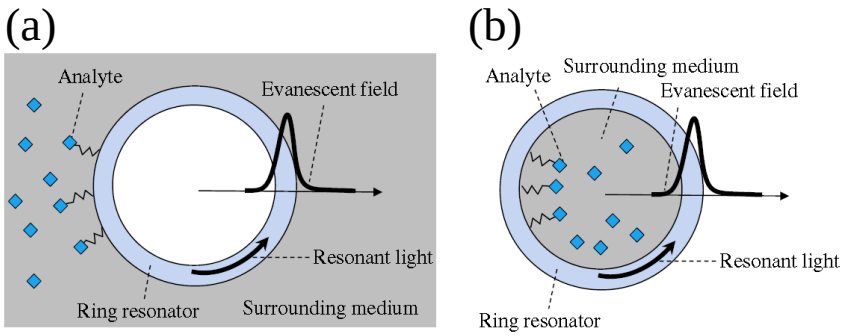

Figure 1-3 Conceptual illustrations of an optical ring resonator sensor. The resonant light circulates along the resonator and its evanescent field is present in the surrounding medium outside (a) or inside (b) the ring resonator, interacting with the analyte on the ring resonator exterior surface (a) or interior surface (b) and in the surrounding medium.[25]

A key to achieve better DL is to narrow the linewidth of optical resonance, *i.e.*, achieving high Q factor. Optical ring resonators based on whispering gallery mode (WGM) have been under extensive investigation as label-free sensing technology, owing to the extremely high Q factor. A ring resonator consists of an optical waveguide in ring geometry, placed closely to a standard channel waveguide. Light passing through the channel waveguide can couple into the ring at wavelengths that are exact integers of the optical path length of the ring, which produces a dip in the transmission spectrum of the channel waveguide at resonant wavelengths. The WGM modes circulate along the ring resonator and have an evanescent field that reaches several hundred nanometers into the surrounding medium and can interact with the analyte near the resonator surface, which is illustrated in Figure 1-3.[25] In contrast to the traditional linear waveguide sensors in which the light-analyte interaction length is the physical length of the sensor, the effective light-analyte interaction length in a ring resonator sensor is no longer determined by the sensor's physical size but rather by the number of revolutions of the light supported by the resonator, owing to the circulating nature of WGM modes. Ring resonators demonstrate extremely high Q factor, ranging from 10^4 to 10^8 which depends on the configurations of the ring resonators.[25-28] Thus, despite the small physical size, ring resonators have an effective length of a few tens of centimeters or even longer, which leads to better sensing performance with smaller footprint. However, a problem associated with ring resonators is that the light is strongly confined by the ring and only a small portion of the optical mode can interact with the analyte, which renders a relatively low sensitivity (a few nm/RIU) and hence restricts the DL.[32]

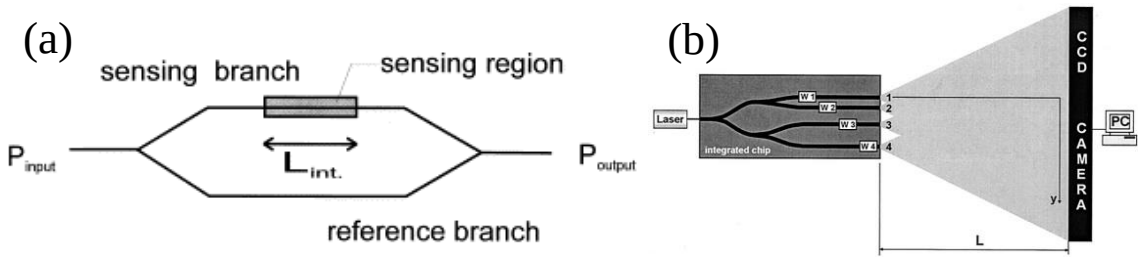

Figure 1-4 Conceptual illustrations of interferometer sensors. (a) Mach-Zehnder interferometer sensor.[18] (b) Multi-channel Young's interferometer sensor.[19]

Interferometer based sensors measure the optical path length change caused by the local RI change. Two popular configurations of interferometer sensors are Mach-Zehnder and Young's interferometers, which are illustrated in Figure 1-4.[18, 19] They usually are composed of two arms, one reference arm and one sensing arm. Coherent, single frequency, single polarization light from a laser source enters the input waveguide and is split equally at the Y-junction. The sensing arm has a window allowing the evanescent field of that branch to interact with the analyte, while the reference arm is protected from the sample. Light from two arms will recombine at the output waveguide, resulting in interference, and a photodetector is used to measure light intensity. Once the local RI of the sensing arm is changed due to analyte binding, the optical path length in this branch will change, which in turn leads to interference pattern change, and hence change of light intensity collected by the photodetector. Interferometer based optical sensors are very sensitive, and a DL of 10^{-7} RIU has been achieved.[19] However, in order to introduce sufficient optical path length difference to achieve small DL, the required length of interferometer device is quite long, around a few centimeters. In addition, since it needs two channel to generate interference, reference channel and

sensing channel, it is hard to do multiplexing sensing with multiple channels. Heideman *et al.* achieved four-channel Young interferometer sensor[19], but it is hard to design multi-channel beyond it.

During the same period, it has also seen the fast advance in microfluidics, which could enable small volume sample handling for performing automated and parallel functions such as particle sorting and separation, cell culturing and concentration gradient formation within the same miniaturized and planar platform, promoting the development of lab-on-a-chip technology.[33] Modern advances in both optics and microfluidics have led to the emergence of optofluidics, which is defined as the "integration" or "marriage" of photonic and microfluidic architectures and can provide enhanced performance and novel functionalities within the same miniaturized system.[34, 35] This innovation of optofluidics is the result of high degree integration, miniaturization, and growing interest in cross-disciplinary research and applications.[36-38]

An optofluidic device consists of photonic structure and microfluidic component on a single chip; microfluidics is designed to handle and control the fluid (gaseous or liquid) media, and optical structure is used to control light. Optofluidics is not merely the adding of microfluidic device to optical structure, but rather the synergistic integration of them, resulting in smart microsystems that can enable new applications in biological and chemical analysis with several advantages. Firstly, it is compatible with nanotechnology and biology. Different materials can be explored and different surface treatment can be implemented to increase the biocompatibility of the materials. Secondly, microfluidic component can be easily fabricated with soft lithography and combined with photonic structure for different applications. Also, microfluidic component is usually made with

materials that are transparent to light, like polydimethylsiloxane (PDMS), making it well suitable for optical detection. Finally, optofluidics can be ultra-compact and portable, resulting in the further development of lab-on-a-chip technology and potential applications in a wide range of fields, like point-of-care diagnostics and drug discovery.

As a class of optical nanostructures, PhCs can be easily integrated with microfluidic channel for developing ultra-compact, miniaturized, and on-chip optofluidic sensor arrays with high throughput. Most of the studies reported so far involved micro-cavities into PhCs to achieve high Q factor, and hence better sensing performance.[24] The in-plane light coupling method associated with micro-cavities increased the alignment challenge and made it difficult for system miniaturization. In this dissertation, we will develop a Fano resonance photonic crystal slab (PCS) based optofluidic label-free sensing platform which makes use of guided resonances in PCS to couple light from in-plane to free space.[39] We will show that, with Fano resonance PCS, the sensor characterization system is much simplified. We will explore the bulk liquid sensing and chemical vapor detection with Fano resonance PCS.

1.2 Organization of this dissertation

This dissertation includes seven chapters and is organized as follows.

In chapter 1, an introduction of optical label-free sensing as well as the motivation for developing optofluidic PhCs label-free sensing platform are presented.

Chapter 2 gives an overview of PhCs based label-free sensors, including one-dimensional (1D), two-dimensional (2D), and three-dimensional (3D) PhCs. It also introduces a particular kind of PhCs, 2D PCS, which possesses Fano resonance

associating with unique asymmetric lineshape and is advantageous for label-free sensing to other optical structures with Lorentzian lineshape.

Chapter 3 focuses on the design and numerical study of 2D PCS biosensors, including single-layer PCS and coupled double-layer PCS. Fourier modal method (FMM) and finite-difference time-domain (FDTD) method are introduced for computing the reflection spectrum and modal field distribution of PCS, respectively. The metrics for evaluating PCS sensor performance are discussed. The lattice parameters that affect the sensing performance of single-layer PCS are studied and the underlying physics is given. The theoretical background of coupled double-layer PCS is presented, and the principle for achieving high Q factor with it is discussed. Numerical study of coupled double-layer PCS sensor is performed, and the guidelines for optimizing its performance are discussed.

In chapter 4, the fabrication technologies for building optofluidic PCS sensing platform are presented. The PCS is fabricated with electron-beam lithography (EBL) and reactive-ion etching (RIE) process, and microfluidic channel is made with soft lithography. Such simple fabrication process with low cost and high yield makes it possible for mass-production and scaling up to an array format for multiplexed detection.

In chapter 5, the experimental characterization of both single-layer and coupled double-layer PCS for bulk liquid sensing is studied. And discussion of key sensing metrics, like Q factor, sensitivity, and DL is performed. Experimental results are compared with numerical results to confirm its accuracy. And comparison between single-layer and coupled double-layer PCS sensor is presented too.

Chapter 6 is dedicated to the study of PCS for chemical vapor detection. The vapor sensing mechanism is presented, and sensitivity of both single-layer and coupled

double-layer PCS vapor sensors are evaluated with representative vapor analytes. Selective detection of vapor analytes with different polymer coatings is investigated. Theoretical study is also performed to further understand the sensing principle and the sensing capability of PCS sensor.

Chapter 7 concludes this dissertation and proposes outlook towards future research directions.

Chapter 2

Overview of Photonic Crystal Based Label-free Biosensors

2.1 Introduction of photonic crystals (PhCs)

PhCs are structures in which the dielectric constant, *i.e.*, RI, is modulated periodically within wavelength scale in one, two or three directions.[40-43] They are called 1D, 2D, and 3D PhCs, as shown in Figure 2-1(a)-(c), respectively. For 1D PhCs, they are consisted of two materials with different RI that are alternating only in one direction. One example of 1D PhCs is the distributed Bragg reflector which is widely used in the conventional vertical cavity surface emitting lasers. In 2D PhCs, the materials are modulated in two directions, while there is no change in the third direction. 2D PhCs can be realized by drilling holes with hexagonal or square symmetry in a high RI material or by stacking cylinders of any dielectric material in air. 3D PhCs are structures in which the RI is varied in all the three directions of space, such as an inverse opal structure and spheres in a diamond lattice, as shown in Figure 2-1(c).

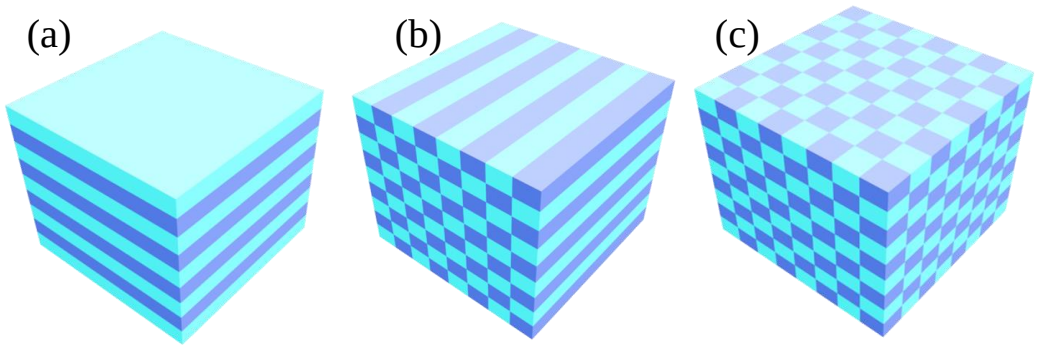

Figure 2-1 Schematic illustrations of (a) 1D, (b) 2D, (c) 3D PhCs.[43]

Traditionally, the control of photons has relied on total internal reflection (TIR). Light propagating in a high dielectric material is reflected at the interface with a low

dielectric material. This severely limits the degree of miniaturization of optical components since the interface has to be smooth with respect to light wavelength. PhCs provide a completely different mechanism for the manipulation of light. When light is incident onto PhCs, a certain wavelength of incident light is reflected depending on the period and effective RI of the structure. The reflection peak will be associated with a transmission trough and the wavelength at which happens is called the photonic stop band or pseudo band gap wavelength. When the stop band is seen for all directions of propagation and for both polarization states of light, this forbidden band in transmission is referred to as a complete photonic band gap (PBG).[43] A PhC could be designed to possess a complete PBG, *i.e.*, a range of wavelengths which is not allowed to propagate through the PhC unless there is a defect in the perfect structure. The defect could lead to localized photonic states in the gap whose shapes and properties would be dictated by the nature of the defect. A point defect could act like a micro-cavity, a line defect like a waveguide, and a planar defect like a perfect mirror. The capability of PhCs to manipulate a photon offers us with a new dimension in our ability to control the properties of light, and therein lies the exciting applications.

Through active research in the last two decades, owing to the unique light manipulation capability in nano-scale to sub-micron scale dimension, PhCs have been widely explored for developing novel, compact and integrated optical devices, such as lasers, mirrors, filters, switches, modulators, and sensors.[24, 44-46] By doping active materials such as dyes or quantum dots into a PhC with defect, low threshold laser can be achieved when the defect mode wavelength of the PhC and the emission wavelength of active medium match.[47, 48] 2D PhCs could be designed as mirror with broadband

reflectivity or filter with high Q factor, depending on the coupling strength between in-plane guided resonance modes and free-space radiation modes, which can be adjusted through engineering the lattice geometry.[46, 49, 50] With point or line defect, local electrical field of PhCs can be significantly enhanced, resulting in strong light-matter interaction, and hence high sensitivity.[24]

2.2 Overview of PhCs based label-free biosensors

In the past decades, optical biomedical and chemical sensors have received extensive investigation, which is to a large extent driven by the vast applications in biomedical research, healthcare, pharmaceuticals, environmental monitoring, homeland security and the battlefield, as well as its unique properties, such as immune to electromagnetic interference, capable of performing remote sensing and multiplexing sensing within a single chip. The detection is used to rely on labels or tags[8], *e.g.*, fluorescent materials, which may substantially alter the structure or function of the analyte. Thus, optical label-free sensing in which light can interrogate the analyte in noninvasive way becomes more promising as a highly sensitive, high-throughput, compact and easy to use technology.[4, 51] Optical label-free sensors are implemented through a variety of signal transduction pathways based on photonic attributes that include absorption, polarization, RI, and scattering. In particular, RI based sensors can measure the RI change of bulk solution and that induced from analyte binding on the surface, hence it is especially attractive for those applications with ultra-small detection volume as RI sensing signal scales with the bulk concentration or surface density, rather than with the total amount of the analyte. In addition, it allows for quantitative and

kinetic analysis of the analyte in real-time. A variety of optical structures have been proposed and demonstrated for label-free RI sensing, as described in chapter 1.

Owing to the unique light confinement and coupling method as well as enhanced light-matter interaction in nano-scale to sub-micron scale dimension, PhCs are highly attractive for developing ultra-compact on-chip integrated sensor arrays.[24, 45] Since PhCs are defined by repeating RI contrast, their optical properties are particularly sensitive to changes in RI, and thus making them promising for sensing applications. Usually there is an optical resonance mode associated with the reflection and transmission spectrum of PhCs. When there is a small change in RI of the medium surrounding the PhCs, like the binding of small biochemical molecules onto PhCs surface, the frequency of the optical mode shifts. The shift of the optical mode frequency from local RI change can be calculated by applying the perturbation theory[24]:

$$\frac{\Delta\omega}{\omega} \cong -\frac{1}{2}\frac{\int d^3\mathbf{r}\Delta\varepsilon(\mathbf{r})|\mathbf{E}(\mathbf{r})|^2}{\int d^3\mathbf{r}\varepsilon(\mathbf{r})|\mathbf{E}(\mathbf{r})|^2}$$

$$\cong -\frac{\Delta n}{n}\cdot\left(\text{fraction of } \int \varepsilon|\mathbf{E}|^2 \text{ in perturbed region}\right) \quad (2.1)$$

Equation (2.1) indicates that the frequency change of optical mode in PhCs depends on both local RI change and the fractional portion of electric field energy in the RI perturbed region. Thus, by monitoring the optical mode frequency of PhCs in real-time, the quantitative and kinetic analysis of the analyte can be realized.

As a new label-free sensing technology, PhCs offer a number of distinctive advantages. Firstly, in PhCs light can be concentrated in micrometer dimension, and thus achieving strong light-matter interaction within volume down to femtoliters. With enhanced local field, PhCs could render better sensing performance with smaller footprint

and less amount of analyte. Secondly, the planar geometry, small footprint, and simple fabrication with high yield make it easily scaled into multiplexed sensing arrays for parallel detection. Also, the ultra-compact nature and easily integration with microfluidic channel and other optical components can be implemented for many lab-on-a-chip sensing applications.

2.2.1 One-dimensional PhCs biosensors

1D PhCs have two kinds of configurations, vertically stacked multiple dielectric layers with different RI and 1D planar gratings, as shown in Figure 2-2.[52-59] They can be easily fabricated and scaled up to an array format for multiplexed detection. For 1D PhCs with multiple dielectric layers, when introducing defect layer at appropriate position of the structure, PhCs can have a very large portion of evanescent field extending outside the structure, resulting in strong light-matter interaction, and hence pretty large sensitivity ($>10^3$ nm/RIU).[52] Despite the Q factor is moderate (10^2 - 10^3), the DL can be as low as 10^{-8} RIU thanks to extremely high sensitivity.[52] Since the filling fraction outside the PCS is very large, 1D PhCs with multiple dielectric layers can be not only useful for detecting small biomolecules, but also suitable for detection of multilayered biomolecular interactions.

1D planar gratings are also known as guided-mode resonance (GMR) sensors, in which the resonant leaky mode can be excited by an incident optical wave.[57, 59, 60] GMR theory was first proposed by Professor Robert Magnusson in The University of Texas at Arlington. In 1D planar grating structure, the input light can be efficiently reflected in a narrow spectral band whose central wavelength is highly sensitive to chemical reactions occurring at the surface of the structure. Professor Magnusson and his

student suggested the application of the GMR effect for label-free sensing application in 1992, and invented highly accurate biosensors with GMR grating which are being commercialized in ResonantSensors.[61] As a kind of label-free sensors, 1D gratings show good sensitivity, simplified light coupling method, and compatibility with plastic substrates.

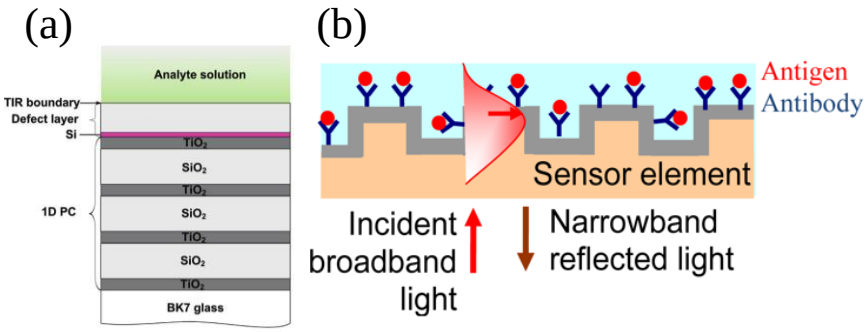

Figure 2-2 Configurations of 1D PhCs sensors. (a) PhCs with multiple dielectric layers.[52] (b) 1D planar gratings.[57]

2.2.2 Two-dimensional PhCs biosensors

2.2.2.1 Two-dimensional PhCs with defect cavity

One of the main advantages of PhCs is their ability to control the dispersion of light. By introducing defects into the lattice, high Q factor cavities can be formed within nano-scale to sub-micron scale dimension. Such small size cavity is advantageous over the larger cavities, as the analyte consumption is much reduced and it also allows for the multiplexing of many sensor arrays on chip. Slow light effect can also be engineered in PhCs by altering the dispersion curve of the device through deformation in the lattice, which can reduce the group velocity significantly, resulting in enhanced light-matter interaction.[62, 63] With defect cavity and slow light effect, the amount of time and light-

matter interaction can be increased a lot, which leads to higher Q factor and larger sensitivity, and hence better DL.

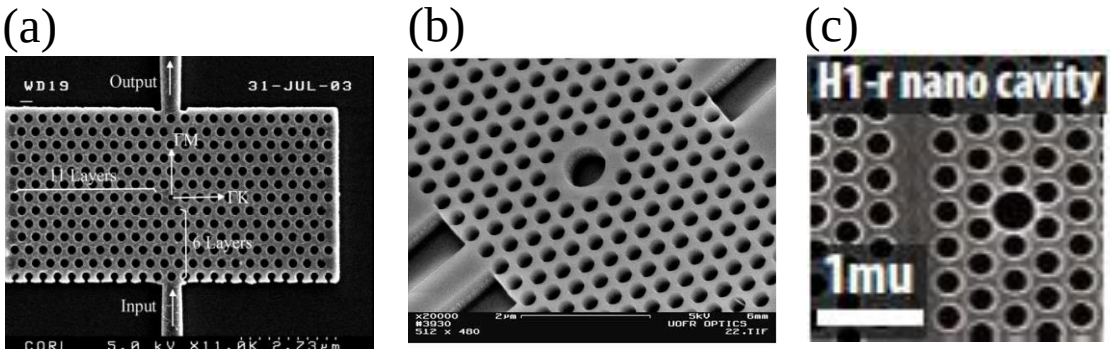

Figure 2-3 PhCs with point defect micro-cavity. (a) PhC micro-cavity with integrated rigid waveguides. Point defect has smaller radius than regular holes.[64] (b) PhC micro-cavity with tapered rigid waveguides. Point defect has larger radius than regular holes.[65] (c) Point defect cavity in the vicinity of PhC waveguide.[66]

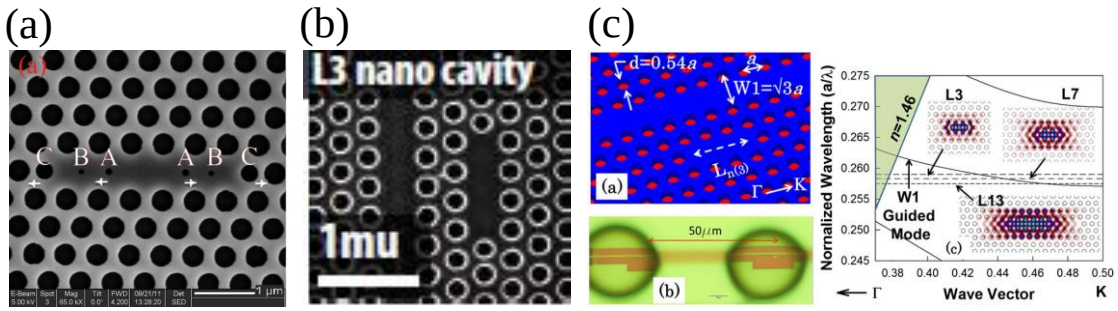

Figure 2-4 PhCs with L-type defect micro-cavity. (a) L7 cavity with mini air holes.[67] (b) L3 defect in the vicinity of the PhC waveguide.[66] (c) L3, L7, L13 PhCs micro-cavities.[68]

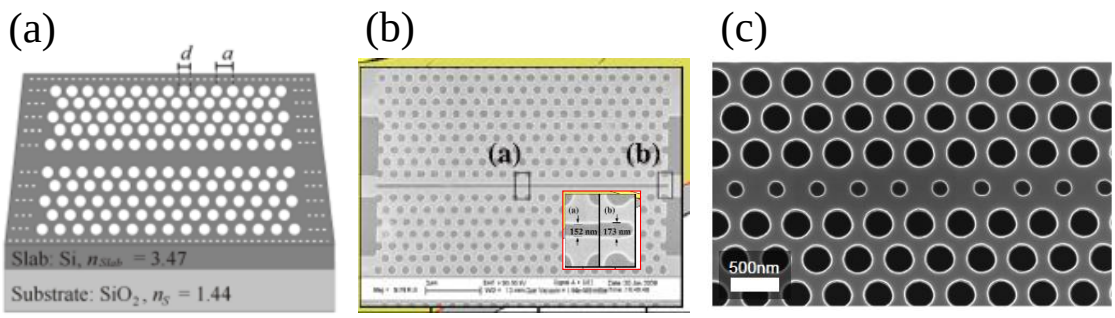

Figure 2-5 PhCs with waveuide. (a) PhC waveguide configuration.[69] (b) PhC waveguide with an air slot.[70] (c) Modified PhC waveguide with a row of holes.[71]

To date, there is a variety of 2D PhCs micro-cavity architectures that has been studied for label-free sensing, including PhCs with point defect, L-type defect, and line defect (waveguide), as illustrated in Figure 2-3, Figure 2-4, and Figure 2-5, respectively.[24, 45, 62-81] PhCs with point defect micro-cavity are created by introducing an enlarged or reduced air hole into the periodic lattice. The enlarged or reduced air hole gives rise to a defect state in the measured transmission spectrum. Fauchet *et al*. have demonstrated a PhC micro-cavity with an enlarged air hole for single particle detection, which exhibits a Q factor of around 2,000.[65] Ruda *et al.* have fabricated a heterogeneous Si pillar-array micro-cavity, from which a high Q factor of 2.7×10^4 and a bulk RI sensitivity of 350 nm/RIU were achieved.[80] PhCs sensors with such point defect micro-cavity can achieve extremely small DL and are capable of detecting single particle/molecule. Furthermore, metrics such as particle/molecule size can be quantitatively measured.[65] The main challenge with it is the delivery of target analytes to the sensing region.

To achieve better sensing performance, *i.e.*, smaller DL, both high Q factor and high sensitivity are preferable.[32] However, these two requirements are contradictory in guided-wave optics; since the optical mode should be strongly confined in the structure to achieve a high Q factor, and strong overlap of optical field with the analyte is required to have high sensitivity. Most of the PhCs sensors demonstrated so far have either high Q factor[68] or high sensitivity[64]. Thus, tradeoffs between light confinement and the spatial overlap have to be considered in the design of PhCs based label-free sensors. For example, in PhCs with point defect micro-cavity, if the defect hole is very small, the optical modes can be tightly confined at the cavity region which results in very high Q factor, while the portion of evanescent light existing outside the cavity is small, as a result of small overlap between analyte and optical modal field, and thus small sensitivity. In contrast, if the defect hole is very large, the light confinement is reduced which decreases the Q factor; but the overlap between light and the analyte is increased, resulting in strong light-matter interaction and thus high sensitivity. To overcome the above limitations, L-type cavities and their modifications are investigated, in which several air holes are missing along Γ-K direction in the periodic structure. With L-type micro-cavities, the optical modal field can be strongly confined within the cavity region, as a result of high Q factor. By introducing mini air holes into cavity region, the overlap between analytes and modal field is improved, resulting in enhanced light-matter interaction, and hence higher sensitivity.[67, 81]

PhCs waveguides have also been studied for label-free sensing owing to the large sensing area it offered compared to other cavity based sensors, although the Q factor is quite low. To further increase the sensitivity, Evoy *et al.* introduced a row of air holes

into the waveguide to increase the sensing area, and thus higher sensitivity.[71] Krauss *et al.* have designed a slotted waveguide which demonstrated both high Q factor and high sensitivity.[70]

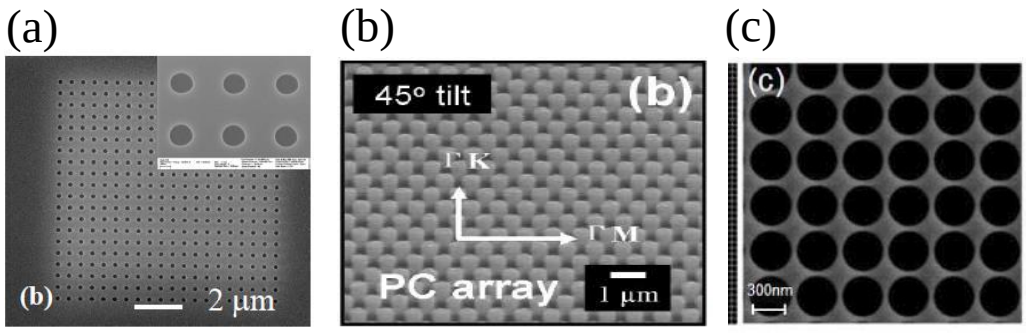

Figure 2-6 Cavity free PhCs. (a) Cavity free SiN_x PhC on dielectric substrate.[82] (b) TiO_2 nanopillar PhC.[83] (c) Suspended SiN_x PhC.[84]

2.2.2.2 Cavity free two-dimensional PhCs

Although PhCs micro-cavities have demonstrated excellent sensing performance through the engineering of defect and slow light effect, the delicate alignment schemes required for coupling light from free space to in-plane waveguide make it difficult for system miniaturization and scaling up into multiplexed sensor arrays for lab-on-a-chip applications. Cavity free PhCs, *i.e.*, PCSs, have also been investigated for label-free sensing applications, due to its easily fabrication and characterization with surface normal setup. Configurations of PCS sensors are shown in Figure 2-6.[82-86] PCS relies on the guided resonance to coupling light from in-plane to free space, and is usually characterized at normal incidence. Harris *et al.* have demonstrated the feasibility of cavity free PhC for label-free sensing, although the sensor performance is not as good as that of PhCs with micro-cavities.[82] To improve the sensing performance, Altug *et al.*

implemented the “flow-through” scheme to enhance the sensitivity.[84] As shown in Figure 2-7(a), in the “flow-through” scheme, the nanoholes to form PhC label-free sensor serve as nanofluidic channels for analyte to flow through. Compared to traditional “flow-over” scheme used in most of label-free sensors, mass transport rate in “flow-through” scheme has been improved by 6-14-fold.[87] Moreover, light-matter interaction has been enhanced owing to the effective analyte delivery to the sensor surface through active flow, and thus sensitivity has been improved. By employing nano-scale openings in optical structure as nanofluidics, it demonstrates the excellent integration of nanophotonics with nanofluidics on the same platform. However, fabrication of such suspended PhCs nanomembrane is challenging. The integrity and mechanical strength of suspended nanomembrane need to be worked out, since it is subject to relatively high pressure gradients for driving analytes through.

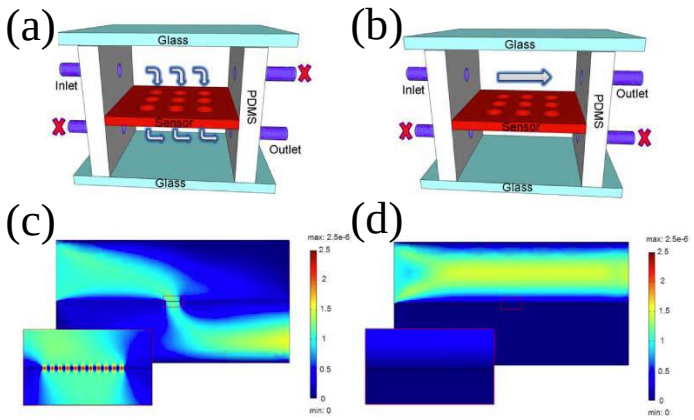

Figure 2-7 (a) Illustration of the actively controlled flow scheme. Solution directed to the structure surface goes through the nano-scale hole arrays and flows to the bottom channel. The nanohole arrays are used as sensing structures as well as nanofluidic channels. (b) Conventional (passively controlled) flow scheme is illustrated. Convective flow stream passes over the surface of the sensor. (c)-(d) Velocity distribution of solutions are calculated by solving the Navier-Stokes equations for actively and passively controlled flow scheme. Insets show the distribution around the nanohole arrays in detail.[84]

In contrast to conventional homogeneous PCS (HPCS), Levi *et al.* designed "*checkerboard*" PCS (CPCS) in which light is coupled to slightly perturbed dark modes through alternating nanohole sizes, as illustrated in Figure 2-8(b).[85] By alternating the nanohole radius in the lattice, small perturbation to existing dark modes has been introduced, as a result that these dark modes are "band-folded" into the light-cone, as shown in Figure 2-8(c). These new modes show extraordinary high Q factor compared to guided resonance modes in the HPCS, and the sensitivity is improved too. The combined Q factor and sensitivity enhancement drastically improves the DL with respect to

conventional HPCS structure. Both high Q factor (10,600) and high sensitivity (>800 nm/RIU) are achieved experimentally with this CPCS structure.

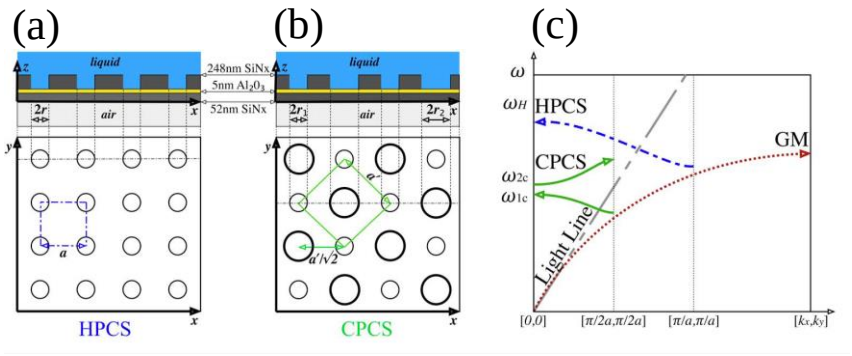

Figure 2-8 (a) Geometry of HPCS reduced unit cell (bounded by the blue dashed line). (b) Geometry of CPCS reduced unit cell (bounded by the green solid line), with lattice constant a' and the inter-hole distance $a'/2^{1/2}$. (c) Schematic description of CPCS (solid green line), and HPCS (dashed blue line) band-folding starting from a dielectric substrate guided mode (dotted red line) into HPCS GR at $[k_x,k_y] = [\pi/a, \pi/a]$ and into CPCS GR at $[k_x,k_y] = [\pi/2a, \pi/2a]$. In panel (c), we have set inter-hole distance of HPCS and CPCS to be the same, resulting in a ratio of $a'/a = 2^{1/2}$ for the lattice constants of CPCS and HPCS. The nano-hole radii are $r_1 = r-\Delta r/2$ and $r_2 = r + \Delta r/2$ for small Δr.[85]

2.2.3 Three-dimensional PhCs biosensors

Colloidally templated 3D PhCs (*e.g.*, opal or inverse opal as demonstrated) have been explored for biosensing applications.[88-93] With femtosecond laser exposure at optimized focusing depth, 3D PhCs can be created inside fused silica.[93] Phased-tunable multi-level diffractive optical elements have been used to define 3D PhCs in a "woodpile" configuration for sensing.[92] 3D PhCs sensors demonstrate very large RI sensitivity due to the relatively large overlap between optical modal field and the analytes. Other

advantages of 3D PhCs sensors include enabling many types of materials to be incorporated into the structure, and involving many different sensing mechanisms (*e.g.*, RI change and polymer swelling). However, fabricating 3D PhCs has still been a challenge since they tend to have complex 3D connectivity and strict alignment requirements.

2.3 Two-dimensional photonic crystal slab (2D PCS)

2D PCS is a particularly important class of PhCs. A 2D PCS is consisted of a two-dimensionally periodic index contrast introduced into a high RI guiding layer. As shown in Figure 2-9(a), 2D PCS is quasi-3D structure in which the light confinement is arising from the in-plane 2D PBG confinement and vertical waveguide index confinement (through the TIR principle).[43, 94] Compared to other PhCs, the perfect uniformity of 2D PCS makes it more amenable to fabricate using current microfabrication technology with high yield, while they offer much similar functionality. A typical dispersion plot is shown in Figure 2-9(b).[39, 95] The light core region is formed due to the vertical confinement. These structures support in-plane guided modes below the light line, which are completely confined by the slab without any coupling to external radiation.[94] In addition to in-plane wave guiding, 2D PCS can also interact with external radiation in complex and interesting ways. When the light is confined into guided resonance modes in the slab, it can be coupled to the external radiation modes due to phase-matching provided by the periodic lattice structure.[39, 96] Thus, 2D PCS offers an efficient way to channel light from within the slab to the external environment, which is very appealing for many applications, such as laser, sensor, etc.

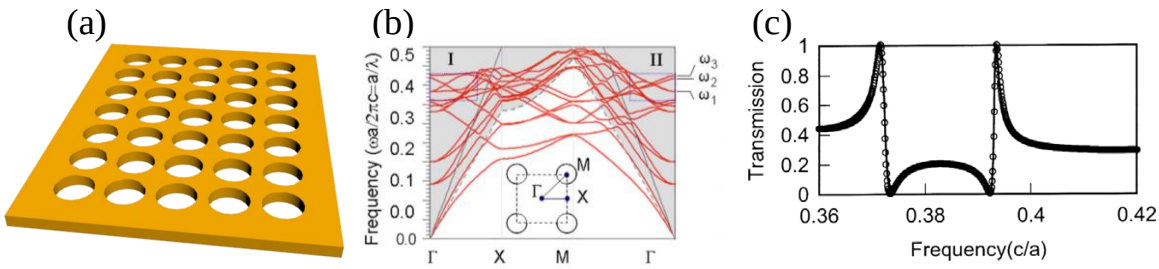

Figure 2-9 2D PCS: (a) Schematic representation of square lattice PCS. (b) Simulated dispersion characteristics for the square lattice Si PCS on low index glass substrate. The lattice parameters are r/a = 0.19, t/a = 0.417, the refractive indices of Si and glass are 3.48 and 1.5, respectively. (c) The intensity transmission spectrum through such a 2D PCS, with lattice parameters, r/a = 0.2, t/a = 0.5.[46]

2.3.1 Photonic band structures

The PhC refers to a heterogeneous structure composed of a periodic arrangement of low-loss dielectric materials with contrasting RI. When light is incident onto the PhC, the constructive and destructive interference resulting from various reflection and refraction of photons within the contrasting materials produce a phenomenon known as photonic bands.[80] A photonic band is a continuous range of light frequencies or wavelengths (of a particular polarization, propagating in a particular direction) that can pass through the PhC. And the PBG is a range of frequencies or wavelengths of light that cannot pass through the PhC (when propagating in a particular direction with a particular polarization). Photons with frequencies in the bandgap range are reflected by the material and only can penetrate the PhC evanescently.

Photonic band structures of PhCs can be explained with Maxwell's equations. In SI units, they are:

$$\nabla \cdot \mathbf{B} = 0 \qquad \nabla \times \mathbf{E} = -\frac{\partial \mathbf{B}}{\partial t} \tag{2.2a}$$

$$\nabla \cdot \mathbf{D} = \rho \qquad \nabla \times \mathbf{H} = \frac{\partial \mathbf{D}}{\partial t} + \mathbf{J} \tag{2.2b}$$

where ρ and **J** are the free charge and current densities, and **E**, **D**, **B**, and **H** are the electric, displacement, magnetic induction, and magnetic fields, respectively. All six variables depend on both time and position. For dielectric materials that are non-magnetic, non-dispersive, linear, and isotropic, the electric fields **E** & **D** as well as magnetic fields **H** & **B** are related through the constitutive relations:

$$\mathbf{D} = \varepsilon \varepsilon_0 \mathbf{E} \tag{2.3a}$$

$$\mathbf{B} = \mu_0 \mathbf{H} \tag{2.3b}$$

where ε is the dielectric function (of time and position) and ε_0 & μ_0 are the permittivity and permeability constants of free space. Combining equation (2.2) and (2.3), and with the assumption of harmonic time-dependence for the fields at any given frequency, we can derive the wave equation for PhCs:

$$\nabla \times \left(\frac{1}{\varepsilon(\mathbf{r})} \nabla \times \mathbf{H}(\mathbf{r}) \right) = \left(\frac{\omega}{c} \right)^2 \mathbf{H}(\mathbf{r}) \tag{2.4a}$$

$$\mathbf{E}(\mathbf{r}) = \frac{i}{\omega \varepsilon_0 \varepsilon(r)} \nabla \times \mathbf{H}(\mathbf{r}) \tag{2.4b}$$

where ω is the angular frequency of propagating light. The distribution of magnetic field within a PhC is entirely determined by the solutions of equation (2.4a), and electric field can be calculated with equation (2.4b).

The photonic band structures of PhCs follow from the solutions of equation (2.4a). It is an eigenvalue equation, and depending on $\varepsilon(\mathbf{r})$, both discrete solutions and bands of solutions may exist. When equation (2.4a) can be satisfied over a continuous range of

frequencies, a photonic band exists. A PBG is a continuous range of frequencies for which equation (2.4a) does not have a solution (for the given $\varepsilon(\mathbf{r})$). A discrete solution to equation (2.4a), corresponding to a specific isolated frequency, represents a confined optical cavity state at that frequency within a PBG. Unfortunately, equation (2.4) cannot be solved analytically for practical PhCs, thus researchers rely on numerical (computational) modeling to make predictions about the behaviors of PhCs. A typical dispersion plot or band diagram of a 2D PCS is shown in Figure 2-9(b).

2.3.2 Fano resonance in 2D PCS

Fano resonance, known from atomic physics, arises from the constructive and destructive interference of discrete resonance states by broadband continuum states.[97] First observed from the transmission spectra of gratings, Fano resonance is responsible for a variety of Wood's anomalies.[98] This phenomenon and the underlying mechanism, being common and ubiquitous in many realms of physical sciences, are found in many nanophotonic structures, such as quantum dots, PhCs, plasmonics, and metamaterials.[39, 99, 100] Unlike conventional symmetric-shaped Lorentzian resonance, Fano resonance possesses asymmetric line profile,[97, 99] which originates from a close coexistence of resonant transmission and resonant reflection, and can be reduced to the interaction of a discrete (localized) state with a continuum of propagation modes. The sharp dip-to-peak transition of Fano resonance promises its applicability in a wide range of photonic devices, such as optical filters, switches, sensors, detectors, etc.

In 2D PCS, light can be confined to in-plane guided modes by the higher RI dielectric material (through the TIR principle).[94] In addition to in-plane wave guiding, PCS can also interact with external radiation modes in complex and interesting ways. Of

particular importance is the presence of guided resonance.[39, 96] Similar to guided mode, guided resonance can be strongly confined within the slab. Unlike guided mode, guided resonance can couple with the external radiation modes.[39] Thus guided resonance provides an efficient way to channel light from within the slab to the external environment. Moreover, guided resonance can significantly affect the transmission and reflection of external incident light, resulting in complex resonant line shapes which can be linked to Fano resonance.[39, 101] When light incidences onto PCS from out of the plane direction (*e.g.*, surface normal direction), there are two pathways for energy transportation. The first pathway is a direct transmission process, where a portion of the incident energy goes straight through the slab and generates the initial pulse. The second pathway is an indirect transmission process, where the remaining portion of the incident energy excites the guided resonance and subsequently leaks out to free space. Taking into consideration the interference between these two pathways, we express the transmitted amplitude *t* and the reflected amplitude *r* as follows[46]:

$$t = t_d + f\frac{\gamma}{i(\omega - \omega_0) + \gamma} \tag{2.5a}$$

$$r = r_d \pm f\frac{\gamma}{i(\omega - \omega_0) + \gamma} \tag{2.5b}$$

where t_d and r_d are the direct transmission and reflection coefficients, ω_0 and γ are the center frequency and width of the resonance, and the factor *f* is the complex amplitude of the resonant mode. The plus and minus sign in equation (2.5b) correspond to even and odd resonant modes with respect to the mirror plane parallel to the slab. For $0 < |t_d| < 1$, equation (2.5a) gives a Fano lineshape with sharp dip-to-peak transition. For example, the intensity transmission spectrum of a PCS with a square lattice of air holes introduced into

a dielectric slab (Figure 2-9(a)) is shown in Figure 2-9(c), which exhibits Fano resonance lineshapes with asymmetric profiles.[39, 95]

Fano resonance in 2D PCS arises from the coupling of in-plane guided resonance modes above the light line to the out-of-the-plane radiation modes due to phase-matching provided by the periodic lattice structure. It is very appealing to employ Fano resonance for sensing applications since it provides an efficient and easy way to channel light from in-plane to free space. Furthermore, the asymmetric Fano lineshape in the reflection and transmission spectrum of 2D PCS is advantageous for extracting small spectral shift induced from small RI change around the slab, and thus better DL can be achieved.

2.4 Conclusion

In this chapter, a detailed introduction to PhCs based lable-free sensing platform is given. As shown above, the unique light manipulation capability of PhCs in nano-scale to sub-micron scale dimension makes it promising for developing highly sensitive, high-throughput, and compact sensor arrays. In particular, 2D PCS possesses Fano resonance with asymmetric lineshape and have great potential for building label-free biosensors with excellent performance that will be studied in detail in the following chapters.

Chapter 3

Design of Label-free Fano Resonance 2D PCS Sensors

3.1 Computational method

There is a variety of general purpose tools available for computational electromagnetic, such as the FDTD method, finite-difference frequency-domain (FDFD) method[102], FMM[103], and the finite element method (FEM)[104], that can be adapted to simulate 3D structures with 2D periodicity. Typically for 2D PCS structures, there are two widely used approaches for the simulation of the transmission and reflection properties, as well as modal field distribution, FMM and 3D FDTD method. We will discuss FMM and FDTD method in detail for the simulation of 2D PCS.

3.1.1 Fourier modal method

FMM is an electromagnetic propagation solver that is specifically adapted to solve layered 3D structures that are periodic in the plane of layering. There are two implementations of FMM, rigorous coupled wave analysis (RCWA)[105] and Stanford Stratified Structure Solver (S^4) software package[106]. RCWA utilizes a state-variable method that converges with the proper solution without inherent numerical instabilities to obtain the exact solution of Maxwell's equations for the electromagnetic diffraction of grating structures. It is a relatively straightforward, non-iterative, and deterministic technique. The accuracy of solution obtained from RCWA depends solely on the number of terms in the field space-harmonic expansion, which ensures that the energy is always conserved.[105]

Another implementation of FMM is S^4, a freely available software package developed by Liu and Fan.[106] Compared to the commercial RCWA package GD-Calc,

the S^4 software package offers much higher resolution due to the consideration of higher diffraction orders and also takes much less computation time.[106] Throughout this dissertation, we use the FMM based S^4 software package to compute the reflection spectrum through the slab, Q factor, and the spectral sensitivity ($\Delta\lambda/\Delta n$) by tracking shifts in Fano resonance frequency.

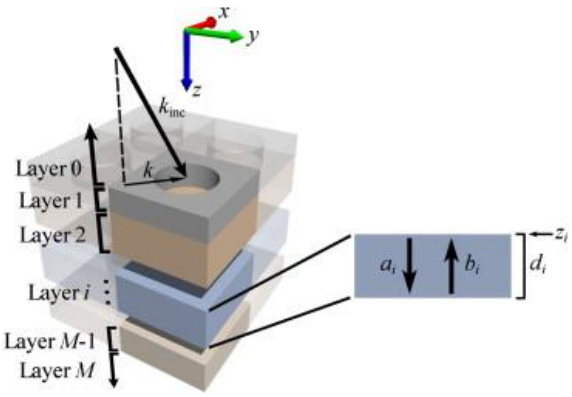

Figure 3-1 Left: schematic of the problem formulation for a stack of layers. A single square unit cell is highlighted among the four shown. The incident radiation is assumed to be a plane wave with wave vector $\mathbf{k}_{inc}$, and its projection into the *xy* plane is $\mathbf{k}$. Right: schematic for the cross section of layer *i*. The arrows indicate the propagation directions of forward and backward layer modes.[106]

In this method, the structure is modeled as a unit cell that is periodic in the *x* and *y* directions and aperiodic in the *z*-direction, as shown in Figure 3-1. This is exactly the case for the PCS structures studied in this dissertation. The eigenmodes that are appropriate to each layer are determined by considering a corresponding infinite structure, which has the same dielectric profile in the *xy* plane, but is uniform and infinite in the *z*-direction. In such a corresponding infinite structure, the electrical field distribution of the eigenmodes can be expressed by equation[107]:

$$\mathbf{u}_{n,m}(\mathbf{r}, z) = \sum_{\mathbf{G}} \mathbf{u}_{n,m}(\mathbf{G}) e^{i(\mathbf{k}+\mathbf{G})\cdot\mathbf{r}} e^{iq_{n,m}z} \quad (3.1)$$

Here, $\mathbf{r}$ = (x, y) is the position vector and $\mathbf{k}$ = (k_x, k_y) is the in-plane wave vector for the incident wave. The summation is conducted over all reciprocal lattice vectors, **G'**s. The subscripts n and m label the m^{th} mode for the n^{th} layer. Both $\mathbf{u}_{n,m}(\mathbf{G})$ and the square of longitudinal wave vectors, *i.e.*, $q_{n,m}^2$, correspond to the m^{th} eigenmode and eigenvalue of an N_G x N_G matrix, obtained by representing Maxwell's equations in a plane wave basis. N_G is the number of plane waves used. Using the eigenmodes as a basis, the field in the n^{th} layer can be expanded as[107]:

$$\mathbf{E}_n(\mathbf{G}, z) = \sum_{m} \mathbf{u}_{n,m}(\mathbf{G}) \left[a_{n,m} e^{iq_{n,m}z} + b_{n,m} e^{-iq_{n,m}z} \right] \quad (3.2)$$

The forward and backward wave mode amplitudes are $a_{n,m}$ and $b_{n,m}$, respectively. Suppose a plane wave is incident onto the structure from a region above. In this region, all incoming plane wave amplitudes are set to zero except for the actual incident wave. By matching boundary conditions at all interfaces, a linear system can be set up to determine all the *a* and *b* coefficients, and thus obtaining the field in the entire structures. It is noted that this procedure provides exact results for a dielectric function of a finite number of Fourier components.[107] This inherently stable computational technique permits the determination of sharp spectral features (Fano resonance) and rapid estimation of resonance frequencies as well as peak widths.

3.1.2 Finite-difference time-domain method

FDTD is one of the most common computational tools in classical electromagnetism, which divides space and time into a regular grid and simulates the time evolution of Maxwell's equations. The FDTD method employs a discretized form of

Maxwell's equations to propagate electromagnetic fields through a discretized space composed of building blocks known as Yee cells[108]. The Yee cell exists as a square in 2D space and as a cube in 3D space. The boundaries of these cells are treated as the discrete electric field components while the magnetic field components are normal to the faces. The method steps through discrete time and at each step the fields are updated according to fields of the neighboring cells at the previous time step.[102] With this method, fields are propagated through a discrete space in discrete time. FDTD is extremely versatile and puts little constraint on the type of geometry that can be simulated. At the same time computational requirements grow as a square function of the cell size in 2D space and cubic function in 3D space. Therefore high resolution requirements come with a large computational penalty. FDTD has advantages of simplicity, generality, and robustness. It is straightforward to implement the full time-dependent Maxwell's equations for nearly arbitrary materials (including nonlinear, anisotropic, dispersive, and time-varying materials) and a variety of boundary conditions.

Throughout this dissertation, we use Meep (an acronym for Massachusetts Institute of Technology Electromagnetic Equation Propagation)[109], a free, open-source implementation of the FDTD algorithm to compute the reflection and transmission spectrum as well as modal field distribution of 2D PCS to confirm the accuracy of results from FMM based S^4 software package. In this method, the computational domain includes a unit cell of the structure which is defined by using periodic boundary conditions (PBCs) and perfectly matched layers (PMLs), as illustrated in Figure 3-2.[39] PMLs are imposed on the top and bottom surfaces to absorb the outgoing field[110]. The concept of PML was initially formulated by Berrenger in 1994[110] and provides an

angle and frequency independent absorption. Bloch PBCs are applied to the four lateral *xz* and *yz* planes to emulate infinite planar periodicity, which is given by[39]:

$$\mathbf{E}(\mathbf{r}+\mathbf{a}) = e^{i(\mathbf{k}\cdot\mathbf{a})}\mathbf{E}(\mathbf{r}) \tag{3.3}$$

Here, **a** is the lattice vector of the square lattice and **k** is the wave vector that is parallel to the slab. It is noted that **k** is a conserved quantity in the scattering process by Bloch's theorem. To solve modes of the PCS, a Gaussian source is launched from the top of the PCS structure, with two power monitors monitoring both the reflected and transmitted power. Modal field distributions are calculated by exciting the PCS using a planar continuous-wave source also located above the PCS. We use Meep to calculate the instantaneous field energies and distributions, which are used to evaluate the sensing metrics that will be presented in section 3.2.

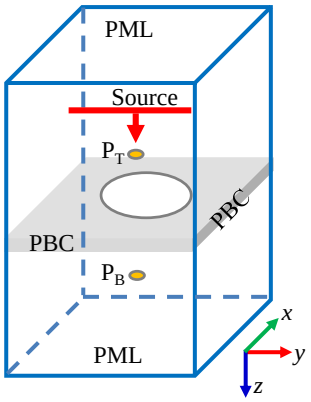

Figure 3-2 Schematic of a unit cell used in the simulation based on 3D FDTD technique. Bloch boundary conditions are imposed on the four surfaces perpendicular to the slab. The PML absorbing boundary conditions are imposed at the top and bottom surfaces. A plane of dipole sources generates the incident plane waves. The transmitted and reflected amplitudes are determined by recording the fields at the monitor points positioned at both sides of the structures.[39].

3.1.3 Methods comparison

Table 3-1: Comparison of FMM and FDTD method

Features	FMM	FDTD
Speed	Fast regardless of feature size	Very slow for sub-micron features
Resolution	Described by number of reciprocal lattice vectors	Described by number of Yee cells in computational space, cubic relationship between computation time and resolution
Discretization	Arbitrary, *i.e.*, fields can be calculated at any location in computational space	Limited by grid resolution
Field distribution	Limited to fields at cross sections of simulated structure	Very flexible, time-evolution of fields may be visualized, field in arbitrary regions calculated
Spectrum	Highly accurate, resolves high Q resonances	Limited to spectral width of source, vulnerable to numerical errors for high Q values
Design flexibility	Limited to uniform dielectric layers with in-plane periodicity	Flexible, any 3D feature can be implemented and simulated
Error source	Inherently stable, no significant artifact	Many, due to non-trivial source definitions, boundary conditions and dispersion-related issues

FDTD method is highly flexible and can implement any feature in 3D space. It can not only produce time-domain animations of field distribution, but also offer a built-in mode-solver to help determine true spectral locations of asymmetric Fano resonance

spectrum. The main drawback of FDTD method is the lack to accommodate approximations to simplify computations. Simulations need a lot of memory and computational overhead, as a result of long computation time, especially for high resolution. There is a cubic relationship between resolution and computation time in FDTD simulations. In comparison, FMM can compute high resolution spectrum with high accuracy in high speed (*e.g.*, a few minutes). However, FMM can only simulate structures of uniform dielectric layers with in-plane periodicity. More detailed comparison between FMM and FDTD method is listed in Table 3-1. In this dissertation, we use both FMM and FDTD method to study our PCS structure and affirm accurate results. We use S^4 package to compute the reflection spectrum as well as acquire sensitivity by tracking spectral shift ($\Delta\lambda/\Delta n$). Meep is used for simulation of the optical modal field distributions, and then the sensitivity is calculated based on perturbation theory (see discussion in section 3.2).

3.2 Sensitivity parameters of PCS sensors

The sensing mechanism of 2D PCS sensors is the detection of Fano resonance spectral shift caused from RI change of the medium surrounding PCS. As a method of label-free biosensing, the PCS surface may be coated with a thin layer of biorecognition molecules that bind specifically to an analyte (*e.g.*, antibodies with affinity to a specific protein, or streptavidin with an affinity to biotin). When excited at a Fano resonance frequency, the PCS will have significant electric field energy engulfing the biorecoginition layer. Assuming in an aqueous environment, such as in a microfluidic channel, the binding of analytes to the biorecognition layer will cause a change of the

local RI in that region. This RI change in turn leads to a detectable spectral shift of PCS Fano resonance.

The relationship between RI change of the surrounding medium and the shift of Fano resonance frequency is linear to the first order approximation. An important metric in quantifying such shift is the filling fraction or optical overlap integral *f*, which describes the ratio of electric field energy existing outside of a dielectric structure with the total at a given mode[111]:

$$f = \frac{\int_{liquid} d^3r\, n^2(r)\left|E_{k,m}(r)\right|^2}{\int_{\infty}\, d^3r\, n^2(r)\left|E_{k,m}(r)\right|^2} \tag{3.4}$$

The volume integral in the numerator of equation (3.4) gets contributions only from the liquid regions, where due to analytes binding there is a small perturbation, $\Delta\varepsilon$, to the otherwise linear and unperturbed dielectric function ε.[43] Assuming that $\Delta n/n$ is the same for all perturbed liquid regions and following the perturbation theory, bulk spectral sensitivity variable, *S* (nm/RIU), is defined as[111]:

$$S = \frac{\Delta\lambda}{\Delta n} = f\,\frac{\lambda_0}{n_{\text{liquid}}}\ \left[\frac{\text{nm}}{\text{RIU}}\right] \tag{3.5}$$

where Δn is RI change of surrounding medium, $\Delta\lambda$ is the spectral shift, and n_{liquid} is the liquid RI. Based on equations (3.4) and (3.5), it is indicated that a large *f* value implies a considerable electric field energy in locations outside the dielectric structure (*i.e.*, the PCS) available for sensing changes of RI. It is noted that the calculation assumes that a small perturbation in RI does not change the modal field distributions significantly. In addition to *S*, we define the sensor DL, which describes the smallest RI change that can be measured by a RI sensor[32]:

$$DL = \frac{R}{S} \propto \frac{1}{Q \times S} \text{ [RIU]} \tag{3.6}$$

where R is the spectral resolution. The spectral resolution depends on the spectral lineshape and the signal-to-noise ratio of experimental system. Since the spectral lineshape is related to Q factor (traditionally defined as $Q = \omega_0/\Delta\omega$), we can get that DL is inversely related to both Q factor and the sensitivity.

In label-free biosensing scenario, the biological analytes may have a wide range of RI values and only analytes localized onto the detection zone of the sensor can be detected, and thus the ability to detect small RI changes is of great importance for a biosensor. From equation (3.6), we know that, to achieve better DL, both high Q factor and high sensitivity are desired. For practical applications, a DL less than 10^{-4} RIU is applicable.

3.3 Design of 2D PCS sensors

3.3.1 Design of single-layer 2D PCS sensors

There are two kinds of PCS architectures that have been proposed for label-free sensing, symmetric one which refers to suspended PCS and asymmetric one which refers to PCS resting on a substrate, as shown in Figure 3-3.[86] Intuitively, the presence of a substrate in PCS design has an enormous bearing on the sensitivity compared to symmetric, suspended design, since the filling fraction *f* in asymmetric PCS architecture is much reduced due to substrate-incurred loss. However, suspended PCS increases fabrication challenges, and the fragility of suspended PCS membrane makes it unsuitable for many practical applications. In contrast, the asymmetric PCS implementation reduces the fabrication challenge significantly, and the detection zone can be as large as cm by

cm. Therefore, we only consider asymmetric PCS design on silicon-on-insulator (SOI) substrate in this dissertation.

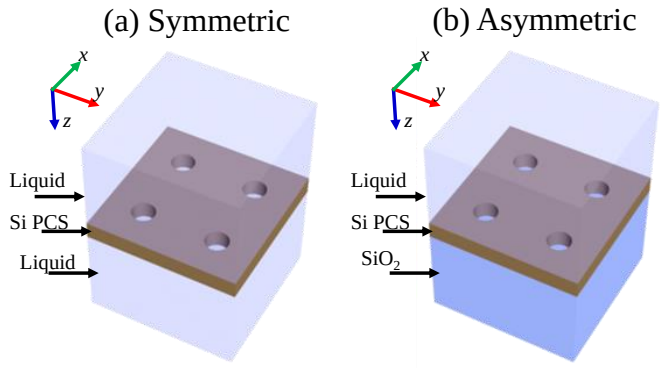

Figure 3-3 Schematic illustration of symmetric (a) and asymmetric (b) PCS design.[86]

The PCS sensor designed in this work is based on the shift of Fano resonance frequencies. As detailed in 2.3.2, Fano resonance is the coupling effect of in-plane discrete states (guided resonance modes) to the out-of-the-plane continuum states (vertical radiation modes).[39] In the reflection spectrum of PCS, Fano resonance results in a sharp Fano lineshape which has finite lifetime described by Q value.[101] The lattice geometry of PCS is very important for sensor optimization, which is shown in Figure 3-4, including slab thickness *t*, lattice constant *a*, and air hole radius *r*. Since the DL of a biosensor is inversely related to the sensitivity and Q factor, both high Q factor and high sensitivity are preferable to achieve better sensing performance. In guided-wave optics, however, these two requirements are contradictory, as the mode should be strongly confined in the structure to achieve a high Q factor, and strong overlap of optical field with analytes is required to have high sensitivity. We investigated the dependence of Q factor and sensitivity on lattice geometry, by varying the slab thickness *t*, lattice constant *a*, and air hole radius *r* in simulation.

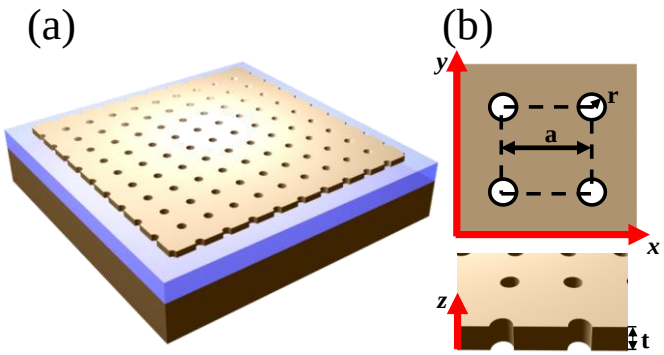

Figure 3-4 (a) Schematic of 2D PCS on SOI substrate. (b) Illustration of 2D PCS design parameter: slab thickness (*t*), lattice constant (*a*), and air hole radius (*r*).[112]

For slab thickness dependence of PCS sensor performance, shown in Figure 3-5(a) is the reflection spectra of PCS with various slab thickness from 120 nm to 200 nm, and the corresponding sensitivity for each resonant mode is plotted in Figure 3-5(b). With slab thickness decreasing, the effective RI of PCS structure is reduced, as a result that resonance modes shift towards shorter wavelength. We have examined the Q factor of the resonance modes that have highest sensitivity for PCS with different slab thickness, as seen in Figure 3-5(c). With the increase of slab thickness, both sensitivity and Q factor increase first, and then decrease, which is a result of asymmetric RI profile in asymmetric PCS design. If the PCS is symmetric, with slab thickness increasing, the electric field energy that extended into liquid region reduces, *i.e.*, filling fraction *f* decreases, and thus sensitivity reduces. However, in the case of asymmetric PCS design, due to the asymmetry of RI profile with the presence of SiO_2 substrate, more electric field energy penetrates into the substrate region if the slab is too thin (*e.g.*, <160 nm in our design), as a result of smaller *f* and sensitivity. For thicker slab (>160 nm) in asymmetric design, increasing the slab thickness, more electric field energy is constrained into the slab region,

as a result of smaller *f* and sensitivity. For the trend of Q values with slab thickness, with thin slab (<160 nm), the Q factor increases as slab thickness increases owing to less scattering within the slab and better electric field confinement from larger effective RI. When the slab thickness is larger than 160 nm, Q factor starts reducing.

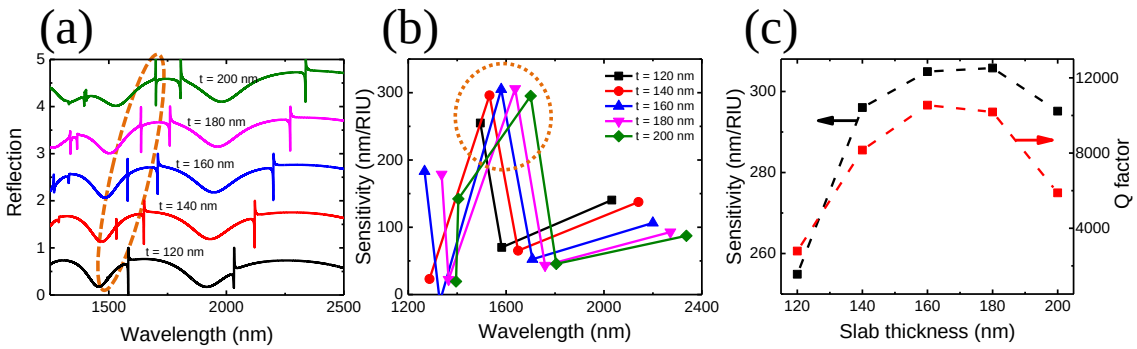

Figure 3-5 Calculated results of Fano resonance 2D PCS biosensor with various slab thickness. (a) Reflection spectra of PCS with slab thickness varying from 120 nm to 200 nm. (b) Sensitivity values versus corresponding resonant wavelengths for PCS with different slab thickness. (c) Q values and sensitivity of resonance mode with the highest sensitivity, for PCS with different slab thickness. In simulation, the PCS is covered by liquid with a RI of 1.33, and lattice constant a = 1,000 nm, r/a = 0.1.

Except slab thickness *t*, lattice constant *a* and air hole radius *r* are important parameters in determining the sensitivity and Q factor of PCS sensor. The reflection spectra, sensitivity, and Q values of PCS sensor with different lattice constant are shown in Figure 3-6. The reflection spectra in Figure 3-6(a) indicate that the resonance modes shift to longer wavelength when the lattice constant is increased, which is caused by the increased effective RI. Both sensitivity and Q factor increase as lattice constant increases, which is depicted in Figure 3-6(b) & (c). Keeping the same radius-to-lattice constant ratio

(*r*/*a*), increasing the lattice constant will increase the effective RI and reduce scattering loss, resulting in longer resonance lifetime, and hence higher Q value. Also, the effective detection zone on PCS surface is increased with the increasing of lattice constant, as a result of higher sensitivity. It is noted that we assume there is no liquid penetrated into air holes in the simulation, since the surface of Si is hydrophobic.

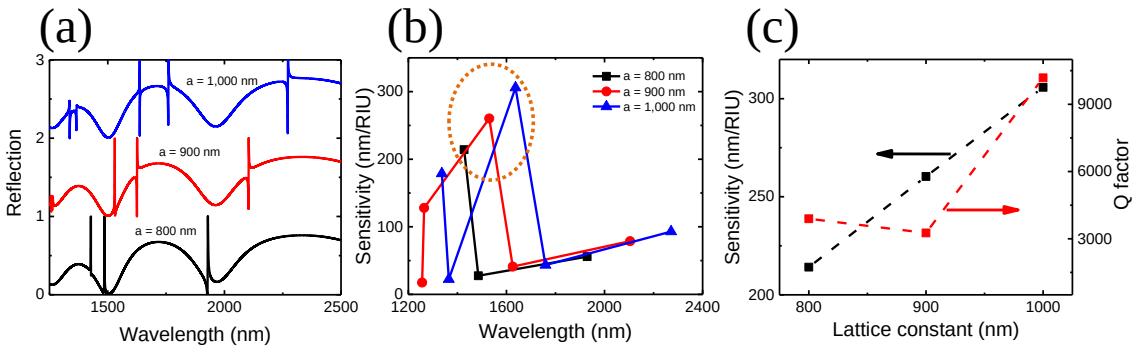

Figure 3-6 Calculated results of Fano resonance 2D PCS biosensor with various lattice constant. (a) Reflection spectra of PCS with lattice constant varying from 800 nm to 1,000 nm. (b) Sensitivity values versus corresponding resonant wavelengths for PCS with different lattice constant. (c) Q values and sensitivity of resonance mode with the highest sensitivity, for PCS with different lattice constant. In simulation, the PCS is covered by liquid with a RI of 1.33, and slab thickness t = 180 nm, r/a = 0.1.

The dependence of PCS sensor performance on radius-to-lattice constant ratio (*r*/*a*) is plotted in Figure 3-7. As shown in Figure 3-7(a), the reflection spectra experience blue shift with *r*/*a* increasing, which is expected, because the effective RI of the structure is reduced with increased *r*/*a*. When *r*/*a* is increased, *i.e.*, hole radius increased, the confinement of resonance mode to the slab region is weaker due to reduced effective RI, which enables more electric field energy extend outside the slab and interact with liquid,

i.e., higher filling fraction, and hence sensitivity is increased, as shown in Figure 3-7(b) & (c). Another effect with larger hole radius is that, the in-plane scattering effect will be increased. Both weaker mode confinement and stronger scattering effect give rise to shorter resonance lifetime, and hence lower Q factor as seen in Figure 3-7(c).

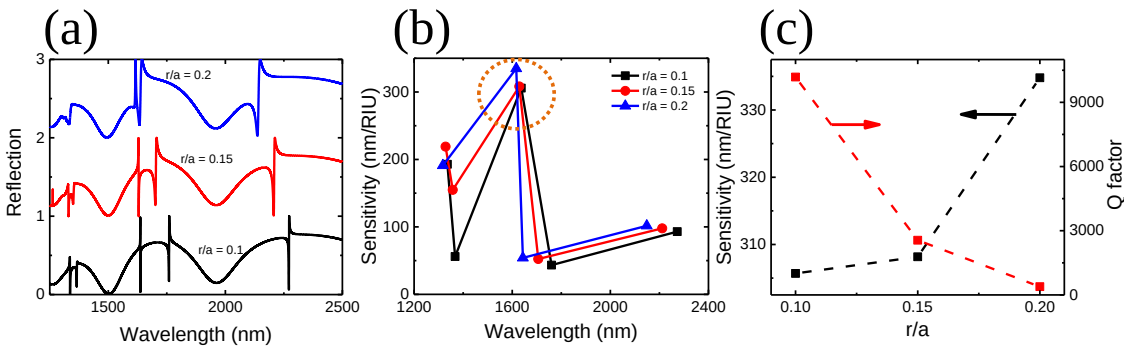

Figure 3-7 Calculated results of Fano resonance 2D PCS biosensor with various air hole radius. (a) Reflection spectra of PCS with *r/a* varying from 0.1 to 0.2. (b) Sensitivity values versus corresponding resonant wavelengths for PCS with different *r/a* value. (c) Q values and sensitivity of resonant mode with the highest sensitivity, for PCS with different *r/a* value. In simulation, the PCS is covered by liquid with a RI of 1.33, and slab thickness t = 180 nm, lattice constant a = 1,000 nm.

Combining the effect of slab thickness, lattice constant, and hole radius, as presented in Figure 3-5, Figure 3-6, and Figure 3-7, respectively, we can conclude that, the PCS with t = 160 nm, a = 1,000 nm, r/a = 0.1, will give the best sensing performance, *i.e.*, high Q factor, high sensitivity, and best DL.

Since there are two ways for the determination of PCS sensitivity, one is through tracking shifts in the Fano resonance frequency from reflection spectra computed with S^4 based on FMM as detailed in 3.1.1, the other approach is to calculate directly from

equation (3.5) with data collected from Meep based on FDTD method (*i.e.*, f and λ_0). We compared the results from both methods by evaluating the sensitivity of PCS with lattice geometry, t = 160 nm, a = 980 nm, r/a = 0.1. Shown in Figure 3-8(a) is the simulated reflection spectra in liquid environment with S^4. Through Fano fitting, a Q factor of 8,451 is estimated with resonance mode at 1,557 nm when n_{liquid} = 1.33. And a sensitivity of 300 nm/RIU is calculated based on the spectral shift from Δn = 0.005. Figure 3-8 (b-d) are the electric field energy distributions calculated from Meep when the PCS is immersed in liquid with a RI of 1.33 and resonance mode λ_0 is at 1,559.7 nm. Figure 3-8(c) and (d) show the mode profile in the yz plane (x = 0) and xy plane (z = 0), respectively. Dashed lines outline the boundary of the air hole. Figure 3-8(b) is the integrated electric field energy distribution along vertical direction (z-axis), which demonstrates the percentage of electric field energy outside PCS is 22.04%, *i.e.*, f = 22.04%. With equation (3.5), we can calculate that the sensitivity is 258.5 nm/RIU. The results from S^4 and Meep are consistent, and the slight deviation could be attributed to limited resolution and the inherent drawbacks presented in Table 3-1.

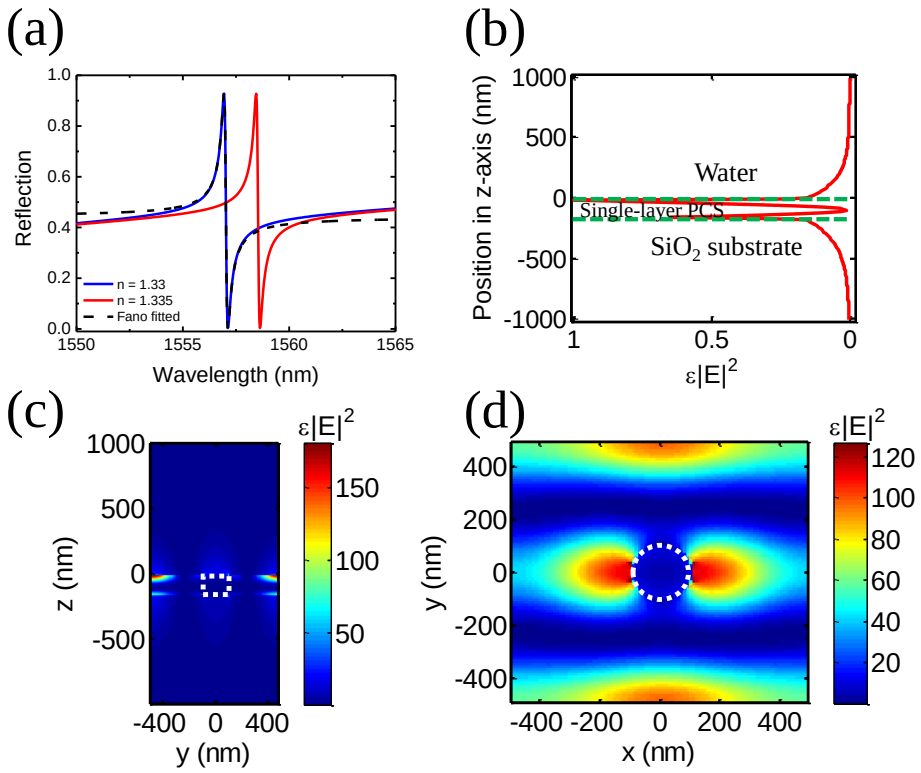

Figure 3-8 Simulation of Fano resonance reflection spectra and electric field distribution with PCS, t = 160 nm, a = 980 nm, and r/a = 0.1. (a) Calculated (solid blue) and fitted (dash black) Fano resonance reflection spectrum in liquid with n_{liquid} = 1.33. The spectral position is at 1,557 nm with a Q factor of 8,451. The red curve is calculated with n_{liquid} = 1.335, which demonstrates a sensitivity of 300 nm/RIU by tracking resonance frequency shift. (b) The electric field energy density along vertical direction (z-axis) showing filling fraction f = 22.04%. The sensor surface is located at z = 0. (c) and (d) show the mode profile in the yz plane (x = 0) and xy plane (z = 0), respectively. Dashed lines outline the boundary of the air hole. Note that the electric field energy distribution is calculated with n_{liquid} = 1.33.

3.3.2 Design of double-layer 2D PCS sensors

In the single-layer PCS discussed above, it possesses guided resonances that are strongly confined by the slab, but nevertheless can couple to the external radiation. Therefore, these guided resonances have a finite lifetime, *i.e.*, limited Q value, and are referred to as "bright guided resonances". In addition to the bright guided resonances, the single-layer PCS also possesses "dark guided resonances", which exist above the light line and would have been able to couple to radiation modes, but never couple to the external radiation due to either symmetric or dynamic reasons.[113, 114] Thus, these dark guided resonances have an infinite lifetime, *i.e.*, infinite Q factor. For the two-slab system, dark states can arise from the interaction of either bright or dark guided resonances in the single slab.[107] As shown in Figure 3-9, in which the two slabs are separated by certain specific distance, the dark states of such two-slab system arise from the coupled bright resonances in the single slab.

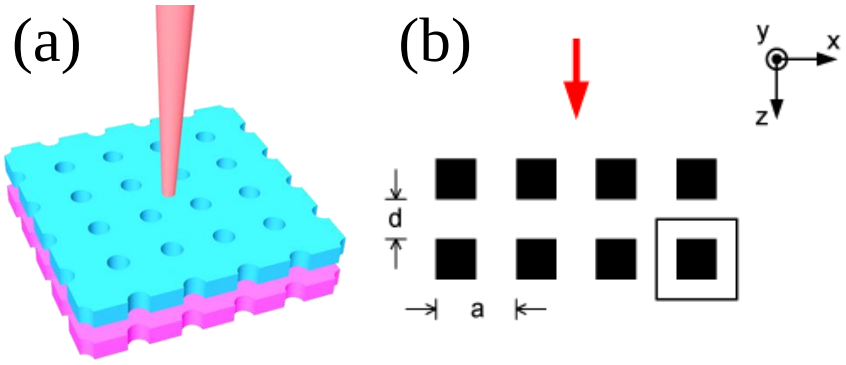

Figure 3-9 Schematic illustration of the double slab system: (a) 3D sketch. (b) Cross-sectional illustration.[107]

Starting with the single slab system, there always exists a frequency for which TIR happens near a bright guided resonance. Thus, a dark state can be formed by choosing an appropriate spacing (referred to as d_∞ below) between two slabs, such that a

Fabry-Pérot resonance between two slabs is formed exactly at the frequency where the reflectivity of each individual slab reaches unity.[115] For the two-slab system shown in Figure 3-10, $d_\infty = 0.65a$ (a is the lattice constant), the state is decoupled from the external radiation when the slab spacing d is equal to d_∞.[107] When the slab spacing d is in the vicinity of d_∞ (Figure 3-10(c) & (e)), the transmission spectrum of the two-slab system exhibits a lineshape, where a sharp transparency resonance peak exists within the center of a broad resonance dip.[114] Comparing Figure 3-10(c) ($d = 0.5a$) with Figure 3-10(e) ($d = 0.65a$), the width of transmission peak diverges as d approaches d_∞, as a result of higher Q factor. To design double-layer PCS system, we can start with a bright resonance in a single-layer PCS and introduce a second slab to create a near-dark state with a much higher Q factor. The Q factor is mechanically tunable over a wide range by adjusting the slab spacing and can be as high as infinity, which is the advantage of double-layer PCS for label-free sensing.

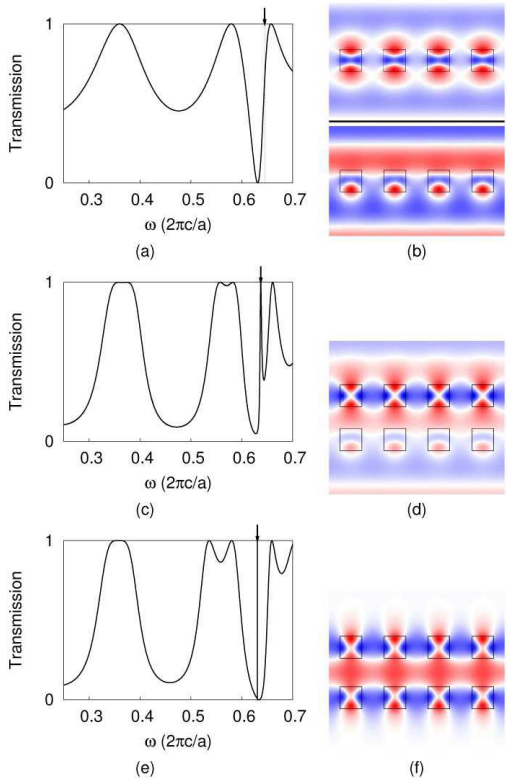

Figure 3-10 Dark state arising from coupled bright resonances in coupled symmetric PCSs: (a) Single slab transmission spectrum; the arrow indicates the frequency of a Fano resonance mode. (b) Mode profile calculated by photonic band structure code (MPB) (top) and field profile computed with scattering matrix method (SMM) at the frequency indicated by the arrow in (a) (bottom). (c) Double slab transmission spectrum for d = 0.5a. (d) Field profile at frequency indicated by the arrow in (c). (e) Double slab transmission spectrum for d = 0.65a; note the extremely sharp resonance peak. (f) Field profile at peak of resonance in (e).[107]

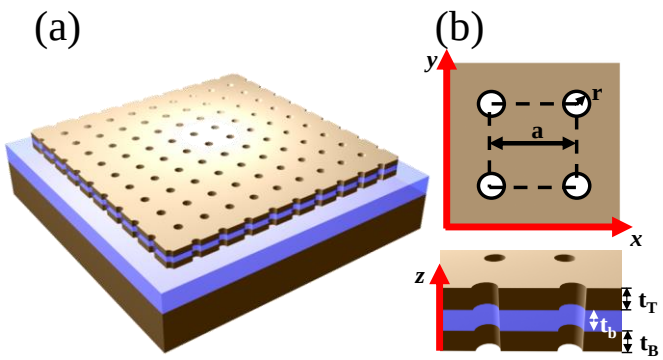

Figure 3-11 (a) Schematic of double-layer PCS on SOI substrate. (b) Illustration of double-layer PCS design parameter: lattice constant (a), air hole radius (r), top Si layer thickness (t_T), bottom Si layer thickness (t_B), and buffer oxide layer thickness (t_b).

As shown in Figure 3-11, the performance of double-layer PCS sensor can be optimized by adjusting the lattice geometry, including top Si layer t_T, bottom Si layer t_B, buffer oxide layer t_b (*i.e.*, slab spacing), lattice constant a, and air hole radius r. We start with a 230 nm single slab system with a = 1,000 nm and r/a = 0.1. The dependence of Q factor on two slab spacing t_b is explored firstly. The simulated spectra for double-layer PCS with various slab spacing are plotted in Figure 3-12(a), and the maximum Q factor from each structure is shown in Figure 3-12(b). With 60 nm slab spacing, a Q factor of 4.7×10^5 is obtained, which is almost fifty times of that from single-layer PCS. Since the DL of a label-free sensor is inversely proportional to the product between Q factor and sensitivity, we simulate the sensitivity of the double-layer structure, and corresponding product between Q factor and sensitivity is shown in Figure 3-12(c). With 60 nm and 100 nm slab spacing, this product reaches maximum, which is similar to that from single-layer PCS presented in 3.3.1. The effect of air hole radius is also investigated, which is

depicted in Figure 3-13. From Figure 3-13(c), the product between Q factor and sensitivity drops drastically as the hole radius increases.

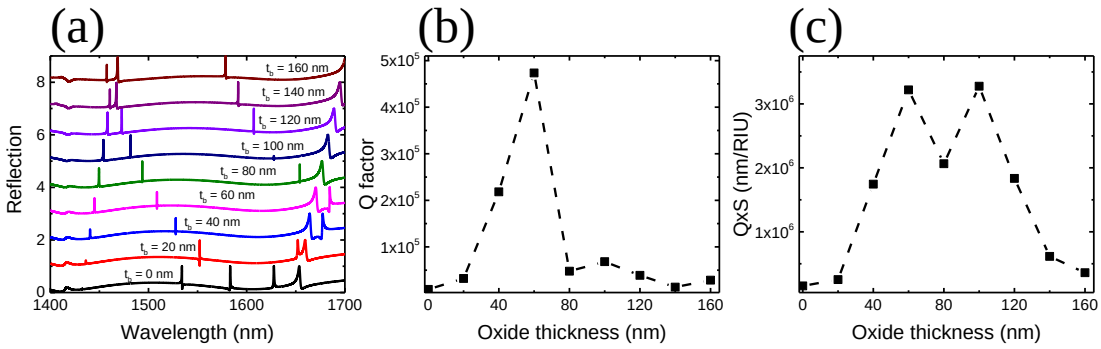

Figure 3-12 Calculated results of double-layer PCS biosensor with various oxide thickness. The thickness of top and bottom Si layer is 230 nm. (a) Reflection spectra of double-layer PCS with oxide thickness varying from 0 nm to 160 nm. (b) Q values for double-layer PCS with different oxide thickness. (c) The product of Q value and sensitivity for double-layer PCS with different oxide thickness. In simulation, the PCS is covered by liquid with a RI of 1.33, and lattice constant a = 1,000 nm, r/a = 0.1.

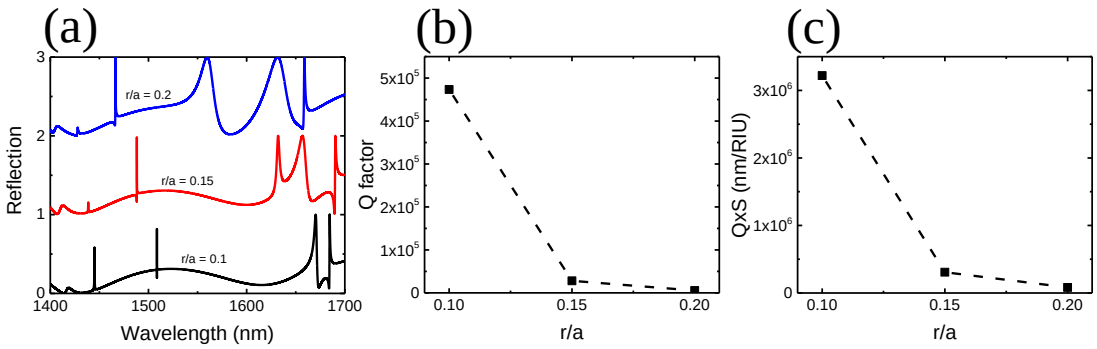

Figure 3-13 Calculated results of double-layer PCS biosensor with various air hole radius. The thickness of three layers, $t_T = t_B = 230$ nm, and $t_b = 60$ nm. (a) Reflection spectra of double-layer PCS with *r/a* varying from 0.1 to 0.2. (b) Q values for double-layer PCS with different *r/a* value. (c) The product of Q value and sensitivity for double-layer PCS with different *r/a* value. In simulation, the PCS is covered by liquid with a RI of 1.33, and lattice constant $a = 1{,}000$ nm.

In addition, we also examine the dependence of double-layer system on the single lab thickness. Starting with 230 nm single slab, we calculate the sensing performance of double-layer system with both thinner (200 nm) and thicker (260 nm) single slab. As seen from Figure 3-14(c), either thinner or thicker slab degrades the sensing performance of double-layer system. It is noted that these results are based on 60 nm slab spacing. For thinner or thicker single slab, the optimized slab spacing may not be 60 nm. Based on our current design, it can be concluded that double-layer PCS that is formed with 230 nm single slab and 60 nm or 100 nm slab spacing will generate excellent sensing performance.

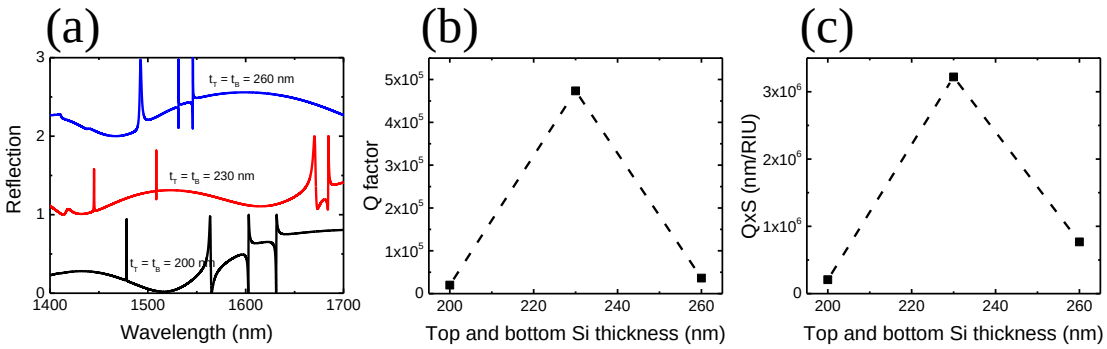

Figure 3-14 Calculated results of double-layer PCS biosensor with various top and bottom Si thickness. It is noted that: $t_T = t_B$, and the thickness of coupling oxide layer is 60 nm. (a) Reflection spectra of double-layer PCS with top and bottom Si thickness varying from 200 nm to 260 nm. (b) Q values for double-layer PCS with different top and bottom Si thickness. (c) The product of Q value and sensitivity for double-layer PCS with different top and bottom Si thickness. In simulation, the PCS is covered by liquid with a RI of 1.33, and lattice constant a = 1,000 nm, r/a = 0.1.

3.4 Conclusion

In this chapter, the computation methods, FMM and FDTD method, for PCS analysis were presented. The merits and demerits of two methods were discussed. The advantage of FDTD method is the time-domain calculation of field distribution, but it usually needs a lot of memory and takes very long computation time. FMM can compute high resolution spectrum with high accuracy within a few minutes, while it can only apply to uniform structures with in-plane periodicity. The sensitivity metrics of PCS sensor is also discussed, including bulk RI sensitivity and DL. Bulk RI sensitivity is related to the filling fraction of the sensor, and DL describes the smallest RI change that can be measured by a sensor, which is inversely proportional to both Q factor and

sensitivity.

Theoretical study of both single-layer and coupled double-layer PCS sensor using FMM and FDTD method was performed, and results were consistent. We have explored the dependence of spectral sensitivity and Q factor on lattice geometry (slab thickness t, slab spacing t_b for double-layer system, lattice constant a, and air hole radius r), and discussed the underlying physics. The simulated results and analysis provide a guideline for future PCS sensor design. Also, the optimized PCS structure will be applied for bulk liquid sensing characterization.

Chapter 4

Fabrication of Optofluidic Fano Resonance 2D PCS Sensors

4.1 Wafer preparation

The PCS investigated in this dissertation is fabricated on SOI substrate. For single-layer PCS, simulation results indicate that the PCS with 160 nm thick slab yields best sensing performance. However, the top Si layer of commercially available SOI wafer is fixed to several thicknesses, like 340 nm, 260 nm, and 230 nm.[116] To fabricate single-layer PCS, we need to firstly reduce the top Si layer of SOI wafer to the desired thickness (*e.g.*, 160 nm), which is called thin-down process. Thin-down process takes two steps, thermal oxidation of Si layer and wet etching of SiO_2 that formed from thermal oxidation with hydrofluoric acid (HF). For coupled double-layer PCS which has three layers, top poly-crystalline Si/coupling oxide/bottom single-crystalline Si, we start with SOI wafer whose Si layer serves as the bottom crystalline-Si layer. The first step is to form buffer oxide layer by thermal oxidation of Si layer on SOI substrate and HF etching of extra SiO_2. And then top poly-crystalline Si layer is formed using low pressure chemical vapor deposition (LPCVD) and annealing process. After each deposition and etching process, the layer thickness is characterized with the ellipsometer.

4.1.1 Thermal oxidation of Si

In microfabrication technology, thermal oxidation is a method to produce a thin layer of oxide (*e.g.*, SiO_2 and SiN_x) on the surface of a substrate, which is usually performed in furnaces at a temperature between 800 and 1,200 ^{0}C. Thermal oxidation of Si is through the diffusion of an oxidizing agent (molecular H_2O or O_2) into the Si wafer at high temperature and reacting with it to form SiO_2. There are two processes that are

widely used for the formulation of SiO_2 by thermal oxidation of Si, dry oxidation and wet oxidation, whose reactions can be described by[117]:

$$Si\ (solid) + O_2\ (vapor) - -\!-\!> SiO_2 \qquad Dry\ oxidation \qquad (4.1)$$

$$Si\ (solid) + H_2O\ (vapor) - -\!-\!> SiO_2 + 2H_2 \qquad Wet\ oxidation \qquad (4.2)$$

Wet oxidation is preferred to dry oxidation for growing thick oxide due to the higher oxidation rate. However, wet oxidation with fast rate yields a lower-density oxide with lower dielectric strength.

From the oxidation mechanism, it was told that Si is consumed as the oxide grows. Thus, thermal oxidation grows both down into the wafer and up out of it. Based on relative densities and molecular weights of Si and SiO_2, it was found that the amount of Si consumed is 44% of the final oxide thickness, as shown in Figure 4-1. This relationship is very important for calculating height of formed oxide and remaining Si during oxidation process.

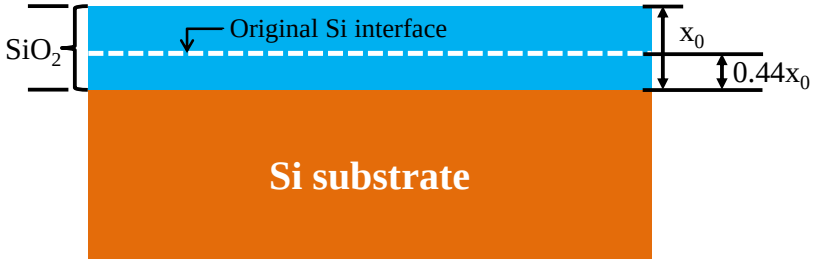

Figure 4-1 The thermal oxidation of Si model.[117]

The thermal oxidation rate of Si depends on many factors, including the pressure and temperature in the furnace, the photon flux during growth, the crystallographic orientation of the Si, the doping level of Si, the presence of halogen impurities in the gas phase, the presence of plasma during oxidation, etc. The time τ required to grow an oxide

of thickness X_0 at a constant temperature can be estimated by the commonly used Deal-Grove model[117]:

$$\tau = \frac{{X_0}^2}{B} + \frac{X_0}{\frac{B}{A}} \tag{4.3}$$

where the constants *A* and *B* encapsulate the properties of the reaction and the oxide layer, respectively.

In this dissertation, we use the well developed wet oxidation process at Microelectronics Reseach Ccenter (MRC) in the Univerisity of Texas Austin for the oxidation of Si. The process is performed in the field oxide furnace at a temperature of 1,050 ^{0}C. For the fabrication of single-layer PCS, SOI wafer with a top Si layer of 260 nm is oxidized for 18 mins, as a result that a new layer of 230 nm SiO_2 is formed on top and the left thickness of Si layer is 160 nm. For the fabrication of coupled double-layer PCS, SOI wafer with a top Si layer of 260 nm is oxidized for 25 mins with 250 nm SiO_2 layer formed on top serving as coupling oxide layer and 230 nm Si layer left serving as bottom Si layer.

4.1.2 Thin-down process

Since the product of thermal oxidation is a layer of SiO_2 on the top surface, this SiO_2 layer can be removed by wet etching with HF solution if it won't be needed in the structure. The combination of thermal oxidation and wet etching of SiO_2 is called thin-down process. For our single-layer PCS, after thermal oxidation of Si layer, 230 nm SiO_2 on the top surface is etched with diluted HF for 4 mins at a rate of 1 nm/sec, and then 160 nm Si layer is left on the top surface for PC fabrication. For coupled double-layer PCS, after thermal oxidation, there is 250 nm SiO_2 formed on the top surface. Since we need

certain thickness of SiO_2 to serve as the coupling oxide layer, the extra SiO_2 is etched away with HF too.

4.1.3 Low pressure chemical vapor deposition of poly-crystalline Si

In coupled double-layer PCS, there are three layers, top poly-crystalline Si/coupling oxide/bottom single-crystalline Si. After thin-down process, the coupling oxide and bottom Si layer are formed. The final step is to form top poly-crystalline Si layer with LPCVD process. CVD refers to a chemical process used to produce a variety of dielectric thin films with high quality. In a typical CVD process, the substrate is exposed to one or more volatile precursors, which react and/or decompose on the substrate surface to produce the desired deposition. LPCVD is a kind of CVD at sub-atmospheric pressure (often a few hundred mTorr). Reduced pressure tends to reduce unwanted gas-phase reactions and improve film uniformity across the wafer.[117] Compared to other CVD processes, like atmospheric pressure CVD (APCVD) and plasma enhanced CVD (PECVD), LPCVD yields thin film with excellent purity and uniformity, as well as conformal step coverage, while the deposition needs high temperature environment and the deposition rate is pretty slow (a few nm/min).

The mechanism of Si deposition with LPCVD is the thermal decomposition of silane (SiH_4) at high temperature (500 - 700 ^{0}C). The deposition reaction can be described by[117]:

$$SiH_4 + surface\ site = SiH_4\ (adsorbed) \quad (4.4a)$$

$$SiH_4\ (adsorbed)\ = SiH_2\ (adsorbed) + H_2\ (gas) \quad (4.4b)$$

$$SiH_2\ (adatom) = Si\ (solid) + \ H_2\ (gas) \quad (4.4c)$$

where the adsorption of the SiH_4 is followed by decomposition to an intermediate compound, SiH_2. And then, the solid film forms upon the evolution of the remaining hydrogen. The overall reaction can be given as[117]:

$$SiH_4\ (vapor)\ = Si\ (solid) + 2H_2\ (gas) \tag{4.5}$$

The top Si layer of coupled double-layer PCS structure is deposited using LPCVD with 150 sccm SiH_4 flow, at a temperature of 550 ^{0}C and a pressure of 300 mTorr. The estimated deposition rate is 3 nm/min. The Si layer formed from LPCVD process is amorphous Si which is non-crystalline form of Si and suffers from strong optical loss. Thus, another two steps of annealing process are applied in order to form poly-crystalline Si. The first annealing process is done at 600 ^{0}C for 30 hours, and the second annealing process is done at 1,000 ^{0}C for 5 hours.

4.2 Fabrication of 2D PCS

After the appropriate Si and SiO_2 films are formed on SOI wafer, it is ready for PC patterning. PC pattern is defined as large as 500 μm by 500 μm, which is chosen for avoiding stitching problem during EBL, easy light coupling, and biosensing with sufficient surface area. PC structure is generated using Clewin layout tool, written with EBL, and then transferred onto the substrate with RIE process.

For single-layer PCS, after pattern definition with EBL, top Si is etched by RIE process with resist as hard mask. Si PC is left after removing resist with piranha solution (a mixture of H_2SO_4 and H_2O_2). The detailed process flow for single-layer PCS fabrication is illustrated in Figure 4-2.

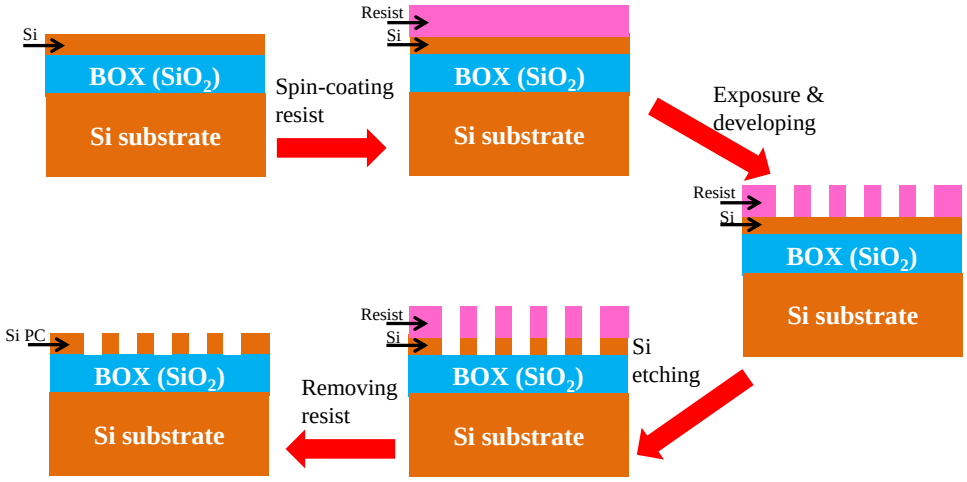

Figure 4-2 Fabrication process flow of single-layer PCS.[112]

For coupled double-layer PCS, since there are three steps etching involved, top Si layer/coupling oxide layer/bottom Si layer, a layer of 400 nm thick resist is not enough as etching hard mask due to low selectivity between Si/SiO_2 and resist from etching recipe. Thus, another layer of metal film is deposited onto the structure before EBL patterning, which will serve as hard mask during RIE process.[50] Cr film is deposited with electron beam evaporator (CHA Industries) which is operated in high vacuum chamber with a pressure of around 10^{-6} Torr. The evaporation rate is 0.04 nm/sec by controlling the electron beam current. Such high vacuum condition and low evaporation speed will render pretty uniform metal film with high density. The thickness of Cr film is 40 nm which is enough as hard mask for the etching of double-layer PCS. After Cr film deposition, PC pattern is defined with EBL, and followed by etching of Cr hard mask/top Si/oxide/bottom Si. At last, resist is cleaned with piranha solution and Cr layer is etched away with Cr etchant. The detailed fabrication flow of double-layer PCS is depicted in Figure 4-3.

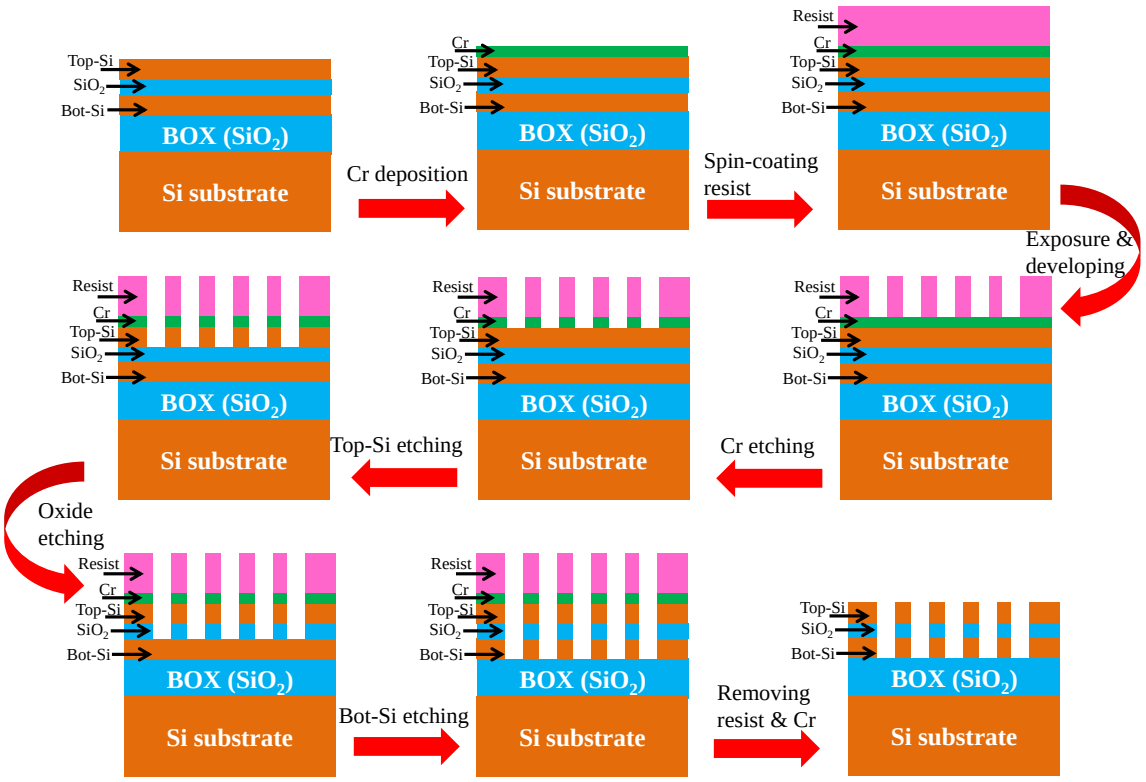

Figure 4-3 Fabrication process flow of coupled double-layer PCS.[50]

4.2.1 Pattern definition with electron-beam lithography

There is a variety of lithography technologies for PC pattern definition, like optical lithography, nanoimprint lithography, laser interference lithography, and EBL. Among them, EBL, which uses a focused beam of electrons to directly write the designed pattern onto substrate, provides highest resolution (sub-10 nm), best hole shape and sidewall, as well as minimized defect with pattern dimension as large as several millimeters. The main drawback of EBL is long run-time for large area patterns since the patterns are written serially as the electron beam scans across the surface of the substrate. In this dissertation, the PC structures are defined with EBL tool in MRC (Jeol 6000). The first step of pattern definition is spin-coating resist which will serve as etching mask for later pattern transferring. In general, the resist can be classified into two groups, positive

tone resist and negative tone resist. Positive tone resist refers to a type of resist in which the properties of resist that is exposed to an electron beam are changed and the exposed region becomes soluble in the resist developer. Negative tone resist refers to a type of resist in which the portion of resist that is exposed to an electron beam becomes insoluble to the developer.

In this work, we choose positive tone resist ZEP 520A from ZEON, because it offers higher resolution, higher sensitivity, and better resistance to dry etching over other resists. The sample is spin-coated with resist at 2,600 rpm/sec for 60 sec, and followed by baking at 180 ^{0}C for 60 sec on a hot plate. Such recipe results in a layer of about 400 nm thick resist. After spin-coating, the resist is patterned by EBL tool with optimized exposure conditions, a 50 kV excitation voltage and 108 $\mu C/cm^2$ electron dose. After exposure, the sample is developed in ZEP developer for 60 sec, which is a wet etching process of exposed ZEP 520A resist. Anisotropic etching is realized by the selectivity provided from electron beam exposure.

4.2.2 Pattern transfer with reactive-ion etching

After PC pattern is defined in the resist with EBL, the next step is to transfer the pattern through dry etching of Si/SiO_2. The successful PC pattern transfer requires an anisotropic etching process with high selectivity to etching mask, and one of the popular techniques is RIE which is a kind of dry etching and uses a combination of chemical etching by plasma activation and physical etching by ion bombardment.[117] In a typical RIE chamber, the plasma of reactive gases is generated by applying a strong radio frequency (RF) electromagnetic field under high vacuum condition. High-energy ions from the plasma are accelerated and directed to the etching surface (*e.g.*, Si), absorb and

react with the surface molecules, forming a volatile reaction product that can be easily desorbed from the surface. Figure 4-4 depicts the primary processes occurring in a plasma etching chamber.

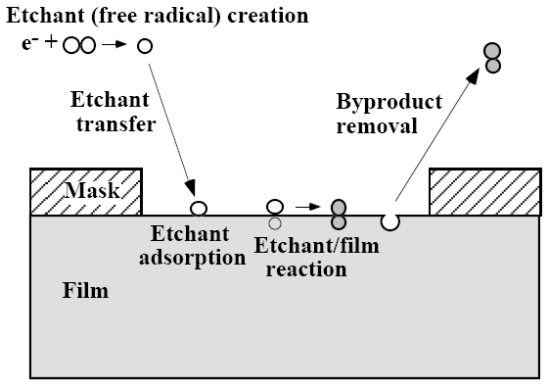

Figure 4-4 Primary processes happened in a plasma etching chamber.[117]

The plasma is a critical feature in dry etching, since it not only provides the energetic ionic bombardment to the etched surface, but also produces the reactive species for film removing. Etching directionality is provided by the applied RF potential in the chamber. The etching rate and profile can be adjusted by tuning the gas flow, chamber pressure, and RF power.

In our PCS fabrication, the Si layer is etched in a reactive ion etcher with chlorine (Cl_2) and hydrogen bromide (HBr). The adding of HBr makes the Si etching profile more anisotropic than when only using Cl_2, and HBr also improves the etching selectivity to resist and oxide.[118] The recipe we used for Si etching yields an etching rate of 23 nm/min. The coupling oxide layer in double-layer PCS is etched by RIE process too, using fluoroform (CHF_3) at a rate of 10 nm/min. The detailed etching recipes for Si and SiO_2 are listed in Table 4-1. The scanning electron microscope (SEM) images of single-

layer and coupled double-layer PCS after etching are shown in Figure 4-5 and Figure 4-6, respectively.

Table 4-1: RIE recipe for Si and SiO_2

Parameters	Gas/flow (sccm)		Pressure (mTorr)	RF power (W)	DC voltage (V)	Etching rate (nm/min)
Si etching	Cl_2/4	HBr/25.4	35	170	250	23
SiO_2 etching	CHF_3/40	O_2/3	40	260	400	10

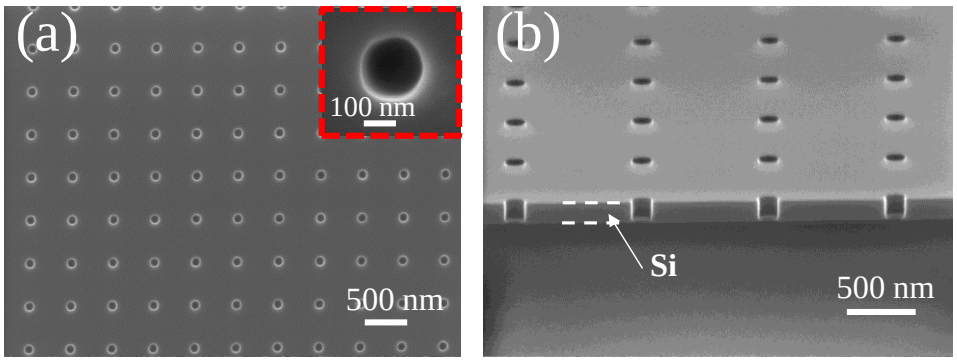

Figure 4-5 SEM images of fabricated single-layer PCS on SOI substrate. (a) Top view showing lattice constant a = 970 nm and air hole radius r = 103 nm. Inset shows the zoomed-in image of the air hole. (b) Cross-sectional view showing slab thickness t = 156 nm.[112]

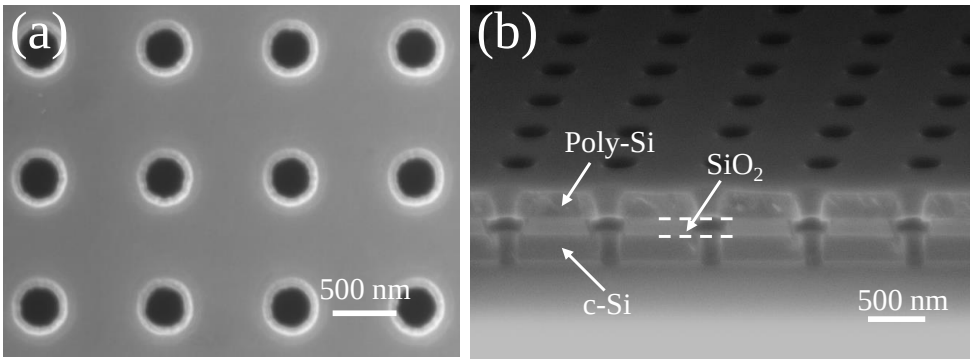

Figure 4-6 SEM images of fabricated coupled double-layer PCS on SOI substrate. (a)Top view showing lattice constant a = 1,000 nm and air hole radius r = 180 nm. (b) Cross-sectional view showing top layer PCS (t_T = 230 nm) and bottom layer PCS (t_B = 222 nm) separated by a coupling oxide layer (t_b = 160 nm).

4.3 Fabrication of PDMS microfluidic channel

To build optofluidic PCS sensing platform, another layer of PDMS microfluidic channel made with soft lithography is bonded onto PCS using oxygen plasma treatment to form the fluidic chamber for analyte delivery. There are two processes involved in the fabrication of PDMS microfluidic channel, photolithography and soft lithography. Before making the channel with soft lithography, the negative relief pattern of the channel feature needs to be defined with photolithography on a substrate (*e.g.*, Si or glass substrate), which is called master serving as mold in soft lithography. Once the desired features are defined, PDMS mixture is poured onto the master and cured in an oven or hot plate. This process of making PDMS patterns with master is also called replica molding (REM).[119] The detailed fabrication process will be discussed in this section.

4.3.1 Design of microfluidic channel

Several factors need to be considered in the design of microfluidic channel for practical sensing applications, like total volume of the chamber, efficient analyte delivery, flow dead volume, alignment with the sensor, multi-channel for parallel detection. The chamber size should be as small as possible to reduce analytes consumption without degrading the sensing performance. Flow dead volume should be avoided for efficient analytes transportation and accurate detection. Since microfluidic channel needs to be bonded onto the sensor, the possible challenge during alignment between sensor and channel should be considered and minimized in the channel design. Since the PCS device presented in this dissertation has an area of 500 μm by 500 μm, the microfluidic channel is designed to have a width of 1 mm, which can be aligned with the PC mesa easily. Multi-channel can be designed for parallel detection with sensor arrays. One example of the microfluidic channel we designed for PCS sensor is shown in Figure 4-7, which generates smooth flow during sensing and avoids any possible dead volume issues. With 100 μm depth, the total volume of the channel is 1.97 μL.

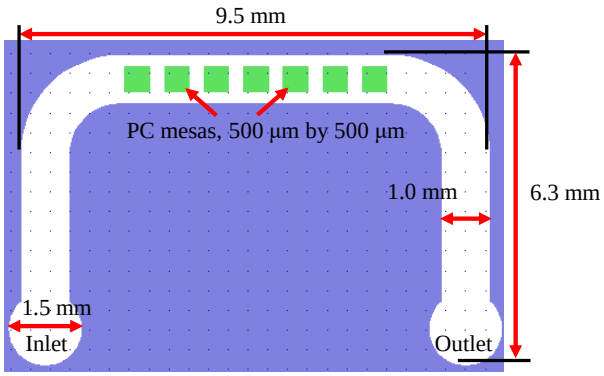

Figure 4-7 Design of microfluidic channel with a row of PC patterns inside. The white color region is MF channel with 1.0 mm width, and the squares with green color are PC patterns with 300 μm spacing that aligned in microfluidic channel. The diameter of inlet and outlet holes is 1.5 mm.

4.3.2 Fabrication of SU-8 mold with photolithography

The negative relief pattern of microfluidic channel can be defined through photolithography or RIE process on Si or glass substrate. In this dissertation, we choose photolithography to fabricate the master with SU-8 photoresist on Si substrate, due to its simplicity for patterning large features (μm to mm). SU-8 is a type of negative tone photoresist, and can be patterned with a wide range of thickness (a few μm to several hundred μm). The typical process flow for SU-8 patterning with photolithography is shown in Figure 4-8. A normal process includes spin-coating, soft bake, exposure, post exposure bake (PEB), and develop. PEB is attended to thermally cross-link SU-8 upon exposure. The thickness of SU-8 pattern can be controlled by its viscosity, spin-speed, temperature, and period of both soft bake and PEB. A controlled hard bake is recommended to further cross-link the structure when it will remain as part of the device. The whole process should be optimized for specific application. We use SU-8 2100 (MicroChem) photoresist in this work which is exposed to i-line (365 nm) light with mask aligner. The process is as follows, which is optimized to create SU-8 structure with a thickness of 100 μm.

1. Clean Si substrate with acetone, isopropanol (IPA), deionized (DI) water, and dry with N_2.

2. Dehydrate the substrate on a hotplate at 120 ^{0}C for 1 min.

3. Spin-coating SU-8 2100 at 3,000 rpm for 1 min.

4. Soft baking at 65 ^{0}C for 5 mins and 95 ^{0}C for 20 mins.

5. Exposure using a mask aligner (OAI Model806) for 12 sec.

6. Post exposure baking at 65 ^{0}C for 5 mins and 95 ^{0}C for 10 mins.

7. Develop with SU-8 developer for 10 mins.

8. Rinse the sample with IPA, and dry with N_2.

9. Measure the thickness with profilometer.

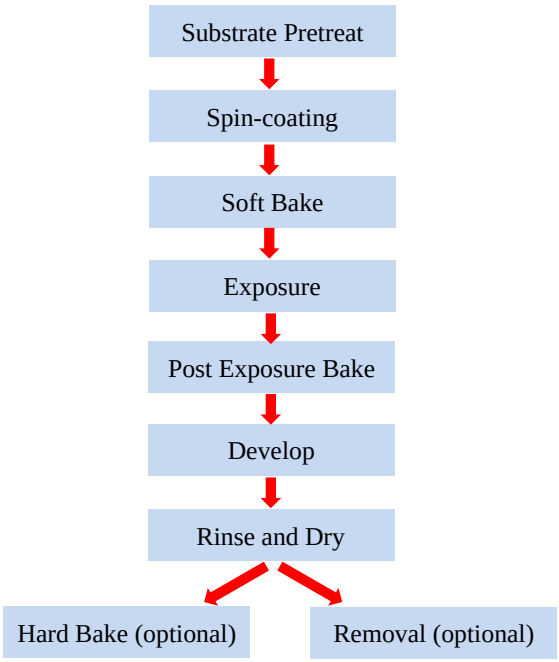

Figure 4-8 Process flow of SU-8 patterning with photolithography.

Silanizing of SU-8 mold is recommended before casting PDMS, which forms a monolayer on the surface that prevents the PDMS from adhering to the master and makes the peeling of PDMS easier.[120] Silanizing process is performed in a desiccator with a drop of trichloro(1,1,2,2-perfluoocytl)silane placed in a vial and SU-8 mold inside. The desiccator is placed under vacuum for 24 hours to cause the silanizing agent to evaporate and form a monolayer on the surface of SU-8 master. The fabricated SU-8 mold on Si substrate for microfluidic channel is shown in Figure 4-9, which has a thickness of 100 μm.

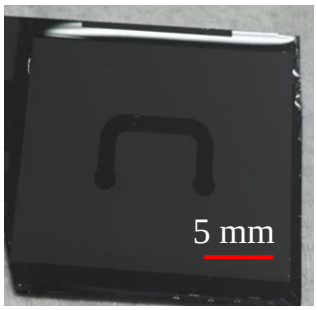

Figure 4-9 Fabricated SU-8 mold with 100 μm thickness on Si substrate.

4.3.3 Fabrication of microfluidic channel with soft lithography

Typically, microfluidic channel is made of PDMS elastomer, which is purchased as a two-part elastomer kit consisted of PDMS prepolymer and a curing agent (SYLGARD® 184 Silicone Elastomer Kit). PDMS is extremely popular for making microfluidic devices in many applications due to its useful properties. Firstly, PDMS provides a surface with good chemical stability and low interfacial free energy; most molecules or polymers being patterned do not react with PDMS. Secondly, PDMS is not hydroscopic; thus it does not swell with humidity. And it has good thermal stability (up to 186 ^{0}C in air). Moreover, PDMS elastomer is optically transparent down to 300 nm, making it advantageous in many optical related applications. In addition, the interfacial properties of PDMS elastomer can be easily changed by modifying the prepolymer or treating the surface with plasma for different application purposes.

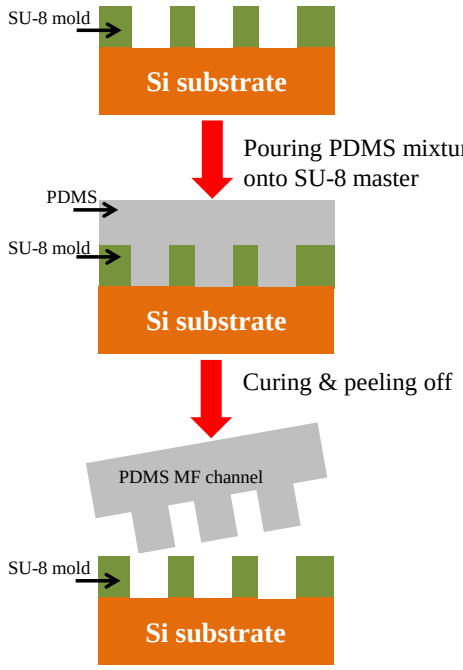

Figure 4-10 Schematic illustration of PDMS microfluidic channel fabrication procedure with SU-8 mold.

Preparing PDMS is quite straightforward. Sylgard 184 silicone base is mixed with the curing agent in a 10:1 ratio by weight. The mixture is degassed in a desiccator to remove air bubbles and then poured onto the master. The PDMS mixture is cured on a hot plate at 80 ^{0}C for 50 mins. After cooling, the PDMS stamp can be easily peeled from the master and cut into desired shape. The process flow is described in Figure 4-10. In this work, the thickness of fabricated PDMS stamp is around 5 mm, and the microfluidic channel has a depth of 100 μm, which is determined by the thickness of SU-8 feature created from photolithography. For fluidics access, inlet and outlet holes are punched with a glass capillary (Polymicro Technologies, TSP530660, ID = 535 μm, OD = 664 μm) for tubing connection.

4.3.4 Oxygen plasma treatment

Once the PDMS stamp is peeled from the mold and cut into desired shape, it is ready for assembly with PCS on SOI substrate into a final device. To permanently bond PDMS stamp onto SOI substrate, PDMS stamp and PCS chip undergoes oxygen plasma treatment. Before oxygen plasma treatment, the PCS is firstly cleaned with piranha solution for 20 mins to strip organic material from the surface, which is critical to achieve a good bonding. After clean process, both PDMS stamp and PCS chip are exposed to oxygen plasma in an Asher (Diener Electronics), whereby surface Si-CH_3 groups along the PDMS backbone are transformed into Si-OH groups by the reactive oxygen species in the plasma, and Si-OH groups are exposed to the surface of Si too. And then the PDMS stamp is bonded onto PCS by hand using microscope so that the PC mesas can be aligned in the microfluidic channel. Figure 4-11 presents an example of PC mesas aligned in the microfluidic channel during bonding process.

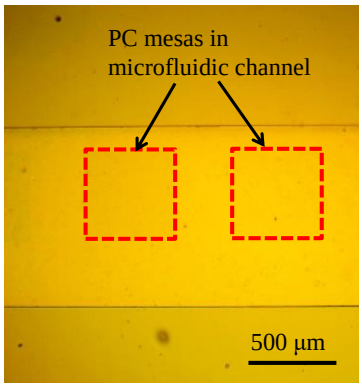

Figure 4-11 Microscopic image showing two PC mesas aligned in microfluidic channel during bonding process. Red dash lines are PC boundary.

After bonding, stainless steel ferrules (New England, NE-1300-01, OD = 0.025”, ID = 0.017”, Length = 0.5") are inserted into access holes as fluidic ports and tygon tubing (Cole-Parmer, AAD02103-CP ND-100-80, ID = 0.02", OD = 0.06") is used to

deliver fluidics in and out of PCS sensor. The inner diameter of tygon tubing is slightly smaller than the outer diameter of stainless steel ferrules, which ensures adequate sealing for fluidics. Image of an optofluidic PCS sensor is shown in Figure 4-12.

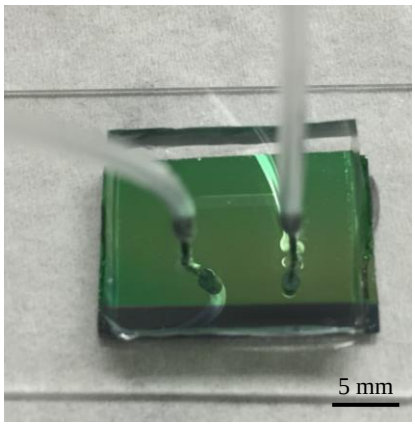

Figure 4-12 One example of fabricated optofluidic PCS sensor. A microfluidic channel with 100 μm depth bonded onto a 15 mm by 20 mm PCS chip. Stainless steel ferrules (New England, NE-1300-01, OD = 0.025”, ID = 0.017”, Length = 0.5") are inserted into access holes as fluidic ports and tygon tubing (Cole-Parmer, AAD02103-CP ND-100-80, ID = 0.02", OD = 0.06") is used to deliver fluidics in and out of PCS sensor.

4.4 Conclusion

In this chapter, the detailed fabrication technologies for both single-layer and coupled double-layer PCS are presented. The structures of PCS are prepared by thermal oxidation, LPCVD, and thin-down process. Thermal oxidation is used to form SiO_2 through the diffusion of an oxidizing agent into the Si wafer at high temperature. It grows both down into the Si wafer and up out of it. Thin-down process is employed for reducing the Si layer into desired thickness, which is a combination of thermal oxidation of Si and wet etching of SiO_2 formed during oxidation process. The top poly-crystalline Si of

double-layer structure is generated with LPCVD and annealing process. The smaller pressure during LPCVD process improves the uniformity of dielectric thin film formed across the wafer. In order to reduce the optical loss, two-steps annealing process is applied to transfer the amorphous Si formed from LPCVD into poly-crystalline Si.

PCS is fabricated with EBL and RIE process. The etching of single-layer PCS is done in one step, *i.e.*, RIE of Si layer; while the etching of double-layer PCS takes three steps, including RIE of top Si layer, coupling SiO_2 layer, and bottom Si layer. Soft lithography for making PDMS microfluidic channel is also discussed. Before making PDMS microfluidic channel with soft lithography, SU-8 master is fabricated with photolithography and then silanized with trichloro(1,1,2,2-perfluoocytl)silane for easily peeling from PDMS. The microfluidic channel is bonded onto PCS chip using oxygen plasma treatment to form optofluidic PCS sensor.

Chapter 5

Label-free Fano Resonance 2D PCS Liquid Sensor

5.1 Characterization of 2D PCS liquid sensor

5.1.1 Fano resonance reflection spectrum of 2D PCS

The Fano resonance PCS is characterized by measuring the reflection spectrum with a tunable laser system at normal incidence. Schematic illustration of the measurement system is shown in Figure 5-1. Light from a tunable laser source (Agilent 81980A, wavelength range: 1,465 nm - 1,575 nm) is coupled into free space by a fiber optic circulator (Thorlabs, 6015-3-APC), collimated with a collimator, and then focused onto the device with an optical lens. The diameter of beam spot incident onto the device is around 100 μm. The 50% power of reflected beam from PCS is reflected by the beam splitter (BS), and collected by a photodetector (Agilent 81623B) for reflection spectrum measurement. The other 50% power transmits through the BS, circulator, and is received by the optical spectrum analyzer (OSA) for incident angle alignment purpose. The angle change of PCS chip through adjusting screws of sample mount causes the change of incident angle, resulting in a change of reflected power received by OSA. Normal incidence is realized when the reflected power collected by OSA reaches maximum value. The relative position between laser spot and PC mesa is monitored by a thermal camera (GOODRICH, SU320MS-1.7RT) using white light source. A snapshot from thermal camera in Figure 5-2 shows that light beam from tunable laser is incident onto PC mesa. Such surface normal incidence and detection setup eliminates the delicate alignment for light coupling needed by other optical label-free sensors and it is advantageous for system miniaturization as well as scaling up the device into multiplexed sensing arrays on

chip. One example of measured Fano resonance reflection spectrum from coupled double-layer PCS in air environment is shown in Figure 5-3. The zoom-in of Fano resonance mode in Figure 5-3(b) shows the asymmetric Fano lineshape with sharp peak-to-dip transition.

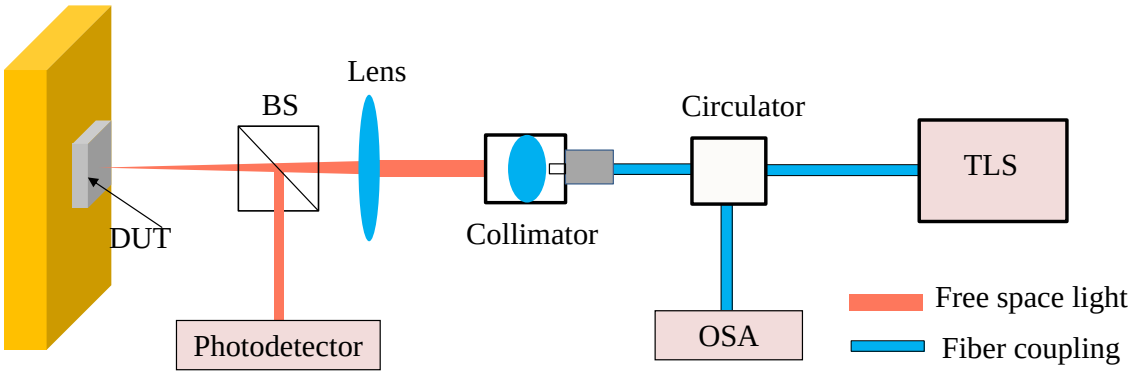

Figure 5-1 Schematic illustration of the normal incident measurement system. TLS: tunable laser source; OSA: optical spectrum analyzer; BS: beam splitter. DUT: device under test (PCS sensor).[112]

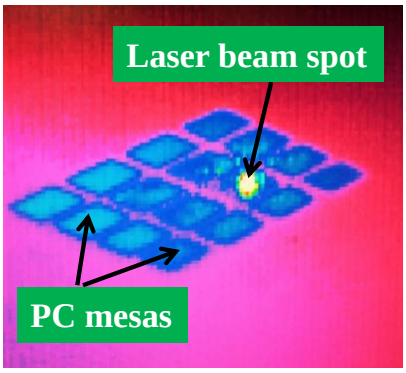

Figure 5-2 A snapshot from thermal camera showing laser spot on PC mesa. The blue squares are PC mesa, and the shining spot is laser spot.

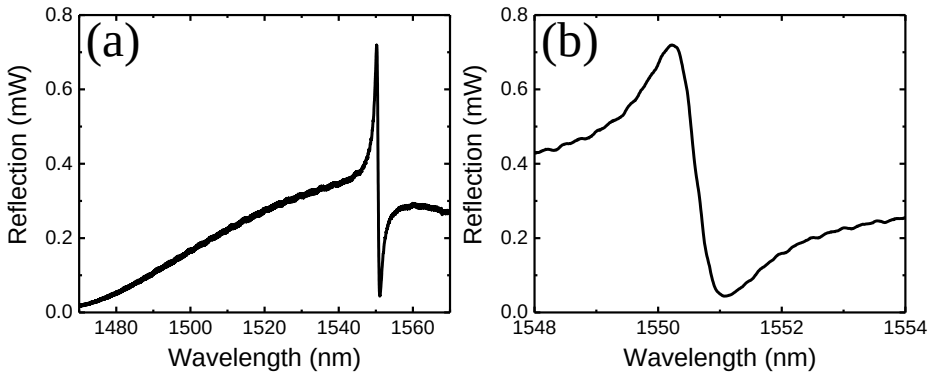

Figure 5-3 (a) Measured Fano resonance reflection spectrum of coupled double-layer PCS in air environment, with top Si layer t_T = 233 nm, bottom Si layer t_B = 229 nm, coupling oxide layer t_b = 163 nm, lattice constant a = 1,000 nm, and air hole radius r = 170 nm. (b) Zoom-in of Fano resonance mode at 1,550.6 nm showing the asymmetric Fano lineshape with sharp peak-to-dip transition.

As detailed in 2.3.2, Fano resonance, known from atomic physics, is used to describe asymmetric resonance that arises from the constructive and destructive interference of discrete resonance states by broadband continuum states.[97] This phenomenon is ubiquitous in many realms of physical sciences, and can be found in many nanophotonic structures.[99, 100] Unlike traditional Lorentzian resonance which exhibits symmetric lineshape, Fano resonance demonstrates a distinctly asymmetric lineshape that can be expressed by the following formula[100]:

$$I \propto \frac{(F \times \gamma - \omega + \omega_0)^2}{(\omega - \omega_0)^2 + \gamma^2} \tag{5.1}$$

where ω_0 and γ represent the position and width of the resonance, respectively; and F is the Fano parameter which describes the degree of asymmetry. Thus, the resonance

position and Q factor can be quantified by fitting the spectrum with this equation. The corresponding Q factor is obtained by[100]:

$$Q = \frac{\omega_0}{2\gamma} \tag{5.2}$$

A Fano fitting to the measured reflection spectrum of coupled double-layer PCS is shown in Figure 5-4, which demonstrates a resonance mode at 1,550.6 nm with a Q factor of 1,900. In this dissertation, the resonance position and Q factor of all characterized PCS are acquired by fitting the reflection spectrum with equation (5.1).

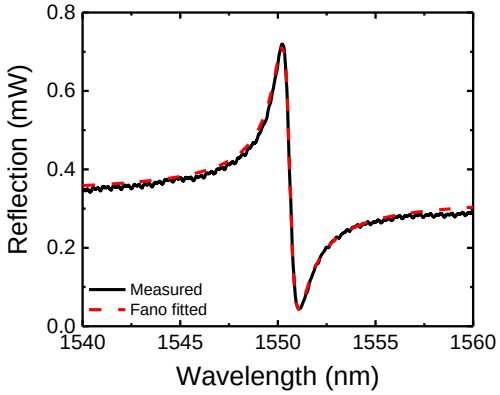

Figure 5-4 Fano fitting (red dash) to measured reflection spectrum (black solid) of coupled double-layer PCS showing resonance mode at 1,550.6 nm with a Q factor of 1,900. Double-layer PCS geometry: top Si layer t_T = 233 nm, bottom Si layer t_B = 229 nm, coupling oxide layer t_b = 163 nm, lattice constant a = 1,000 nm, and air hole radius r = 170 nm.

5.1.2 Bulk liquid sensing

The sensing performance of PCS sensor is evaluated by measuring the bulk RI sensitivity using liquid of known refractive indices. In our experiment, an ethanol/DI water mixture (v/v) is used because the RI of different concentrations of ethanol/DI water

solution is known which is plotted in Figure 5-5. Bulk RI sensitivity is specified by Fano resonance spectral shift per RIU. Initially, the PDMS microfluidic channel is filled with DI water to establish the baseline of resonance spectrum. And then ethanol/DI water mixture with higher RI is flowed through the microfluidic channel, as a result that Fano resonance spectral position shifts to a longer wavelength. A DI water rinsing step between each new concentration is performed to ensure that the chamber is free of residual ethanol, and the Fano resonance spectral shift is measured in real-time at a frequency of 2 Hz with home-made Labview program. Figure 5-6 presents an example of measured sensorgram from single-layer PCS. It is obvious that the Fano resonance mode is shifted to the longer wavelength with ethanol/DI water mixture in the chamber, and fully back to baseline during DI water rinsing step after each concentration measurement. The bulk liquid sensing performance of both single-layer and coupled double-layer PCS will be discussed in section 5.2 and 5.3, respectively.

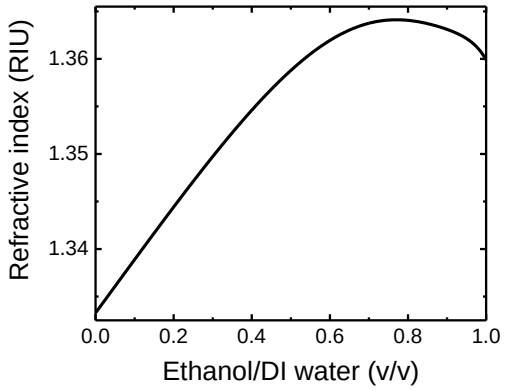

Figure 5-5 Refractive indices of ethanol/DI water mixture with different concentrations (v/v).

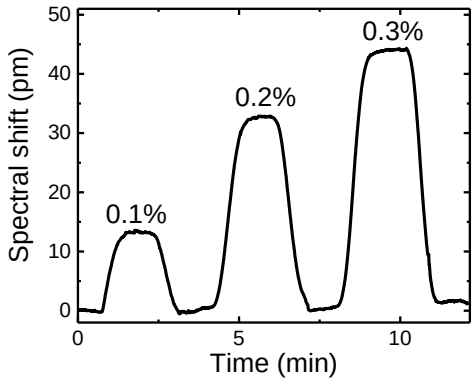

Figure 5-6 Sensorgram of Fano resonance response to ethanol/DI water mixture at different concentrations (v/v) from single-layer PCS with t = 156 nm, a = 970 nm, and r = 103 nm.[112]

5.2 Single-layer 2D PCS liquid sensor

Based on the simulation results of single-layer PCS in 3.3.1, we know that, single-layer PCS with t = 160 nm, a = 1,000 nm, r/a = 0.1, has a Fano resonance mode at 1,580 nm with both high Q factor and high sensitivity. We fabricate single-layer PCS toward this target. The PCS is fabricated on SOI substrate with 156 nm top Si layer from thin-down process as detailed in section 4.1. The PCS is designed to have a lattice constant of 970 nm, in order to shift the Fano resonance mode from 1,580 nm to around 1,550 nm (within the wavelength range of our tunable laser source). The SEM images of fabricated single-layer PCS is shown in Figure 4-5, with t = 156 nm, a = 970 nm, and r = 103 nm. After bonded with PDMS microfluidic channel, the optofluidic PCS sensor is characterized with system illustrated in Figure 5-1.

5.2.1 Q factor of Fano resonance mode

The reflection spectrum of PCS sensor is measured with DI water inside microfluidic channel, *i.e.*, PCS is covered by DI water, and presented in Figure 5-7(b). The Fano fitting method described in 5.1.1.1 is used to fit the reflection spectrum and obtain both resonance position and Q factor. From Fano fitting, it indicates a Fano resonance mode at λ_0 = 1,537.5 nm with a Q factor of 2,828. Numerical analysis of the investigated PCS is also carried out with S^4 software package. In simulation, the lattice parameters of PCS, including slab thickness, lattice constant, and air hole radius, are the same as the fabricated device presented in Figure 4-5. The simulated reflection spectrum is shown in Figure 5-7(a), which predicts the PCS possesses a Fano resonance mode at λ_0 = 1,534.9 nm with a Q factor of 5,429 when immersed in water. The simulated spectral location of PCS Fano resonance mode agrees very well with the measured result. The lower Q factor in experiment can be attributed to imperfections in fabrication and measurement procedures which degrade the Q value from ideal situations assumed in simulation. Considering fabrication defect, the real PCS may have holes with irregular shape and non-uniform Si surface that can severely lower the Q factor. In measurement, the incident beam has a Gaussian profile with a spot size of about 100 μm on the sample that creates non-vanishing lateral wave vectors. The propagation of off-normal wave components in the lateral direction limits the modal lifetime, hence the highest achievable Q factor in experiment.

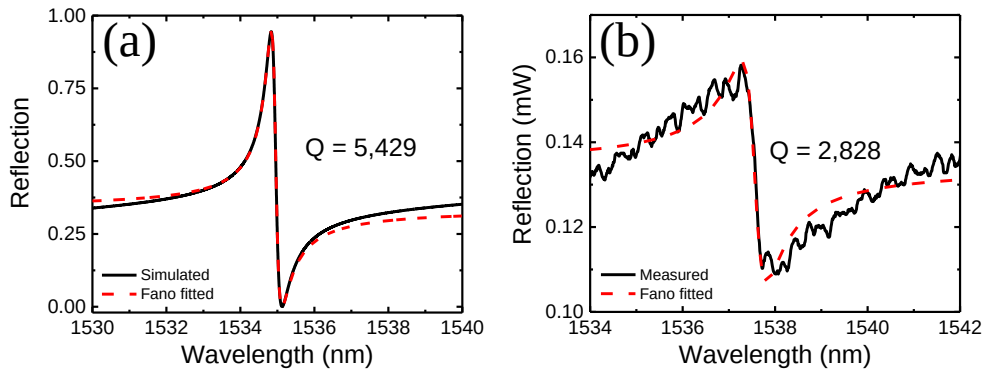

Figure 5-7 (a) Simulated Fano resonance spectrum of single-layer PCS in water environment (black solid) and through Fano fitting (red dash) with the real lattice geometry, t = 156 nm, a = 970 nm, and r = 103 nm. The Q factor from simulation is 5,429. (b) Measured Fano resonance reflection spectrum of single-layer PCS in water environment (black solid) and through Fano fitting (red dash) showing a Q factor of 2,828.[112]

5.2.2 Bulk liquid sensitivity

The bulk liquid RI sensitivity of single-layer PCS sensor is characterized with various concentrations of ethanol/DI water mixture (0.05% - 0.3%, v/v) with known RI. The ethanol/DI water mixture is flowed through the microfluidic channel with a DI water rinsing step between each new concentration to ensure that the chamber is free of residual ethanol, and Fano resonance spectral shift is measured in real-time. The corresponding sensorgram is plotted in Figure 5-8(a), from which it can be clearly seen that, with ethanol concentration increasing, *i.e.*, RI increasing, redshift of Fano resonance mode increases. The respective spectral shift ($\Delta\lambda$) with RI change (Δn) is presented in Figure 5-8(b) and compared to the simulation data calculated with S^4 by tracking resonance shift in

reflection spectrum. The linear fit in Figure 5-8(b) indicates a bulk RI sensitivity of 264 nm/RIU is achieved in experiment, very close to the theoretical prediction of 303 nm/RIU. The discrepancy between simulation and measurement may be due to imperfect shape of air hole from etching process, inaccuracy in Si slab thickness determination, and slight deviation of ethanol concentration in experiment. The smallest RI change measured is 2.8×10^{-5} RIU with 0.05% ethanol. This result represents about two orders of magnitude improvement in the bulk liquid RI sensitivity compared to other PCS based RI sensors reported to date.

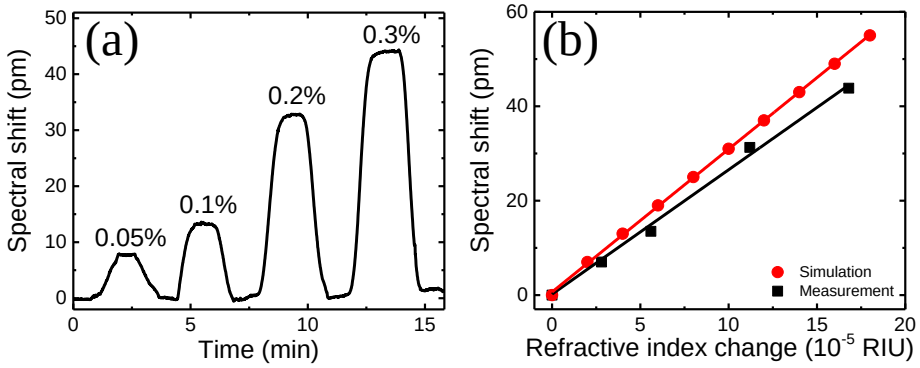

Figure 5-8 Bulk liquid sensing results of single-layer PCS. (a) Sensorgram of Fano resonance spectral response to various concentrations of ethanol/DI water mixture. (b) Theoretical (red) and experimental (black) data of bulk RI sensitivity.[112]

To better understand the sensing capability of PCS sensor, we carry out simulation of modal field distribution with Meep. Figure 5-9 gives the calculated electric field distribution of PCS Fano resonance mode (PCS geometry: t = 156 nm, a = 970 nm, and r = 103 nm). It is noted that the PCS is covered by liquid with RI n = 1.33 in simulation. The field distributions in *yz* and *xy* planes shown in Figure 5-9(b) & (c) reveal

that the modal field mainly concentrates into the Si slab region which has high RI. From Figure 5-9(a), the filling fraction above PCS surface is estimated to be around 25.9%. According to equation (3.5) from perturbation theory, the sensitivity based on field distribution is calculated to be 298 nm/RIU, which is consistent with the calculated *S* by tracking spectral shift with S^4 and the measured one in experiment. In addition, the DL of PCS sensor can be estimated with equation (3.6) using experimental spectral resolution *R*. The spectral resolution depends on the spectral lineshape and the signal-to-noise ratio of experiment system. In contrast to the symmetric Lorentzian lineshape in conventional sensors with cavity mode, Fano resonance PCS sensor demonstrates a much sharper asymmetric Fano lineshape in reflection spectrum, making it advantageous for achieving better DL in practice. Figure 5-10 depicts the measured spectral fluctuation of PCS sensor, which yields a spectral resolution of 0.72 pm. Given that S = 264 nm/RIU from experiment, this spectral resolution leads to a RI DL of 2.7×10^{-6} RIU according to equation (3.6).

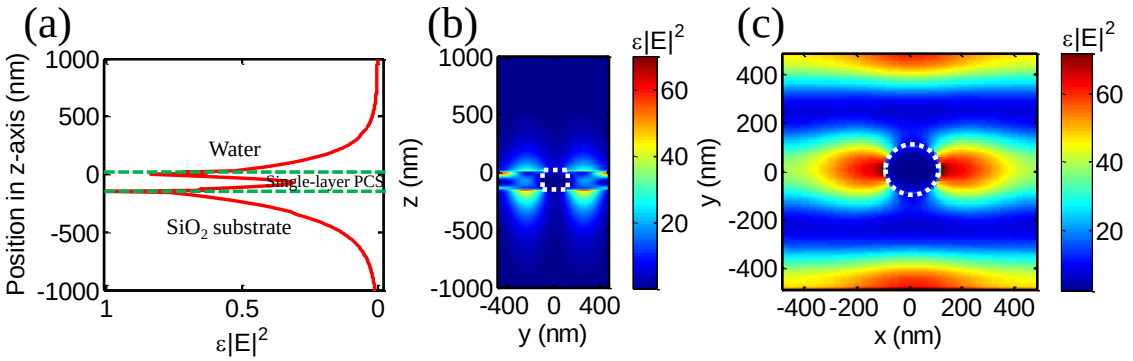

Figure 5-9 Simulated field distribution of Fano resonance mode when single-layer PCS (t = 156 nm, a = 970 nm, and r = 103 nm) is immersed in water (RI n = 1.33). (a) Intensity distribution of electric filed along vertical direction (z-axis). The sensor surface is located at z = 0. (b) and (c) show the mode profile in the yz plane (x = 0) and xy plane (z = 0), respectively. Dashed lines outline the boundary of the air hole.[112]

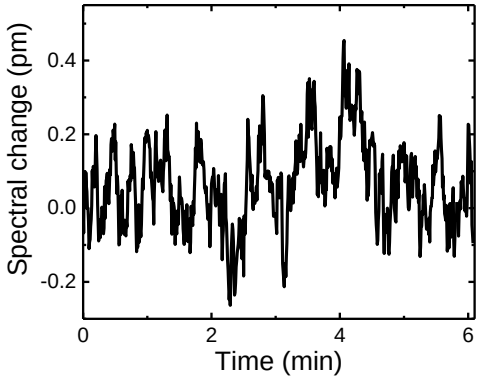

Figure 5-10 Baseline resonance spectral fluctuation of single-layer PCS sensor.[112]

5.3 Coupled double-layer 2D PCS liquid sensor

In chapter 3, the principle of coupled double-layer PCS is presented, in which a dark state with infinite Q factor can be formed by choosing an appreciate spacing

between top and bottom PCS.[107] Small deviation from the critical condition leads to near-dark state with very high Q factor. Simulation results predict that, with 60 nm coupling oxide layer between top and bottom PCSs, a Q factor of around 10^6 can be achieved. We know that, to achieve better sensing performance, *i.e.*, lower DL, both high Q factor and high sensitivity are preferable.[32] Although the sensitivity of coupled double-layer PCS is only a few tens nm/RIU from simulation, the extremely high Q factor can lead to small DL. In this section, we present the sensing performance of fabricated coupled double-layer PCS sensor. We choose double-layer PCS with 160 nm coupling oxide layer as an example to demonstrate the capability of coupled double-layer PCS for sensing purpose. The top and bottom Si layer of designed structure is 230 nm, lattice constant a is 1,000 nm, and hole radius-to-lattice constant ratio (r/a) is 0.1. The designed structure has a Fano resonance mode at λ_0 = 1,457 nm with a high Q factor of 27,664, and the other Fano resonance mode at λ_0 = 1,578 nm with a Q factor of 6,335. The SEM images of fabricated device is presented in Figure 4-6, with top Si layer t_T = 230 nm, bottom Si layer t_B = 222 nm, and coupling oxide layer t_b = 160 nm. After bonded with PDMS microfluidic channel, coupled double-layer PCS sensor is also characterized with system illustrated in Figure 5-1.

5.3.1 Q factor of Fano resonance mode

The reflection spectrum of double-layer PCS is characterized in the same way as that of single-layer PCS sensor. The experimental reflection spectrum is shown in Figure 5-11(b), which presents a Fano resonance mode at λ_0 = 1,541.6 nm with a Q factor of 2,492 from Fano fitting. Numerical result using S^4 software package based on the real lattice geometry indicates a Fano resonance mode at λ_0 = 1,537.4 nm with a Q factor of

3,252, as presented in Figure 5-11(a), which corresponds to the resonance mode at λ_0 = 1,578 nm of the designed structure. Compared the designed result, simulated result with real fabricated structure, and measured result, the high Q mode at λ_0 = 1,457 nm from design is not detected in experiment, due to limited wavelength range of our tunable laser system. Double-layer PCS with larger lattice constant or smaller air hole can be designed and fabricated in order to shift the high Q mode to the wavelength range of our tunable laser system. The measured resonance mode at λ_0 = 1,541.6 nm is corresponding to λ_0 = 1,578 nm mode in design, and λ_0 = 1,537.4 nm mode in simulation with fabricated structure, respectively. The non-symmetry between top and bottom Si layers, larger air hole size, as well as conical shape of air hole from fabrication can account for the lower Q factor in experiment. In addition, the imperfections in measurement described in 5.2.1 limit the experimental Q factor too.

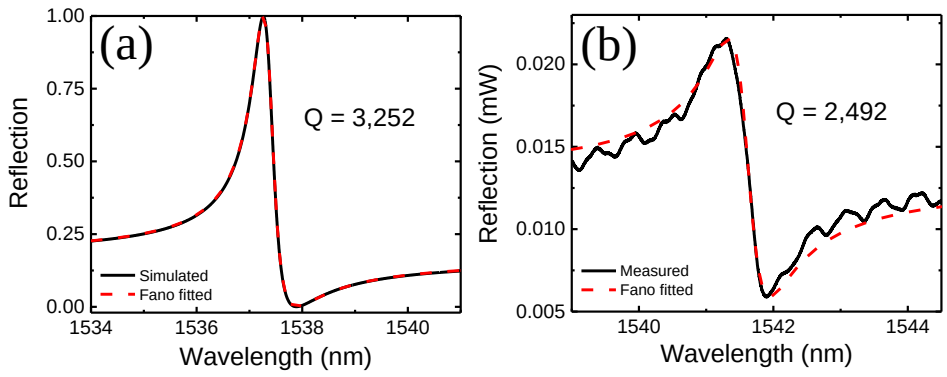

Figure 5-11 (a) Simulated Fano resonance reflection spectrum of coupled double-layer PCS in water environment (black solid) and through Fano fitting (red dash) with the real lattice geometry, t_T = 230 nm, t_B = 222 nm, t_b = 160 nm, a = 1,000 nm, and r = 180 nm. The Q factor from simulation is 3,252. (b) Measured Fano resonance reflection spectrum of coupled double-layer PCS in water environment (black solid) and through Fano fitting (red dash) showing a Q factor of 2,492.

5.3.2 Bulk liquid sensitivity

The bulk liquid RI sensitivity of coupled double-layer PCS sensor is evaluated with various concentrations of ethanol/DI water mixture (0.1% - 2.5%, v/v) with known RI in the similar method as that of single-layer PCS sensor described in 5.2.2. Figure 5-12(a) depicts the reflection spectra measured from various concentrations of ethanol/DI water mixture. Fano lineshaped resonance mode continues shifting to a longer wavelength with increased ethanol concentration, hence RI. The respective spectral shift ($\Delta\lambda$) versus RI change (Δn) is plotted in Figure 5-12(b) and compared to the simulated result with S^4 by tracking resonance shift in reflection spectrum. With linear fitting, the experimental bulk RI sensitivity of 62.8 nm/RIU can be obtained, which is in excellent

agreement with the simulation result of 62.3 nm/RIU. The smallest RI change measured in experiment is 5.6×10^{-5} RIU with 0.1% ethanol, which is of two orders higher than that of single-layer PCS sensor.

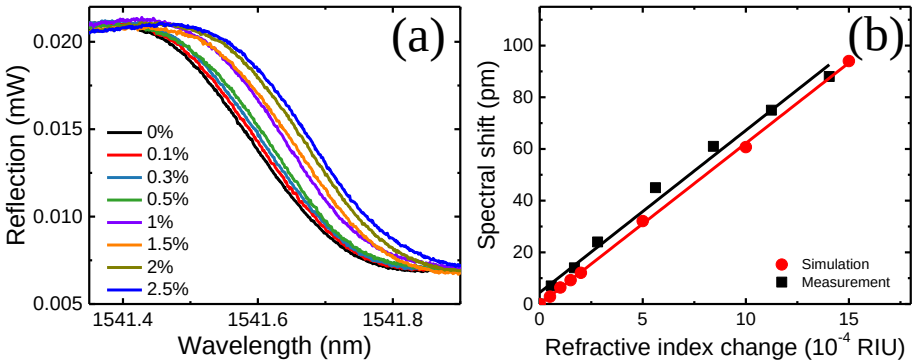

Figure 5-12 Bulk liquid sensing results of double-layer PCS. (a) Fano resonance reflection spectra measured for various concentrations of ethanol/DI water mixture. (b) Theoretical (red) and experimental (black) data of bulk RI sensitivity.

The modal field distribution of fabricated device is studied with Meep too for better understanding the sensing mechanism of coupled double-layer PCS sensor. Figure 5-13 presents the simulated electric field distribution of Fano resonance mode from double-layer PCS sensor. The PCS is immersed in liquid with RI n = 1.33 in simulation. The field distributions in *yz* and *xz* planes indicate that the modal field mainly concentrates into the Si slab and coupling oxide region, which is similar to that of single-layer PCS. Based on electric field distribution along vertical direction (*z*-axis) in Figure 5-13(a), the filling fraction above double-layer PCS surface is calculated to be around 5.9%, resulting in a sensitivity of 68.2 nm/RIU using equation (3.5) from perturbation theory, which is consistent with the measured sensitivity as well as the simulation result

from S^4. Compared with single-layer PCS sensor, the smaller bulk RI sensitivity of double-layer PCS can be attributed to the smaller filling fraction. Since double-layer PCS has a similar Q factor as that of single-layer PCS in experiment, we can assume that the double-layer PCS sensor has the same spectral resolution as that of single-layer PCS, which is shown in Figure 5-10. With R = 0.72 pm and a measured sensitivity of 62.8 nm/RIU, the estimated DL of double-layer PCS sensor is 1.1×10^{-5} RIU, which is four times higher than that of single-layer PCS sensor. The high DL of double-layer PCS sensor is due to lower bulk RI sensitivity. To improve the DL, double-layer PCS with high Q resonance mode can be fabricated in the future, *e.g.*, PCS with 60 nm coupling oxide layer.

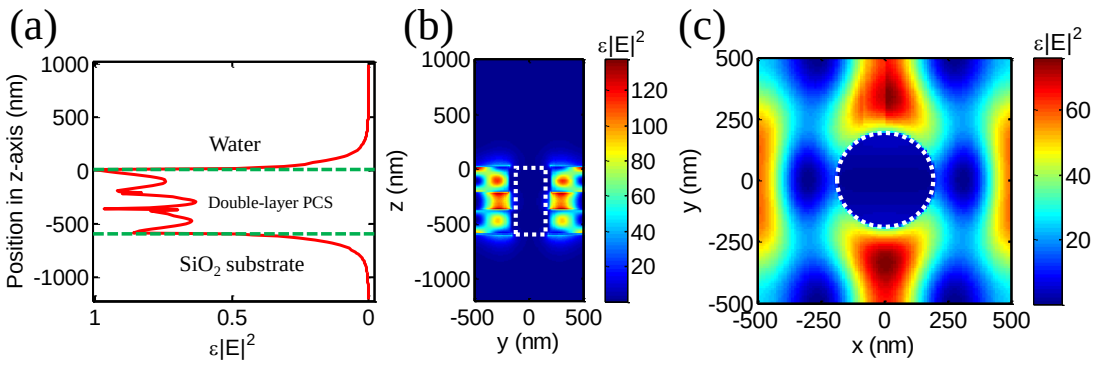

Figure 5-13 Simulated field distribution of Fano resonance mode when double-layer PCS (t_T = 230 nm, t_B = 222 nm, t_b = 160 nm, a = 1,000 nm, and r = 180 nm) is immersed in water (RI n = 1.33). (a) Intensity distribution of electric filed along vertical direction (z-axis). The sensor surface is located at z = 0. (b) and (c) show the mode profile in the yz plane (x = 0) and xy plane (z = 0), respectively. Dashed lines outline the boundary of the air hole.

5.4 Conclusion

In this chapter, the measurement procedure and data analysis method of 2D PCS liquid sensor were discussed. The reflection spectrum of PCS sensor is characterized with a tunable laser system at surface normal incidence. The surface normal incidence measurement system eliminates delicate alignment for light coupling and is advantageous for system miniaturization as well as scaling up into multiplexed sensing arrays for many lab-on-a-chip applications. Fano resonance spectrum is fitted through Fano fitting, from which the resonance position and Q factor can be determined. The sensitivity of PCS sensor is evaluated with various concentrations of ethanol/DI water mixture, and the DL of the sensor is estimated with the experimental spectral resolution.

Both single-layer and coupled double-layer PCS were characterized. The experimental results show that single-layer and coupled double-layer PCS have similar Q factor, while the sensitivity of single-layer PCS is four times higher than that of double-layer PCS, as a result of much better DL from single-layer PCS sensor. Electric field distributions calculated with Meep based on FDTD method indicate that the filling fraction above PCS surface of single-layer PCS sensor is 25.9%, while the filling fraction of double-layer PCS sensor is only 5.9%. The larger filling fraction of single-layer PCS results in larger bulk RI sensitivity, and hence better DL. Although the sensitivity of double-layer PCS is much smaller, simulation indicates extremely high Q factor (10^6) by tuning the spacing between top and bottom Si layers can achieved. Future work should focus on improving the fabrication process in order to have higher Q factor and fabricating double-layer PCS with a coupling oxide layer of 60 nm that possesses extremely high Q factor.

Chapter 6

Chemical Vapor Detection with Fano Resonance 2D PCS

6.1 Motivation of chemical vapor detection with 2D PCS

Detection of volatile organic compounds (VOCs) has wide applications in homeland security, environmental monitoring, and healthcare.[121, 122] Quantitatively analytical techniques, such as chromatography with mass spectrometry and flame ionization detector, nuclear magnetic resonance, have been widely employed for sensitive VOCs detection.[122, 123] While showing excellent detection specificity and sensitivity, they have drawbacks, like bulky, lack of portability, high power consumption, and low throughput. Compact, miniaturized, and multiplexed on-chip sensor arrays with high sensitivity, selectivity, as well as fast response are desired for the next generation of gas detection. With advances in microanalytical systems, a variety of microsensors has been explored for gas detection, including acoustic sensors[124-127], electrical sensors[128-131], and optical sensors[12, 132], each with their own merits and demerits. Especially, optical structures based sensors are one of the most promising and powerful technologies for gas detection and analysis. Compared to other sensing technology, optical sensors are immune to electromagnetic interference, and therefore can be applied in sensitive environments. Also, optical sensors can be implemented through a variety of signal transduction pathways based on the photonic contributes, including absorbance, transmission, polarization, reflectivity, RI, and Raman scattering. Through years of research, a variety of optical structures has been studied for vapor sensing, including SPR[12, 133-137], fiber Bragg gratings (FBGs)[138-140], long period fiber gratings (LPFGs)[141], D-shaped optical fibers[142-144], ring resonators[145-149], Fabry-Pérot

cavities[150-152], and PhCs[153-169]. Several configurations of optical structure based vapor sensors are shown in Figure 6-1. While sensitive, the SPR based sensors are relatively bulky and the measurement system is quite complicated. The fiber gratings and D-shaped fibers suffer from significant fiber loss as well as alignment loss. There are two configurations of ring resonators that have developed for vapor sensing, chip based ring resonators and capillary based ring resonators. Although showing excellent detection capability, chip based ring resonators come with very large gas cell (liters range), as a result of very long response time. Capillary based ring resonators integrate the ring resonator with microfluidics naturally, and demonstrate high sensitivity and selectivity for vapor sensing. However, the reproducibility and robustness of those ring resonators need to be worked out. Fabry-Pérot cavity based sensors are robust and present excellent sensing capability, while the sensitivity depends on the angle of incident light and complicated calibration procedures are required.

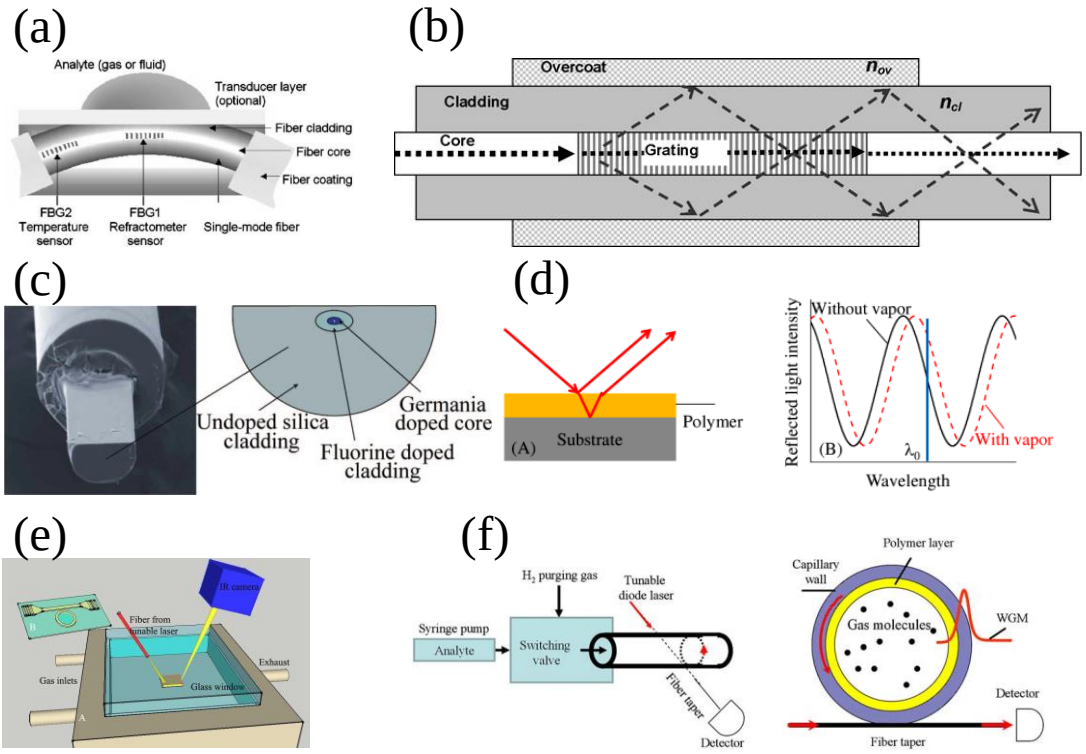

Figure 6-1 Configurations of optical structure based vapor sensors. (a) Fiber Bragg gratings.[139] (b) Long period fiber gratings.[141] (c) D-shaped optical fiber.[144] (d) Fabry-Pérot cavity.[152] (e) Chip based ring resonator.[148] (f) Capillary based ring resonator.[147]

Studies of PhCs as gas sensors have also been performed, most of which are based on photonic crystal fibers (PCFs). In general, there are two kinds of PCFs: PCFs with solid core in which light guiding is based on TIR effect[154], and PCFs with hollow core in which light guiding depends on PBG effect[162], as shown in Figure 6-2. When gas molecules are filled into PCFs voids, light of certain wavelengths will be absorbed depending on the absorption lines of the analytes, as a result that the transmission spectrum of PCFs is changed. The sensitivity of PCFs based gas sensors relies on the

absorption coefficient and the overlap between optical mode and gas molecules. As a new class of gas sensor, PCFs sensors have advantages of flexible, robust, and allowing for remote and distributed sensing. However, it usually needs vacuum or pumping systems to fill gas molecules into PCFs voids.[162, 169] In order to have sufficient absorption, PCFs typically have a length of tens centimeters or even several meters, resulting in pretty long response and evacuation time (typically tens of minutes).[162, 169] In addition, it is difficult to perform low concentration measurement with PCFs due to weak light-matter interaction resulted from poor overlap between optical mode and analytes.[162, 169]

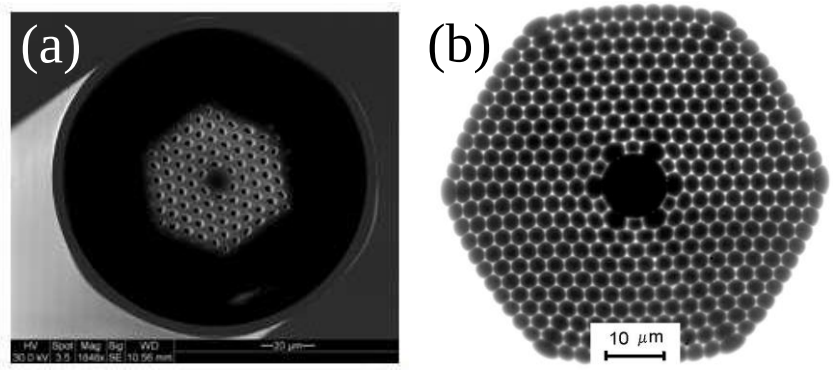

Figure 6-2 Configurations of PCFs gas sensor. (a) PCFs with solid core in which light guiding is based on TIR effect.[154] (b) PCFs with hollow core in which light guiding depends on PBG effect.[162]

As one type of optical label-free sensor, planar PhCs have been widely employed for liquid and biomolecule detection, and demonstrated excellent sensing performance, owning to its unique light confinement provided by PBG effect and enhanced light-matter interaction at the nano-scale to sub-micron scale dimension, as detailed in Chapter 2. In this chapter, we develop a novel chemical vapor sensor using ultra-compact 2D PCS, which relies on Fano resonance for light coupling and uses the sharp dip-to-peak

transition in Fano lineshaped spectrum for extracting spectral shift induced from perturbation of vapor molecules. Two configurations of PCS are studied for vapor sensing in this dissertation, single-layer and coupled double-layer PCS. The vapor sensing capability of PCS is investigated experimentally and theoretically.

6.2 Vapor sensing principle of 2D PCS

Shown in Figure 6-3(a) is the schematic of 2D PCS based vapor sensor which is composed of a Si PC with a thin layer of polymer on SOI substrate.[170] In 2D PCS, the in-plane guided resonance modes above the light line can be coupled with the out-of-the-plane radiation modes due to phase-matching provided by the periodic lattice structure, which is known as Fano resonance.[39] The evanescent field tail of Fano resonance mode outside the slab plane is sensitive to the RI change near PCS surface, and thus PCS is well suitable for RI based sensing applications. As different polymers (such as polar and nonpolar polymers) may have drastically different response to vapor analytes, it is very common to incorporate a polymer layer into a vapor sensor to enhance the detection sensitivity and specificity. When the PCS is exposed to vapor analytes, the vapor molecules can be either adsorbed to the polymer surface to increase the RI near the surface or absorbed by the polymer to cause a change of polymer thickness and/or RI, as a result of Fano resonance spectral shift, as illustrated in Figure 6-3(b). Therefore, by monitoring the Fano resonance spectrum in real-time, PCS based vapor sensor can provide quantitative and kinetic information about the vapor flow inside the gas chamber. As a kind of vapor sensor, Fano resonance PCS has a number of distinctive advantages over other optical structures. Firstly, in contrast to traditional Lorentzian lineshape from other optical structures, Fano resonance of 2D PCS offers an asymmetric lineshape in the

reflection and transmission spectrum. The sharp dip-to-peak transition is advantageous for extracting small spectral shift induced from small concentration analyte, hence better DL can be achieved. Secondly, since Fano resonance is the coupling effect of in-plane guided resonance modes to the out-of-the-plane radiation modes, it provides an efficient and easy way to channel light from within the slab to the external environment, which can simply the measurement system. Thirdly, Fano resonance 2D PCS can be easily fabricated with existing microfabrication technologies and scaled up into an array format for multiplexed sensing on chip. Also, various polymers can be coated onto PCS sensor array and respond differently to analytes, hence improving the vapor detection selectivity. Finally, Fano resonance 2D PCS is highly compatible with micro-gas chromatography (μGC) technology, and can be easily integrated with μGC components, like preconcentrators and separation columns, thus making it attractive for developing compact and miniaturized μGC systems on chip.

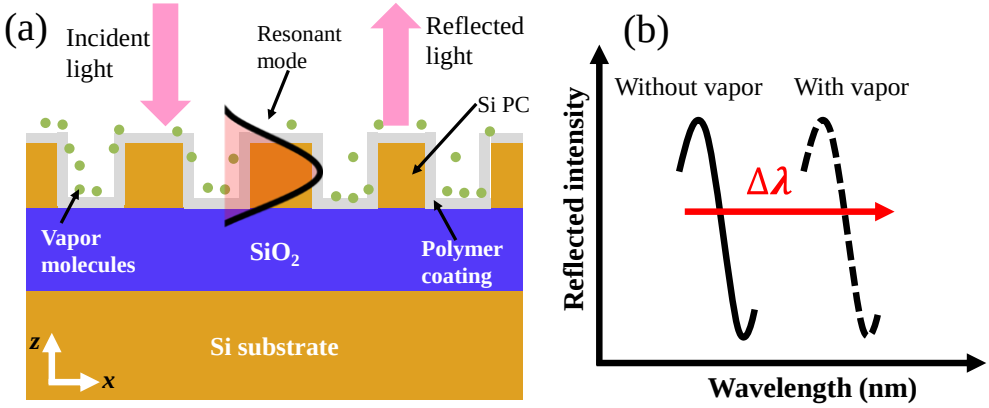

Figure 6-3 (a) Schematic of 2D PCS based gas sensor on SOI substrate. The adsorption of vapor analytes into polymer results in a change of polymer thickness and/or RI, which in turn leads to a shift of resonance wavelength. (b) Example of the resonance wavelength shifting due to vapor adsorption.[170]

6.3 Vapor sensing with 2D PCS

6.3.1 Sensor preparation

Both single-layer and coupled double-layer PCS are fabricated with EBL and RIE process as detailed in Chapter 4. The single-layer PCS has a top Si layer of 251 nm, lattice constant of 970 nm, and air hole radius of 83 nm, as seen from the SEM images in Figure 6-4. The SEM images of fabricated double-layer PCS for vapor sensing are presented in Figure 6-5, showing the three layer structure, t_T = 213 nm, t_B = 240 nm, t_b = 167 nm, with a = 1,000 nm and r = 160 nm. And then the fabricated PCS is coated with two different vapor sensitive polymers, nonpolar dimethylsilicone (OV-101, Ohio Valley Specialty) and highly polar polyethylene glycol (PEG) 1,000 (Sigma-Adlrich) for differentiating different types of chemical vapors. Both of them have been widely used for VOCs detection and GC. The polymer is deposited onto PCS surface by dip coating method. In brief, the polymer is dissolved in organic solvents, like methanol and toluene. PCS chip is immersed in polymer solution for 1 hour and dried at room temperature for 2 hours. The coating thickness is estimated to be around 5 nm for both OV-101 and PEG 1,000 with 15 mg/mL coating solution. All the coating processes are performed at room temperature. After coating, the PCS is checked using microscope to ensure smooth and uniform surface, since the surface quality of PCS is of critical importance for sensing performance. Rough surface may induce additional scattering loss, which will degrade the Q factor, and hence the DL of PCS vapor sensor.

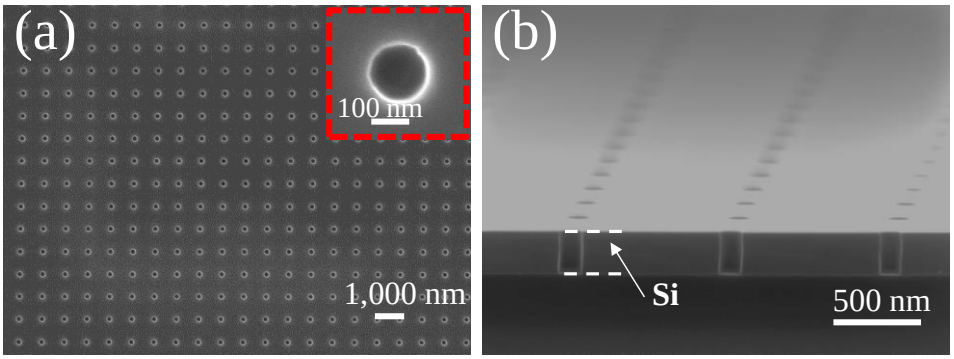

Figure 6-4 SEM images of fabricated single-layer PCS on SOI substrate: (a) Top view SEM image showing lattice constant a = 970 nm and air hole radius r = 83 nm. Inset shows the zoomed-in image of air hole. (b) Cross-sectional view SEM image of PCS showing slab thickness t = 251 nm.[170]

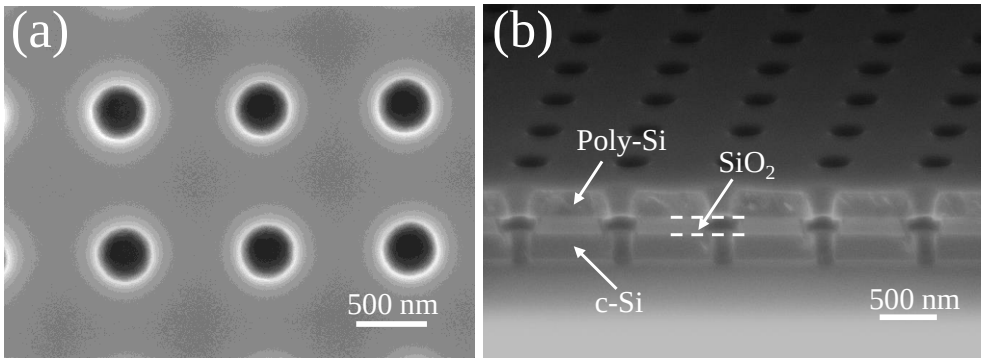

Figure 6-5 SEM images of fabricated double-layer PCS on SOI substrate. (a)Top view showing lattice constant a = 1,000 nm, and air hole radius r = 160 nm. (b) Cross-sectional view showing top layer PCS (t_T = 213 nm) and bottom layer PCS (t_B = 240 nm) separated by a coupling oxide layer (t_b = 167 nm).

After coating polymer onto PCS surface, the chip is placed in a glass cell with 2 mm inner width and 6 mm inner height (Friedrich & Dimmock, BRT-2-6-70) which

serves as the gas fluidic cell. Two short segments of fused-silica capillary (Polymicro Technologies, ID = 535 μm) that serve as gas inlet and exhaust are inserted into the glass cell and sealed with UV-curable glue. The schematic of PCS based vapor sensor is illustrated in Figure 6-6(a). One protype of PCS vapor sensor in glass cell is shown in Figure 6-6(b). The gas cell has a total volume of 0.1 mL, which is much smaller than most gas sensors reported. Such small gas cell will dramatically reduce the sensor response time with similar flow rate as other sensors.

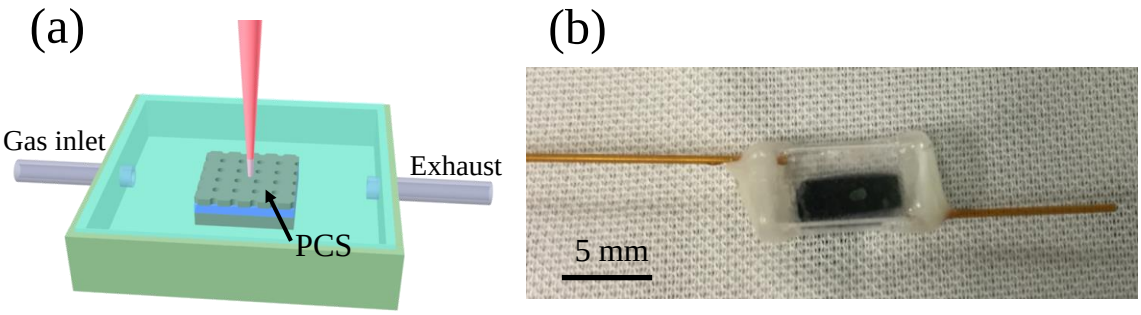

Figure 6-6 (a) Schematic of PCS based vapor sensor with gas cell (not to scale). (b) Image of real PCS vapor sensor in the glass cell (Friedrich & Dimmock, BRT-2-6-70, inner width is 2 mm, and inner height is 6 mm). Two short segments of fused-silica capillary (Polymicro Technologies, ID = 535 μm) that serve as gas inlet and exhaust are inserted into the glass cell and sealed with UV-curable glue. The total volume of gas cell is 0.1 mL.

6.3.2 Chemical vapor sensing

In this section, the vapor sensing capability of PCS is investigated. In our experiment, hexane and ethanol vapors are employed to represent nonpolar and polar analytes, respectively. The experimental setup is the same as that used for bulk liquid

sensing (see Figure 5-1). Various concentrations of analyte/air mixture are injected into the gas chamber with syringe by hand. Air is applied to purge the analyte after sensing. All the measurement is done at atmospheric pressure. When the vapor molecules are injected into the gas cell, the interaction between vapor molecules and polymer causes the thickness and/or RI change of polymer layer, resulting in Fano resonance spectral shift. The spectral position of Fano resonance is measured in real-time with Labview program at a rate of 1.4 Hz.

6.3.2.1 Vapor sensing with single-layer 2D PCS

Before coating vapor sensitive polymer, Fano resonance reflection spectrum of single-layer PCS is characterized and compared with simulation, which is presented in Figure 6-7. The simulation is performed with S^4 software package using the actual lattice geometry suggested from the SEM images in Figure 6-4. In experiment, we observe a Fano resonance mode at λ_0 = 1,515 nm with a Q factor of 1,833, as shown in Figure 6-7(b). Compared to simulation, the low Q factor from experiment may come from the imperfections in fabrication, like irregular hole shape and non-uniform Si surface. After coated with polymer, Fano resonance reflection spectrum of PCS sensor is characterized again, which keeps similar Q factor as before coating.

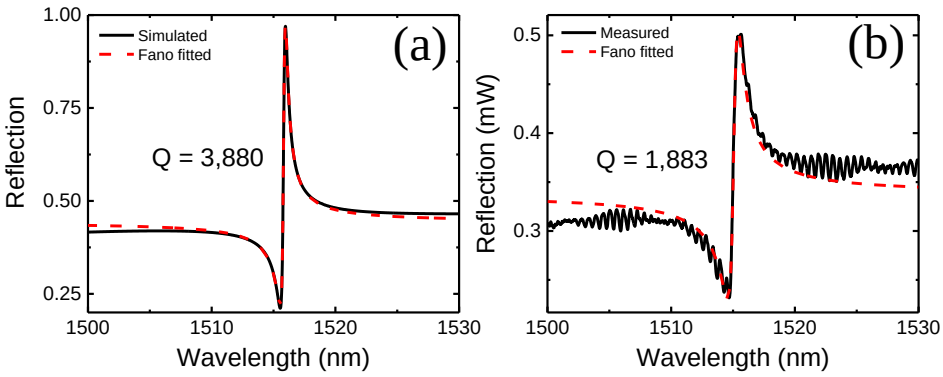

Figure 6-7 Fano resonance reflection spectra of single-layer PCS vapor sensor. (a) Simulated reflection spectrum of Fano resonance PCS (black solid) and through Fano fitting (red dash) with lattice geometry, t = 251 nm, a = 970 nm, and r = 83 nm. The calculation indicates a Fano resonance mode at 1,515.8 nm with a Q factor of 3,880. (b) Experimental reflection spectrum of Fano resonance PCS at normal incidence (black solid) and through Fano fitting (red dash). A Fano resonance mode at 1,515 nm with asymmetric lineshape is observed, demonstrating a Q factor of 1,883.[170]

The response of single-layer PCS to vapor analytes is evaluated with the method mentioned above, and we continue tracking the sensor response in three days. Figure 6-8 presents the sensorgrams when hexane or ethanol vapor is introduced to an OV-101 coated single-layer PCS, and Figure 6-9 shows the sensorgrams when hexane or ethanol vapor is introduced to a PEG 1,000 coated single-layer PCS. Air is initially filled into gas cell to establish the baseline. Then certain concentration of hexane or ethanol analyte is flowed into the gas chamber. Fano resonance mode is shifted to a longer wavelength upon the interaction with vapor molecules and reaches equilibrium in a few seconds. And then air is flowed into the chamber again to purge the vapor analyte, as reflected by the

blue shift of Fano resonance spectral position. The rapid, efficient, and stable nature of PCS vapor sensor is reflected from the sensorgrams. First, the sensor response reaches equilibrium in a few seconds, which is much faster than that of PCFs based sensors. Second, the purge process takes only a few seconds, and the polymer is fully regenerated, as evidenced by the fact that Fano resonance returns to the baseline every time after purge, which is advantageous to other optical sensors that the response is not reversible. Furthermore, the response of the sensor to analyte is consistent in three days, which demonstrates that the sensor is very stable and robust in long term.

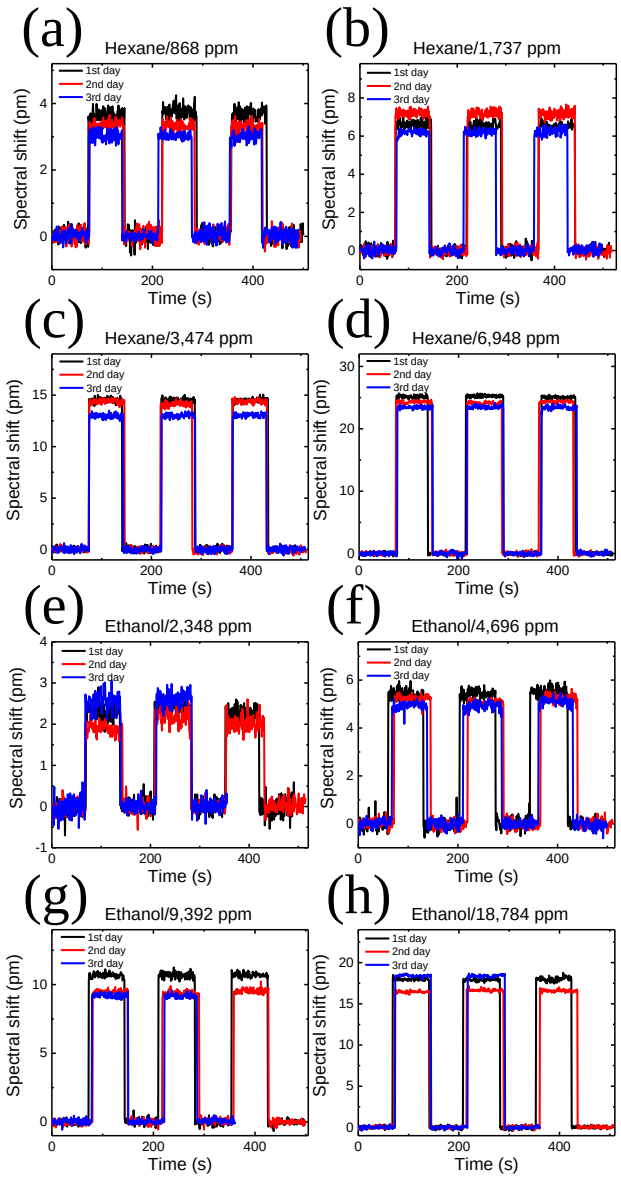

Figure 6-8 Sensorgrams of Fano resonance spectral response to various concentrations of hexane (a-d) and ethanol (e-h) vapors in three days when single-layer PCS is coated with 15 mg/mL OV-101.

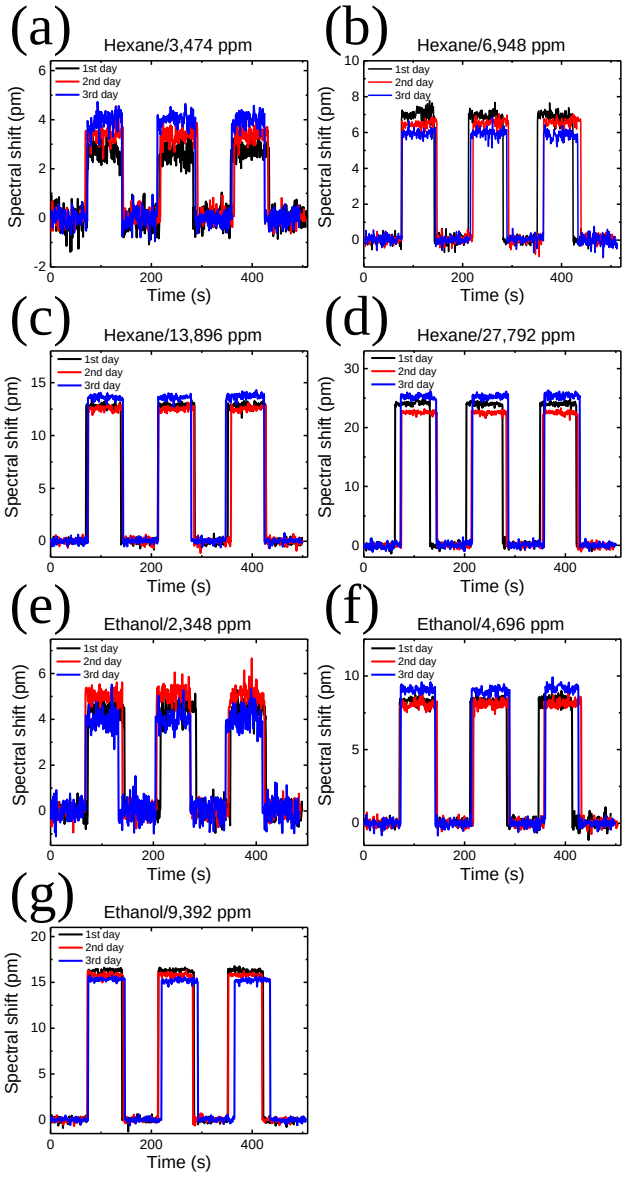

Figure 6-9 Sensorgrams of Fano resonance spectral response to various concentrations of hexane (a-d) and ethanol (e-g) vapors in three days when single-layer PCS is coated with 15 mg/mL PEG 1,000.

Figure 6-10 depicts the Fano resonance spectral shift acquired at equilibrium for various concentrations of hexane and ethanol vapors when the single-layer PCS is coated with OV-101 (Figure 6-10(a)) and PEG 1,000 (Figure 6-10(b)), respectively. According

to Figure 6-10, it is indicated that the resonance shift is almost linear to vapor concentration within 10^2 ppm to 10^4 ppm. For OV-101 coated single-layer PCS sensor, the sensitivity for hexane vapor is 3.2×10^{-3} pm/ppm, four times higher than that for ethanol vapor which is expected, since OV-101 is nonpolar polymer and has higher solubility for hexane vapor that has smaller polarity. Using 1 pm resolution of Fano resonance mode which is typical for the PCS with a Q factor of 2,000, the DL for hexane vapor is estimated to be 312 ppm. In comparison, when the PCS is coated with PEG 1,000, the sensitivity for ethanol vapor is 1.4×10^{-3} pm/ppm, almost two times higher than that for hexane vapor, as PEG 1,000 is highly polar polymer and has more interaction with ethanol vapor which has higher polarity compared to hexane vapor. The estimated DL for ethanol vapor is 714 ppm.

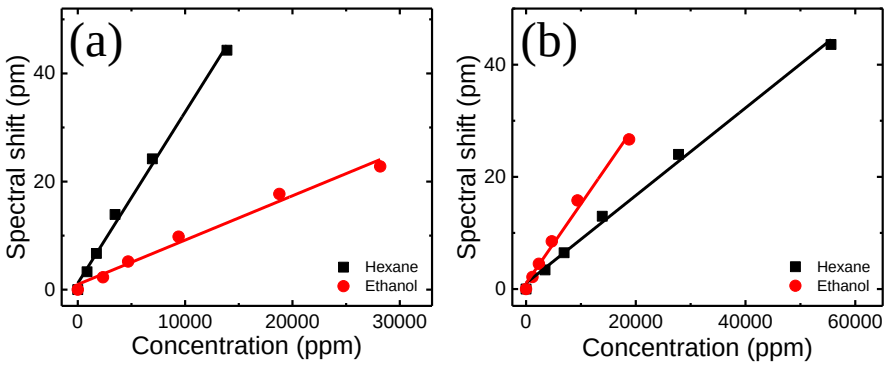

Figure 6-10 Vapor detection at the sharp dip-to-peak transition region of Fano resonance reflection spectrum. Fano resonance spectral shift versus vapor concentration when single-layer PCS is coated with OV-101 (a) and PEG 1,000 (b) at a concentration of 15 mg/mL. Hexane and ethanol vapors are selected to represent nonpolar and polar analytes.[170]

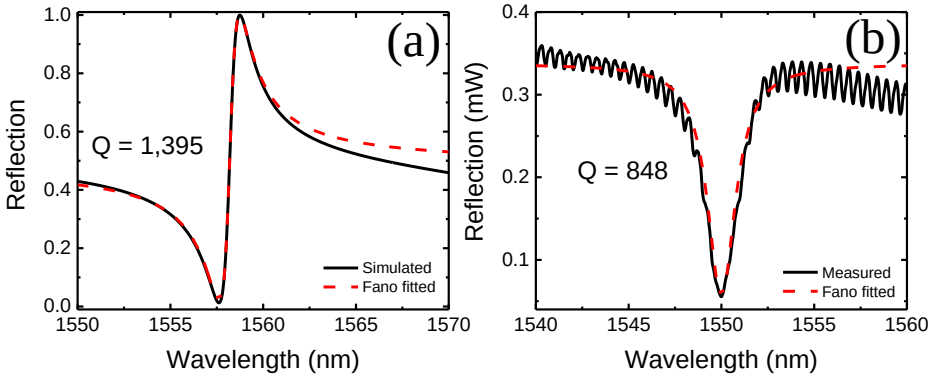

Figure 6-11 Fano resonance reflection spectra of double-layer PCS vapor sensor. (a) Simulated reflection spectrum of Fano resonance PCS (black solid) and through Fano fitting (red dash) with lattice geometry, t_T = 213 nm, t_B = 240 nm, t_b = 167 nm, a = 1,000 nm, and r = 160 nm. The calculation indicates a Fano resonance mode at 1,558.2 nm with a Q factor of 1,395. (b) Experimental reflection spectrum of Fano resonance PCS at normal incidence (black solid) and through Fano fitting (red dash). A Fano resonance mode at 1,550 nm with asymmetric lineshape is observed, demonstrating a Q factor of 848.

6.3.2.2 Vapor sensing with double-layer 2D PCS

Similar to that of single-layer PCS sensor discussed above, Fano resonace reflection spectrum of double-layer PCS is characterized experimentally and compared with simulated result from S^4, which is shown in Figure 6-11. In experiment, a Fano resonance mode at λ_0 = 1,550 nm with a Q factor of 848 is observed, which is presented in Figure 6-11(b). Compared to simulation in Figure 6-11(a) which predicts a resonance mode at λ_0 = 1,558.2 nm with a Q factor of 1,395, the low Q factor from experiment may come from the imperfections in fabrication, like irregular hole shape and non-uniform Si

surface. After coated with polymer, Fano resonance reflection spectrum of double-layer PCS sensor is characterized again, which keeps similar Q factor as before coating.

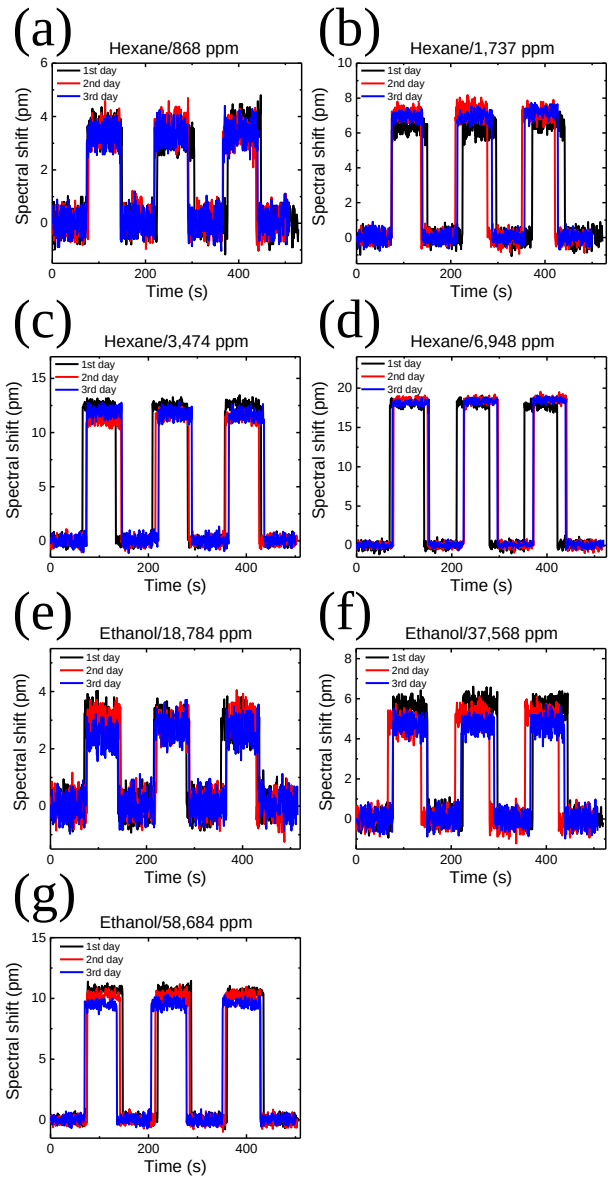

Figure 6-12 Sensorgrams of Fano resonance spectral response to various concentrations of hexane (a-d) and ethanol (e-g) vapors in three days when double-layer PCS is coated with 15 mg/mL OV-101.

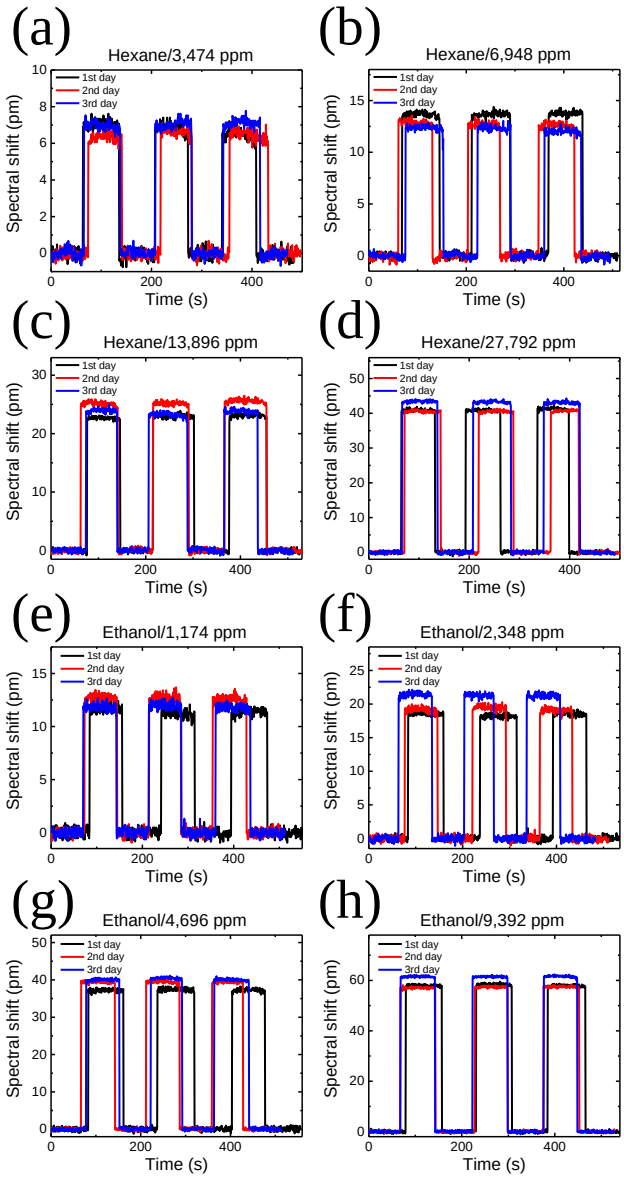

Figure 6-13 Sensorgrams of Fano resonance spectral response to various concentrations of hexane (a-d) and ethanol (e-h) vapors in three days when double-layer PCS is coated with 15 mg/mL PEG 1,000.

The response of double-layer PCS to vapor analytes is characterized in the same way as that of single-layer PCS. The corresponding sensorgrams are plotted in Figure 6-12 (OV-101 coated double-layer PCS) and Figure 6-13 (PEG 1,000 coated double-layer

PCS), respectively. Pretty similar behavior to that of single-layer PCS is observed from double-layer PCS vapor sensor. The Fano resonance spectrum shifts to a longer wavelength with the introduction of vapor analyte, and returns to baseline quickly after purge process with air. The sensor response is very fast, fully reversible, and quite stable in three days.

Figure 6-14 presents the Fano resonance spectral shift acquired at equilibrium for various concentrations of hexane and ethanol vapors when the double-layer PCS is coated with OV-101 (Figure 6-14(a)) and PEG 1,000 (Figure 6-14(b)), respectively. As expected, the resonance shift is almost linear to vapor concentration within 10^2 ppm to 10^4 ppm. OV-101 coated double-layer PCS has a sensitivity of 2.6×10^{-3} pm/ppm to hexane vapor, which is much higher than that for ethanol vapor, owning to the higher solubility of OV-101 for hexane vapor. PEG 1,000 coated double-layer PCS has a sensitivity of 6.18×10^{-3} pm/ppm to ethanol vapor, which is four times higher than that for hexane vapor, due to lower solubility of PEG 1,000 to hexane that possess smaller polarity. Using the 1.8 pm resolution of Fano resonance mode which is typical for the PCS with a Q factor of around 1,000 (shown in Figure 6-15), the DL for hexane vapor is estimated to be 692 ppm, and the estimated DL for ethanol vapor is 291 ppm.

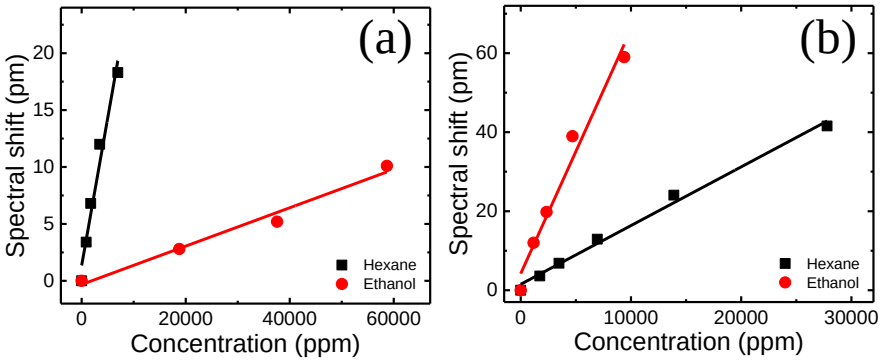

Figure 6-14 Vapor detection at the sharp dip-to-peak transition region of Fano resonance reflection spectrum. Fano resonance spectral shift versus vapor concentration when double-layer PCS is coated with OV-101 (a) and PEG 1,000 (b) at a concentration of 15 mg/mL. Hexane and ethanol vapors are selected to represent nonpolar and polar analytes.

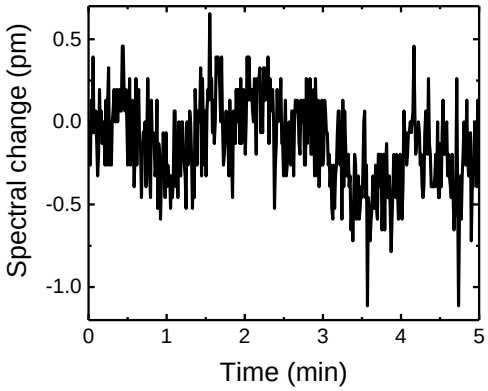

Figure 6-15 Baseline resonance spectral fluctuation of double-layer PCS vapor sensor.

6.4 Theoretical study of vapor sensing performance

Fundamentally, the sensitivity of RI based vapor sensor is determined by the strength of light-matter interaction, which relies on the overlap between analyte and the optical modal field in polymer layer. Therefore, it is of essential importance to

understand the modal field distribution of PCS and calculate the fraction of light in polymer layer which is responsible for the sensor response. In this section, we will calculate the optical modal field of the PCS sensor based on FDTD method by using Meep, and the sensitivity prediction is carried out with S^4 software package which is based on FMM as detailed in Chapter 3. We will compare the simulation with experimental results presented in section 6.3 and provide guidelines for the design of PCS based vapor sensors.

6.4.1 Theory

Since the polymer undergoes RI and/or thickness change when interacting with vapor molecules, the spectral shift of Fano resonance PCS sensor can be expressed as following[149]:

$$\Delta\lambda = \frac{\partial\lambda}{\partial n_{\text{polymer}}}\Delta n_{\text{polymer}} + \frac{\partial\lambda}{\partial t}\Delta t \tag{6.1}$$

where t is the thickness of polymer layer, $\left[\frac{\partial\lambda}{\partial n_{\text{polymer}}}\Delta n_{\text{polymer}}\right]$ refers to the resonance spectral shift due to polymer RI change, and $\left[\frac{\partial\lambda}{\partial t}\Delta t\right]$ represents the resonance spectral shift from polymer swelling. The RI change of polymer can be caused from either the polymer volume change induced by vapor molecules, or the doping effect due to the presence of vapor molecules in the polymer matrix.

The RI sensitivity for polymer RI change, S_{RI}, is determined by the filling fraction of light in the polymer layer and can be written as[149]:

$$S_{\text{RI}} = \frac{\lambda}{n_{eff}} f \tag{6.2}$$

where n_{eff} is the effective RI of polymer layer, and f is the filling fraction of light in polymer layer. The RI change due to polymer volume change can be determined experimentally, while the RI change due to doping effect can be estimated using the Lorentz-Lorentz model[137, 149]:

$$\Delta n = \frac{\left({n_{\text{polymer}}}^2 + 2\right)^2}{6n_{\text{polymer}}} \times \frac{N_A \alpha}{3\varepsilon_0}\rho \tag{6.3}$$

where α is the vapor molecule polarizability, n_{polymer} is the RI of polymer, N_A is the Avogadro's number, ε_0 is the dielectric constant of vacuum, and ρ is the vapor molecule density in polymer layer.

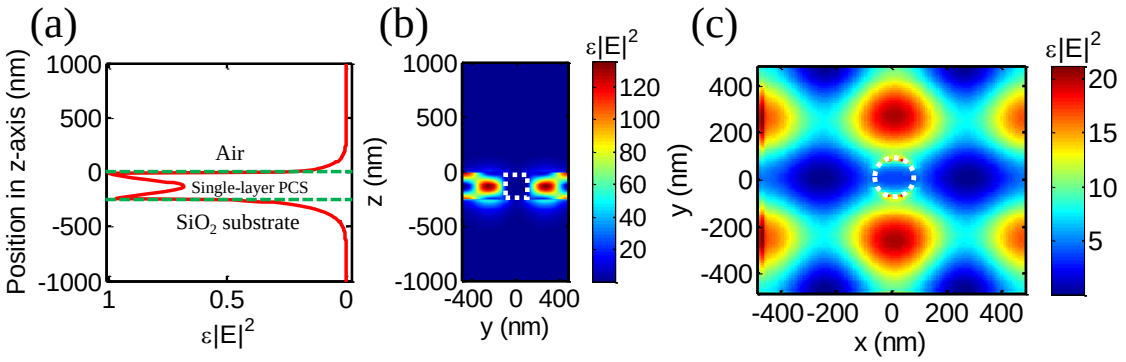

Figure 6-16 Simulated field distribution of single-layer PCS: t = 251 nm, a = 970 nm, and r = 83 nm. (a) Intensity distribution of electric filed along vertical direction (z-axis). (b) and (c) show the mode profile in the yz plane (x = 0) and xy plane (z = 0), respectively. Dashed lines outline the boundary of the air hole.[170]

6.4.2 Theoretical analysis of single-layer 2D PCS vapor sensor

The modal field distribution of the investigated single-layer PCS sensor is shown in Figure 6-16. Based on the integrated electric field distribution along vertical direction (z-axis) in Figure 6-16(a), the evanescent field above PCS surface decays exponentially,

and then becomes zero at a distance of 200 nm away from PCS surface. The filling fraction above PCS surface is calculated to be around 5.57%. From the field distributions in *yz* and *xy* plane shown in Figure 6-16(b) and (c), the modal field is mainly concentrated into the Si slab region that has higher RI, and the filling fraction in air hole region is estimated to be 0.21%, which is much smaller than the filling fraction above PCS surface. Thus, in the sensitivity calculation, we assume that there is no polymer filled into air hole.

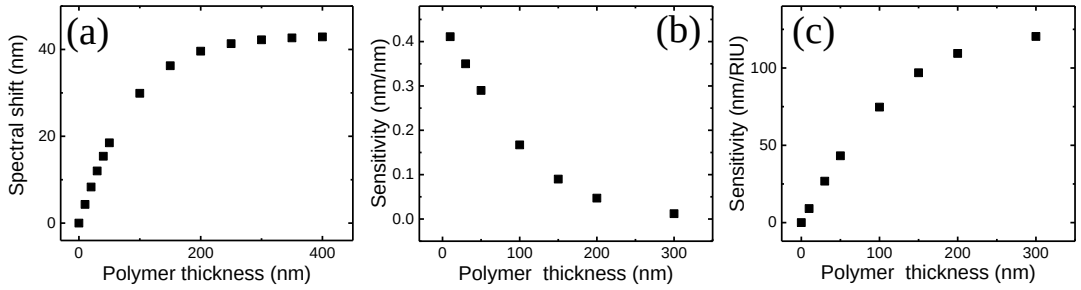

Figure 6-17 Numerical study of the sensing capability for single-layer PCS vapor sensor with polymer coating. In simulation, the RI of polymer is 1.46, and the lattice geometry of PCS is t = 251 nm, a = 970 nm, and r = 83 nm. (a) Fano resonance spectral shift as a function of polymer thickness above PCS surface. (b) Polymer thickness sensitivity as a function of polymer thickness above PCS surface. (c) RI sensitivity as a function of polymer thickness above PCS surface.[170]

Figure 6-17(a) shows the Fano resonance spectral shift of single-layer PCS as a function of polymer thickness above PCS surface. This spectral shift increases as polymer thickness increases and starts saturating when the polymer thickness is more than 200 nm, which is in good agreement with the calculated modal field distribution in

Figure 6-16. The thickness sensitivity, $\left[\frac{\partial\lambda}{\partial t}\right]$, as a function of polymer thickness above PCS surface in Figure 6-17(b) is deduced from the slope of each data point in Figure 6-17(a). The polymer thickness sensitivity of PCS is always positive, indicating that Fano resonance shifts to a longer wavelength when the polymer swells. However, it drops gradually to zero when polymer thickness increases, which means that the PCS sensor is no longer sensitive to the change of polymer thickness. It can be explained by the optical modal field distribution of PCS. When the polymer is sufficiently thick (*e.g.*, > 200 nm), the modal field concentrates into Si slab as well as polymer layer and there is no evanescent field extending out of the polymer layer, the overlap between polymer and the fraction of light becomes constant even with polymer thickness increasing.

We also simulate the RI sensitivity, $\left[\frac{\partial\lambda}{\partial n_{\text{polymer}}}\right]$, of PCS with various thickness of polymer on the surface, which is plotted in Figure 6-17(c). With polymer thickness increasing, the RI sensitivity increases owning to the increased filling fraction in the polymer layer. When the polymer layer is thicker than 200 nm, the plateaus for RI sensitivity is observed, since the modal field is strongly confined in the Si slab as well as polymer layer and the overlap between polymer and modal field becomes constant. With 300 nm polymer, a highest sensitivity of 120.4 nm/RIU is obtained. This sensitivity can be further improved by optimizing the lattice geometry of PCS structure and increasing the overlap between polymer and the optical field later.

To estimate the DL of single-layer PCS vapor sensor, we use equation (6.3) to calculate the RI change of polymer caused by the adsorption of vapor molecules. Taking OV-101 polymer as an example, with 100 ppm hexane vapor, the molecule density in

polymer layer of PCS sensor is estimated to be around 0.88x10^{-6} mol/cm. Using $\left[\frac{N_A \alpha}{3\varepsilon_0}\right]$ = 30.75 cm^3/mol for hexane vapor[171], the RI change of OV-101 polymer due to hexane vapor is 0.53x10^{-6} RIU/ppm. Considering a sensitivity of 120.4 nm/RIU from polymer RI change, a sensitivity of 0.064 pm/ppm for hexane vapor is derived, and hence a DL of 16 ppm. This result is 20 times higher than experimental results (a sensitivity of 3.2x10^{-3} pm/ppm and a DL of 312 ppm). The lower sensitivity from experiment is attributed to the thinner polymer coating. Since we only consider the RI change of polymer from adsorption of polymer in the calculation, the estimated DL can be further improved by considering the effect of RI change from polymer volume change and the thickness change of polymer layer due to the introduction of vapor analytes.

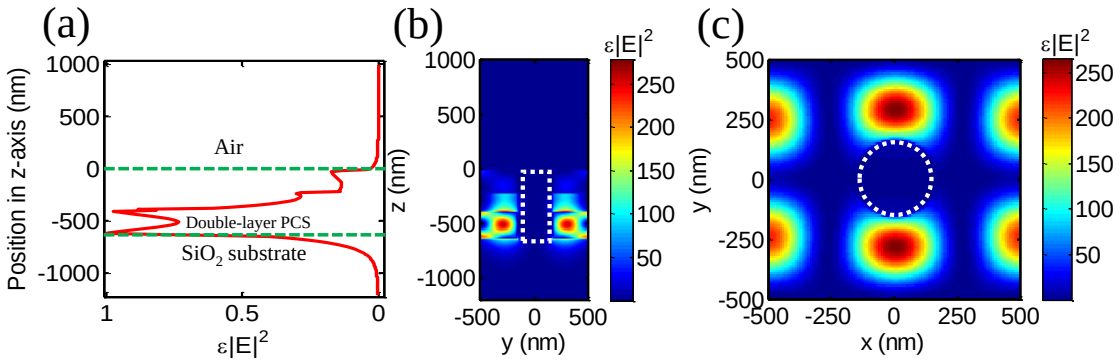

Figure 6-18 Simulated field distribution of double-layer PCS: t_T = 213 nm, t_B = 240 nm, t_b = 167 nm, a = 1,000 nm, and r = 160 nm. (a) Intensity distribution of electric filed along vertical direction (z-axis). The sensor surface is located at z = 0. (b) and (c) show the mode profile in the yz plane (x = 0) and xy plane (z = 0), respectively. Dashed lines outline the boundary of the air hole.

6.4.3 Theoretical analysis of double-layer 2D PCS vapor sensor

Similar to that of single-layer PCS in 6.4.2, both optical modal field distribution and sensitivity of double-layer PCS are studied. The modal field distribution of the investigated double-layer PCS sensor is given in Figure 6-18. Based on the integrated electric field distribution along vertical direction (*z*-axis) in Figure 6-18(a), the evanescent field above PCS surface decays exponentially, and then becomes zero at a distance of 200 nm away from PCS surface. The filling fraction above PCS surface is calculated to be 0.77%. From the field distributions in *yz* and *xy* plane shown in Figure 6-18(b) and (c), the modal field is mainly concentrated into the bottom Si slab region, resulted from the unsymmetrical structure from fabrication that the top Si layer (t_T = 213 nm) is thinner than the bottom Si layer (t_B = 240 nm). The filling fraction in air hole region is estimated to be 1.53%. Compared to the filling fraction above PCS surface, the larger filling fraction in air hole can be used for those sensing applications that the analyte could be filled into the hole region.

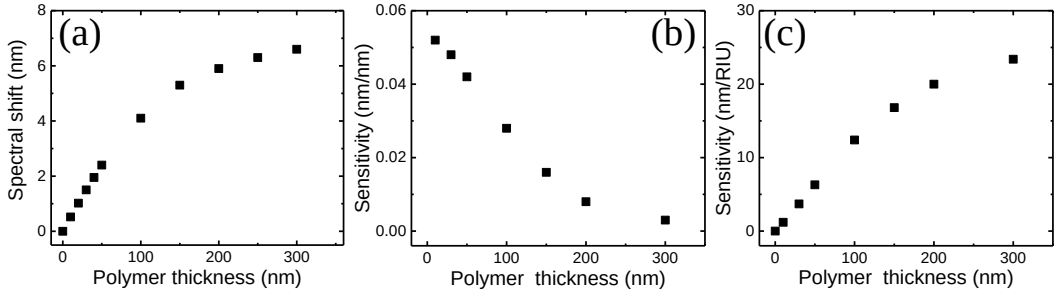

Figure 6-19 Numerical study of the sensing capability for double-layer PCS vapor sensor with polymer coating. In simulation, the RI of polymer is 1.46, and the lattice geometry of PCS is t_T = 213 nm, t_B = 240 nm, t_b = 167 nm, a = 1,000 nm, and r = 160 nm. (a) Fano resonance spectral shift as a function of polymer thickness above PCS surface. (b) Polymer thickness sensitivity as a function of polymer thickness above PCS surface. (c) RI sensitivity as a function of polymer thickness above PCS surface.

Figure 6-19(a) shows the Fano resonance spectral shift of double-layer PCS as a function of polymer thickness above PCS surface. The spectral shift increases with polymer thickness increasing and starts saturating when the polymer thickness is more than 200 nm, which is in good agreement with the calculated modal field distribution in Figure 6-18. The thickness sensitivity, $\left[\frac{\partial\lambda}{\partial t}\right]$, as a function of polymer thickness above PCS surface in Figure 6-19(b) is calculated from the slope of each data point in Figure 6-19(a). Similar to that of single-layer PCS, the polymer thickness sensitivity of double-layer PCS is always positive, and it drops gradually to zero when polymer thickness increases, which is a result of limited attenuation length of evanescent field above PCS surface. Compared to the thickness sensitivity of single-layer PCS in Figure 6-17(b), the thickness sensitivity of double-layer PCS is much smaller, due to the smaller filling fraction above the double-layer PCS surface. This thickness sensitivity of double-layer PCS can be increased by considering the filling fraction in air hole region.

The simulated RI sensitivity, $\left[\frac{\partial\lambda}{\partial n_{\text{polymer}}}\right]$, of double-layer PCS with various thickness of polymer on the surface, is shown in Figure 6-19(c). The RI sensitivity of double-layer PCS increases as polymer thickness increases, and starts saturating when the thickness of polymer is larger than 200 nm. The maximum RI sensitivity is 23.4 nm/RIU, which is calculated with 300 nm polymer on the surface. Similar to the thickness sensitivity, this RI sensitivity from double-layer PCS is much smaller than that of single-layer PCS in Figure 6-17(c), due to smaller filling fraction.

6.5 Conclusion

In this chapter, we developed vapor sensors with both single-layer and coupled double-layer PCS and explored their capability for VOCs detection. The PCS vapor sensors demonstrate fast detection and recovery time which benefits from efficient gas fluidics for sample delivery. Selective detection between hexane and ethanol vapors in experiment is achieved by coating PCS with OV-101 and PEG 1,000, respectively. The vapor sensor is fully reversible and quite stable by continuously tracking the response in three days. The DL of PCS sensor is around a few hundred ppm in terms of vapor concentration which can be further improved by coating thicker polymer. Theoretical analysis of both single-layer and double-layer PCS is also performed. It shows that the single-layer PCS sensor has much higher sensitivity than double-layer PCS sensor, resulted from different filling fraction between two kinds of sensors. Future work will focus on the single-layer PCS that shows better sensing capability from theory, and improve the coating procedure to have thicker polymer, and hence higher sensitivity as well as better DL.

Chapter 7

Summary and Future Work

7.1 Summary

In this dissertation, the background and motivation of developing ultra-compact Fano resonance 2D PCS based label-free sensing platform are presented. The theoretical principle, numerical study, fabrication technologies, and optical characterization of both single-layer and coupled double-layer PCS are described in detail. The applications of PCS for bulk liquid sensing and chemical vapor detection are explored too.

The coupling of in-plane guided resonance modes to the out-of-the-plane radiation modes in PCS provides an efficient way to channel light from within the slab to the external environment, thus making it promising for building ultra-compact and miniaturized sensor arrays on chip. The design guidelines for both single-layer and coupled double-layer PCS sensors are given based on the numerical study. Simulation results show that the single-layer PCS can have both high Q factor and high sensitivity when the thickness of PCS is 160 nm. And double-layer PCS possesses extremely high Q factor by choosing the coupling oxide layer with appropriate thickness, while the sensitivity is limited to a few tens nm/RIU. Since the DL is inversely proportional to Q factor and sensitivity, it is possible to achieve very low DL with both single-layer and coupled double-layer PCS.

The fabrication of PCS is performed with EBL and RIE process. And the optofluidic PCS sensing platform is built with soft lithography for bulk liquid sensing characterization. Single-layer PCS sensor demonstrates both high Q factor and high sensitivity, resulting in a DL of 10^{-6} RIU. For double-layer PCS, due to fabrication

challenge, the experimental Q factor is similar to that of single-layer PCS. The achievable DL of double-layer PCS sensor is around 10^{-5} RIU, which is worse than that of single-layer PCS. By optimizing the fabrication process, the Q factor of double-layer PCS can be improved, hence better DL.

For chemical vapor detection, compact gas sensing platform based on both single-layer and coupled double-layer PCS is built and evaluated with two representative vapor analytes at various concentrations. The fast response of PCS sensor to vapor analytes is demonstrated, owing to the efficient gas fluidics. The Fano resonance spectral shift shows a linear relationship with the vapor concentrations within 10^2 ppm to 10^4 ppm. High sensitivity and specificity to various analytes are realized by coating a thin layer of polymer. The experimental sensitivity to vapor analytes can be further improved by developing new polymer coating method to create thicker polymer onto the device. Moreover, the theoretical study of both single-layer and coupled double-layer PCS vapor sensor is also performed. The numerical study shows that single-layer PCS can possess very high sensitivity (more than hundred nm/RIU) due to large overlap between analytes and optical modal field, while the sensitivity of double-layer PCS is only around a few tens nm/RIU. The advantage of double-layer PCS is the high Q factor, which tends to degrade a lot in practice due to fabrication imperfections.

7.2 Suggestions for future work

Future research can focus on the following directions. First, as numerical study demonstrates that double-layer PCS can have extremely high Q factor, improvement on fabrication process can be performed, like the uniformity of PCS surface from deposition process, the shape of air hole from etching. And fabrication of PCS sensor array on single

chip can be pursued for multiplexed detection. Second, for chemical vapor sensing, the polymer coating method needs to improve in order to have thicker film on PCS, and hence higher sensitivity. Moreover, PCS sensor array with various polymer coatings can be explored for analysis of vapor mixture. Third, the work in this dissertation proves that 2D PCS have excellent sensing capability. The PCS is fabricated on SOI substrate with microfabrication technology, which is highly compatible with μGC technology. More effort can be placed on the integration with micro-fabricated GC separation columns for developing on-chip and portable μGC systems which have vast applications in environmental monitoring, healthcare, and homeland security.

References

[1] M. A. Cooper, "Optical biosensors: where next and how soon?," *Drug Discovery Today*, vol. **11**, pp. 1061-1067, 2006.

[2] M. N. Velasco-Garcia, "Optical biosensors for probing at the cellular level: A review of recent progress and future prospects," *Seminars in Cell & Developmental Biology*, vol. **20**, pp. 27-33, 2009.

[3] K. Narsaiah, S. Jha, R. Bhardwaj, R. Sharma, and R. Kumar, "Optical biosensors for food quality and safety assurance—a review," *Journal of Food Science and Technology*, vol. **49**, pp. 383-406, 2012.

[4] X. Fan, I. M. White, S. I. Shopova, H. Zhu, J. D. Suter, and Y. Sun, "Sensitive optical biosensors for unlabeled targets: A review," *Analytica Chimica Acta*, vol. **620**, pp. 8-26, 2008.

[5] M. S. Luchansky and R. C. Bailey, "High-Q Optical Sensors for Chemical and Biological Analysis," *Analytical Chemistry*, vol. **84**, pp. 793-821, 2012.

[6] G. Gauglitz, "Direct optical detection in bioanalysis: an update," *Analytical and Bioanalytical Chemistry*, vol. **398**, pp. 2363-2372, 2010.

[7] R. Narayanaswamy and O. S. Wolfbeis, Optical sensors: industrial, environmental and diagnostic applications (Springer Science & Business Media, 2004), vol. **1**.

[8] X. Michalet, S. Weiss, and M. Jäger, "Single-Molecule Fluorescence Studies of Protein Folding and Conformational Dynamics," *Chemical Reviews*, vol. **106**, pp. 1785-1813, 2006.

[9] W. Moerner, "New directions in single-molecule imaging and analysis," *Proceedings of the National Academy of Sciences*, vol. **104**, pp. 12596-12602, 2007.

[10] H. K. Hunt and A. M. Armani, "Label-free biological and chemical sensors," *Nanoscale*, vol. **2**, pp. 1544-1559, 2010.

[11] J. Homola, S. S. Yee, and G. Gauglitz, "Surface plasmon resonance sensors: review," *Sensors and Actuators B: Chemical*, vol. **54**, pp. 3-15, 1999.

[12] B. Liedberg, C. Nylander, and I. Lunström, "Surface plasmon resonance for gas detection and biosensing," *Sensors and actuators*, vol. **4**, pp. 299-304, 1983.

[13] K. Matsubara, S. Kawata, and S. Minami, "Optical chemical sensor based on surface plasmon measurement," *Applied Optics*, vol. **27**, pp. 1160-1163, 1988.

[14] R. C. Jorgenson and S. S. Yee, "A fiber-optic chemical sensor based on surface plasmon resonance," *Sensors and Actuators B: Chemical*, vol. **12**, pp. 213-220, 1993.

[15] A. A. Kruchinin and Y. G. Vlasov, "Surface plasmon resonance monitoring by means of polarization state measurement in reflected light as the basis of a DNA-probe biosensor," *Sensors and Actuators B: Chemical*, vol. **30**, pp. 77-80, 1996.

[16] S. G. Nelson, K. S. Johnston, and S. S. Yee, "High sensitivity surface plasmon resonace sensor based on phase detection," *Sensors and Actuators B: Chemical*, vol. **35**, pp. 187-191, 1996.

[17] A. Crespi, Y. Gu, B. Ngamsom, H. J. W. M. Hoekstra, C. Dongre, M. Pollnau, R. Ramponi, H. H. van den Vlekkert, P. Watts, G. Cerullo, and R. Osellame, "Three-dimensional Mach-Zehnder interferometer in a microfluidic chip for spatially-resolved label-free detection," *Lab on a Chip*, vol. **10**, pp. 1167-1173, 2010.

[18] R. G. Heideman and P. V. Lambeck, "Remote opto-chemical sensing with extreme sensitivity: design, fabrication and performance of a pigtailed integrated optical phase-

modulated Mach–Zehnder interferometer system," *Sensors and Actuators B: Chemical*, vol. **61**, pp. 100-127, 1999.

[19] A. Ymeti, J. S. Kanger, J. Greve, P. V. Lambeck, R. Wijn, and R. G. Heideman, "Realization of a multichannel integrated Young interferometer chemical sensor," *Applied Optics*, vol. **42**, pp. 5649-5660, 2003.

[20] C. A. Barrios, M. J. Bañuls, V. González-Pedro, K. B. Gylfason, B. Sánchez, A. Griol, A. Maquieira, H. Sohlström, M. Holgado, and R. Casquel, "Label-free optical biosensing with slot-waveguides," *Optics Letters*, vol. **33**, pp. 708-710, 2008.

[21] F. Warken, E. Vetsch, D. Meschede, M. Sokolowski, and A. Rauschenbeutel, "Ultra-sensitive surface absorption spectroscopy using sub-wavelength diameter optical fibers," *Optics Express*, vol. **15**, pp. 11952-11958, 2007.

[22] J.-C. Yang, J. Ji, J. M. Hogle, and D. N. Larson, "Metallic Nanohole Arrays on Fluoropolymer Substrates as Small Label-Free Real-Time Bioprobes," *Nano Letters*, vol. **8**, pp. 2718-2724, 2008.

[23] C. Fenzl, T. Hirsch, and O. S. Wolfbeis, "Photonic Crystals for Chemical Sensing and Biosensing," *Angewandte Chemie International Edition*, vol. **53**, pp. 3318-3335, 2014.

[24] J. E. Baker, R. Sriram, and B. L. Miller, "Two-dimensional photonic crystals for sensitive microscale chemical and biochemical sensing," *Lab on a Chip*, vol. **15**, pp. 971-990, 2015.

[25] Y. Sun and X. Fan, "Optical ring resonators for biochemical and chemical sensing," *Analytical and Bioanalytical Chemistry*, vol. **399**, pp. 205-211, 2011.

[26] F. Vollmer and S. Arnold, "Whispering-gallery-mode biosensing: label-free detection down to single molecules," *Nature methods*, vol. **5**, pp. 591-596, 2008.

[27] A. M. Armani, R. P. Kulkarni, S. E. Fraser, R. C. Flagan, and K. J. Vahala, "Label-free, single-molecule detection with optical microcavities," *Science*, vol. **317**, pp. 783-787, 2007.

[28] I. M. White, H. Oveys, X. Fan, T. L. Smith, and J. Zhang, "Integrated multiplexed biosensors based on liquid core optical ring resonators and antiresonant reflecting optical waveguides," *Applied Physics Letters*, vol. **89**, pp. 191106, 2006.

[29] www.biacore.com/lifesciences/index.html.

[30] Z. Yu and S. Fan, "Extraordinarily high spectral sensitivity in refractive index sensors using multiple optical modes," *Optics Express*, vol. **19**, pp. 10029-10040, 2011.

[31] P. Pfeifer, U. Aldinger, G. Schwotzer, S. Diekmann, and P. Steinrücke, "Real time sensing of specific molecular binding using surface plasmon resonance spectroscopy," *Sensors and Actuators B: Chemical*, vol. **54**, pp. 166-175, 1999.

[32] I. M. White and X. Fan, "On the performance quantification of resonant refractive index sensors," *Optics Express*, vol. **16**, pp. 1020-1028, 2008.

[33] A. Q. Liu, H. J. Huang, L. K. Chin, Y. F. Yu, and X. C. Li, "Label-free detection with micro optical fluidic systems (MOFS): a review," *Analytical and Bioanalytical Chemistry*, vol. **391**, pp. 2443-2452, 2008.

[34] C. Monat, P. Domachuk, C. Grillet, M. Collins, B. J. Eggleton, M. Cronin-Golomb, S. Mutzenich, T. Mahmud, G. Rosengarten, and A. Mitchell, "Optofluidics: a novel generation of reconfigurable and adaptive compact architectures," *Microfluidics and Nanofluidics*, vol. **4**, pp. 81-95, 2008.

[35] D. Psaltis, S. R. Quake, and C. Yang, "Developing optofluidic technology through the fusion of microfluidics and optics," *Nature*, vol. **442**, pp. 381-386, 2006.

[36] D. Erickson, D. Sinton, and D. Psaltis, "Optofluidics for energy applications," *Nature Photonics*, vol. **5**, pp. 583-590, 2011.

[37] Y.-F. Chen, L. Jiang, M. Mancuso, A. Jain, V. Oncescu, and D. Erickson, "Optofluidic opportunities in global health, food, water and energy," *Nanoscale*, vol. **4**, pp. 4839-4857, 2012.

[38] C. Monat, P. Domachuk, and B. J. Eggleton, "Integrated optofluidics: A new river of light," *Nature Photonics*, vol. **1**, pp. 106-114, 2007.

[39] S. Fan and J. D. Joannopoulos, "Analysis of guided resonances in photonic crystal slabs," *Physical Review B*, vol. **65**, pp. 235112, 2002.

[40] L. Rayleigh, "XXVI. On the remarkable phenomenon of crystalline reflexion described by Prof. Stokes," *The London, Edinburgh, and Dublin Philosophical Magazine and Journal of Science*, vol. **26**, pp. 256-265, 1888.

[41] E. Yablonovitch, "Inhibited Spontaneous Emission in Solid-State Physics and Electronics," *Physical Review Letters*, vol. **58**, pp. 2059-2062, 1987.

[42] S. John, "Strong localization of photons in certain disordered dielectric superlattices," *Physical Review Letters*, vol. **58**, pp. 2486-2489, 1987.

[43] J. D. Joannopoulos, S. G. Johnson, J. N. Winn, and R. D. Meade, Photonic crystals: molding the flow of light (Princeton university press, 2011).

[44] D. W. Prather, S. Shouyuan, J. Murakowski, G. J. Schneider, A. Sharkawy, C. Chen, and M. Binglin, "Photonic Crystal Structures and Applications: Perspective, Overview,

and Development," *Selected Topics in Quantum Electronics, IEEE Journal of*, vol. **12**, pp. 1416-1437, 2006.

[45] R. V. Nair and R. Vijaya, "Photonic crystal sensors: An overview," *Progress in Quantum Electronics*, vol. **34**, pp. 89-134, 2010.

[46] W. Zhou, D. Zhao, Y.-C. Shuai, H. Yang, S. Chuwongin, A. Chadha, J.-H. Seo, K. X. Wang, V. Liu, Z. Ma, and S. Fan, "Progress in 2D photonic crystal Fano resonance photonics," *Progress in Quantum Electronics*, vol. **38**, pp. 1-74, 2014.

[47] O. Painter, R. Lee, A. Scherer, A. Yariv, J. O'brien, P. Dapkus, and I. Kim, "Two-Dimensional Photonic Band-Gap Defect Mode Laser," *Science*, vol. **284**, pp. 1819-1821, 1999.

[48] S. Strauf, K. Hennessy, M. Rakher, Y.-S. Choi, A. Badolato, L. Andreani, E. Hu, P. Petroff, and D. Bouwmeester, "Self-Tuned Quantum Dot Gain in Photonic Crystal Lasers," *Physical Review Letters*, vol. **96**, pp. 127404, 2006.

[49] D. Zhao, A. S. Chadha, S. Liu, H. Yang, Y. Shuai, Z. Ma, and W. Zhou, "Surface-normal photonic crystal membrane reflectors with integrated inplane couplers for integrated silicon photonics," in *Photonics Conference (IPC), 2014 IEEE*, pp. 30-31, 2014.

[50] Y. Shuai, D. Zhao, Z. Tian, J.-H. Seo, D. V. Plant, Z. Ma, S. Fan, and W. Zhou, "Double-layer Fano resonance photonic crystal filters," *Optics Express*, vol. **21**, pp. 24582-24589, 2013.

[51] X. Fan and I. M. White, "Optofluidic microsystems for chemical and biological analysis," *Nature Photonics*, vol. **5**, pp. 591-597, 2011.

[52] Y. Guo, J. Y. Ye, C. Divin, B. Huang, T. P. Thomas, J. J. R. Baker, and T. B. Norris, "Real-Time Biomolecular Binding Detection Using a Sensitive Photonic Crystal Biosensor," *Analytical Chemistry*, vol. **82**, pp. 5211-5218, 2010.

[53] B. Cunningham, B. Lin, J. Qiu, P. Li, J. Pepper, and B. Hugh, "A plastic colorimetric resonant optical biosensor for multiparallel detection of label-free biochemical interactions," *Sensors and Actuators B: Chemical*, vol. **85**, pp. 219-226, 2002.

[54] B. Cunningham, P. Li, B. Lin, and J. Pepper, "Colorimetric resonant reflection as a direct biochemical assay technique," *Sensors and Actuators B: Chemical*, vol. **81**, pp. 316-328, 2002.

[55] I. D. Block, M. Pineda, C. J. Choi, and B. T. Cunningham, "High Sensitivity Plastic-Substrate Photonic Crystal Biosensor," *Sensors Journal, IEEE*, vol. **8**, pp. 1546-1547, 2008.

[56] D. Wawro, S. Zimmerman, R. Magnusson, and P. Koulen, "Photonic Sensor System for Screening Serum Biomarker Proteins in Ovarian Cancer," in *Proceedings of SPIE*, pp. 80900S, 2011.

[57] R. Magnusson, D. Wawro, S. Zimmerman, and Y. Ding, "Resonant Photonic Biosensors with Polarization-Based Multiparametric Discrimination in Each Channel," *Sensors*, vol. **11**, pp. 1476-1488, 2011.

[58] B. Lin, J. Qiu, J. Gerstenmeier, P. Li, H. Pien, J. Pepper, and B. Cunningham, "A label-free optical technique for detecting small molecule interactions," *Biosensors and Bioelectronics*, vol. **17**, pp. 827-834, 2002.

[59] R. Magnusson, "The complete biosensor," *J. Biosensors and Bioelectronics*, vol. **4**, pp. 1-2, 2013.

[60] R. Magnusson and S. S. Wang, "New principle for optical filters," *Applied Physics Letters*, vol. **61**, pp. 1022-1024, 1992.

[61] http://www.resonantsensors.com/.

[62] S. Chakravarty, Y. Zou, W.-C. Lai, and R. T. Chen, "Slow light engineering for high Q high sensitivity photonic crystal microcavity biosensors in silicon," *Biosensors and Bioelectronics*, vol. **38**, pp. 170-176, 2012.

[63] W.-C. Lai, S. Chakravarty, Y. Zou, Y. Guo, and R. T. Chen, "Slow light enhanced sensitivity of resonance modes in photonic crystal biosensors," *Applied Physics Letters*, vol. **102**, pp. 041111, 2013.

[64] E. Chow, A. Grot, L. W. Mirkarimi, M. Sigalas, and G. Girolami, "Ultracompact biochemical sensor built with two-dimensional photoniccrystal microcavity," *Optics Letters*, vol. **29**, pp. 1093-1095, 2004.

[65] M. R. Lee and P. M. Fauchet, "Nanoscale microcavity sensor for single particle detection," *Optics Letters*, vol. **32**, pp. 3284-3286, 2007.

[66] D. F. Dorfner, T. Hürlimann, T. Zabel, L. H. Frandsen, G. Abstreiter, and J. J. Finley, "Silicon photonic crystal nanostructures for refractive index sensing," *Applied Physics Letters*, vol. **93**, pp. 181103, 2008.

[67] Y. Liu and H. W. M. Salemink, "Photonic crystal-based all-optical on-chip sensor," *Optics Express*, vol. **20**, pp. 19912-19920, 2012.

[68] W.-C. Lai, S. Chakravarty, Y. Zou, and R. T. Chen, "Silicon nano-membrane based photonic crystal microcavities for high sensitivity bio-sensing," *Optics Letters*, vol. **37**, pp. 1208-1210, 2012.

[69] N. Skivesen, A. Têtu, M. Kristensen, J. Kjems, L. H. Frandsen, and P. I. Borel, "Photonic-crystal waveguide biosensor," *Optics Express*, vol. **15**, pp. 3169-3176, 2007.

[70] A. Di Falco, L. O'Faolain, and T. F. Krauss, "Chemical sensing in slotted photonic crystal heterostructure cavities," *Applied Physics Letters*, vol. **94**, pp. 063503, 2009.

[71] S. C. Buswell, V. A. Wright, J. M. Buriak, V. Van, and S. Evoy, "Specific detection of proteins using photonic crystal waveguides," *Optics Express*, vol. **16**, pp. 15949-15957, 2008.

[72] M. Lee and P. M. Fauchet, "Two-dimensional silicon photonic crystal based biosensing platform for protein detection," *Optics Express*, vol. **15**, pp. 4530-4535, 2007.

[73] M. G. Scullion, A. Di Falco, and T. F. Krauss, "Slotted photonic crystal cavities with integrated microfluidics for biosensing applications," *Biosensors and Bioelectronics*, vol. **27**, pp. 101-105, 2011.

[74] J. Jágerská, H. Zhang, Z. Diao, N. L. Thomas, and R. Houdré, "Refractive index sensing with an air-slot photonic crystal nanocavity," *Optics Letters*, vol. **35**, pp. 2523-2525, 2010.

[75] S. Zlatanovic, L. W. Mirkarimi, M. M. Sigalas, M. A. Bynum, E. Chow, K. M. Robotti, G. W. Burr, S. Esener, and A. Grot, "Photonic crystal microcavity sensor for ultracompact monitoring of reaction kinetics and protein concentration," *Sensors and Actuators B: Chemical*, vol. **141**, pp. 13-19, 2009.

[76] S. Pal, E. Guillermain, R. Sriram, B. L. Miller, and P. M. Fauchet, "Silicon photonic crystal nanocavity-coupled waveguides for error-corrected optical biosensing," *Biosensors and Bioelectronics*, vol. **26**, pp. 4024-4031, 2011.

[77] F. Hosseinibalam, S. Hassanzadeh, A. Ebnali-Heidari, and C. Karnutsch, "Design of an optofluidic biosensor using the slow-light effect in photonic crystal structures," *Applied Optics*, vol. **51**, pp. 568-576, 2012.

[78] J. García-Rupérez, V. Toccafondo, M. J. Bañuls, J. G. Castelló, A. Griol, S. Peransi-Llopis, and Á. Maquieira, "Label-free antibody detection using band edge fringes in SOI planar photonic crystal waveguides in the slow-light regime," *Optics Express*, vol. **18**, pp. 24276-24286, 2010.

[79] D. Dorfner, T. Zabel, T. Hürlimann, N. Hauke, L. Frandsen, U. Rant, G. Abstreiter, and J. Finley, "Photonic crystal nanostructures for optical biosensing applications," *Biosensors and Bioelectronics*, vol. **24**, pp. 3688-3692, 2009.

[80] T. Xu, N. Zhu, M. Y.-C. Xu, L. Wosinski, J. S. Aitchison, and H. E. Ruda, "Pillar-array based optical sensor," *Optics Express*, vol. **18**, pp. 5420-5425, 2010.

[81] C. Kang, C. T. Phare, Y. A. Vlasov, S. Assefa, and S. M. Weiss, "Photonic crystal slab sensor with enhanced surface area," *Optics Express*, vol. **18**, pp. 27930-27937, 2010.

[82] O. Levi, M. M. Lee, J. Zhang, V. Lousse, S. R. J. Brueck, S. Fan, and J. S. Harris, "Sensitivity analysis of a photonic crystal structure for index-of-refraction sensing," in *Proceedings of SPIE*, pp. 64470P64471, 2007.

[83] Y. Huang, G. Pandraud, and P. M. Sarro, "Reflectance-based two-dimensional TiO_2 photonic crystal liquid sensors," *Optics Letters*, vol. **37**, pp. 3162-3164, 2012.

[84] M. Huang, A. A. Yanik, T.-Y. Chang, and H. Altug, "Sub-wavelength nanofluidics in photonic crystal sensors," *Optics Express*, vol. **17**, pp. 24224-24233, 2009.

[85] C. Nicolaou, W. T. Lau, R. Gad, H. Akhavan, R. Schilling, and O. Levi, "Enhanced detection limit by dark mode perturbation in 2D photonic crystal slab refractive index sensors," *Optics Express*, vol. **21**, pp. 31698-31712, 2013.

[86] M. El Beheiry, V. Liu, S. Fan, and O. Levi, "Sensitivity enhancement in photonic crystal slab biosensors," *Optics Express*, vol. **18**, pp. 22702-22714, 2010.

[87] A. A. Yanik, M. Huang, A. Artar, T.-Y. Chang, and H. Altug, "Integrated nanoplasmonic-nanofluidic biosensors with targeted delivery of analytes," *Applied Physics Letters*, vol. **96**, pp. 021101, 2010.

[88] T. Cassagneau and F. Caruso, "Conjugated Polymer Inverse Opals for Potentiometric Biosensing," *Advanced Materials*, vol. **14**, pp. 1837-1841, 2002.

[89] J. Li, X. Zhao, H. Wei, Z.-Z. Gu, and Z. Lu, "Macroporous ordered titanium dioxide (TiO_2) inverse opal as a new label-free immunosensor," *Analytica Chimica Acta*, vol. **625**, pp. 63-69, 2008.

[90] S. Tian, J. Wang, U. Jonas, and W. Knoll, "Inverse Opals of Polyaniline and Its Copolymers Prepared by Electrochemical Techniques," *Chemistry of Materials*, vol. **17**, pp. 5726-5730, 2005.

[91] X. You, J. H. Pikul, W. P. King, and J. J. Pak, "Zinc oxide inverse opal enzymatic biosensor," *Applied Physics Letters*, vol. **102**, pp. 253103, 2013.

[92] D. Chanda, L. E. Abolghasemi, M. Haque, M. L. Ng, and P. R. Herman, "Multi-level diffractive optics for single laser exposure fabrication of telecom-band diamond-like 3-dimensional photonic crystals," *Optics Express*, vol. **16**, pp. 15402-15414, 2008.

[93] V. Maselli, J. R. Grenier, S. Ho, and P. R. Herman, "Femtosecond laser written optofluidic sensor: Bragg grating waveguide evanescent probing of microfluidic channel," *Optics Express*, vol. **17**, pp. 11719-11729, 2009.

[94] S. G. Johnson, S. Fan, P. R. Villeneuve, J. D. Joannopoulos, and L. A. Kolodziejski, "Guided modes in photonic crystal slabs," *Physical Review B*, vol. **60**, pp. 5751-5758, 1999.

[95] W. Zhou, Z. Ma, H. Yang, Z. Qiang, G. Qin, H. Pang, L. Chen, W. Yang, S. Chuwongin, and D. Zhao, "Flexible photonic-crystal Fano filters based on transferred semiconductor nanomembranes," *Journal of Physics D: Applied Physics*, vol. **42**, pp. 234007, 2009.

[96] S. G. Tikhodeev, A. L. Yablonskii, E. A. Muljarov, N. A. Gippius, and T. Ishihara, "Quasiguided modes and optical properties of photonic crystal slabs," *Physical Review B*, vol. **66**, pp. 045102, 2002.

[97] U. Fano, "Effects of Configuration Interaction on Intensities and Phase Shifts," *Physical Review*, vol. **124**, pp. 1866-1878, 1961.

[98] R. W. Wood, "XLII. On a remarkable case of uneven distribution of light in a diffraction grating spectrum," *The London, Edinburgh, and Dublin Philosophical Magazine and Journal of Science*, vol. **4**, pp. 396-402, 1902.

[99] A. E. Miroshnichenko, S. Flach, and Y. S. Kivshar, "Fano resonances in nanoscale structures," *Reviews of Modern Physics*, vol. **82**, pp. 2257-2298, 2010.

[100] B. Luk'yanchuk, N. I. Zheludev, S. A. Maier, N. J. Halas, P. Nordlander, H. Giessen, and C. T. Chong, "The Fano resonance in plasmonic nanostructures and metamaterials," *Nature materials*, vol. **9**, pp. 707-715, 2010.

[101] S. Fan, "Sharp asymmetric line shapes in side-coupled waveguide-cavity systems," *Applied Physics Letters*, vol. **80**, pp. 908-910, 2002.

[102] A. Taflove and S. C. Hagness, Computational electrodynamics (Artech House, 2000).

[103] L. Li, "New formulation of the Fourier modal method for crossed surface-relief gratings," *Journal of the Optical Society of America A*, vol. **14**, pp. 2758-2767, 1997.

[104] J.-M. Jin, The finite element method in electromagnetics (John Wiley & Sons, 2014).

[105] K. C. Johnson, "Coupled scalar wave diffraction theory," *Applied physics*, vol. **24**, pp. 249-260, 1981.

[106] V. Liu and S. Fan, "S^4 : A free electromagnetic solver for layered periodic structures," *Computer Physics Communications*, vol. **183**, pp. 2233-2244, 2012.

[107] V. Liu, M. Povinelli, and S. Fan, "Resonance-enhanced optical forces between coupled photonic crystal slabs," *Optics Express*, vol. **17**, pp. 21897-21909, 2009.

[108] K. S. Yee, "Numerical Solution of Initial Boundary Value Problems Involving Maxwell's Equations in Isotropic Media," *IEEE Transaction on Antennas and Propagation*, vol. **14**, pp. 302-307, 1966.

[109] A. F. Oskooi, D. Roundy, M. Ibanescu, P. Bermel, J. Joannopoulos, and S. G. Johnson, "MEEP: A flexible free-software package for electromagnetic simulations by the FDTD method," *Computer Physics Communications*, vol. **181**, pp. 687-702, 2010.

[110] J.-P. Berenger, "A perfectly matched layer for the absorption of electromagnetic waves," *Journal of Computational Physics*, vol. **114**, pp. 185-200, 1994.

[111] N. A. Mortensen, S. Xiao, and J. Pedersen, "Liquid-infiltrated photonic crystals: enhanced light-matter interactions for lab-on-a-chip applications," *Microfluidics and Nanofluidics*, vol. **4**, pp. 117-127, 2008.

[112] S. Wang, Y. Liu, D. Zhao, S. Liu, H. Yang, W. Zhou, and Y. Sun, "Label-free Sensing with Optofluidic Fano Resonance Photonic Crystal Slab," *Applied Physics Letters*, vol., pp. Submitted, 2016.

[113] T. Ochiai and K. Sakoda, "Dispersion relation and optical transmittance of a hexagonal photonic crystal slab," *Physical Review B*, vol. **63**, pp. 125107, 2001.

[114] W. Suh, M. F. Yanik, O. Solgaard, and S. Fan, "Displacement-sensitive photonic crystal structures based on guided resonance in photonic crystal slabs," *Applied Physics Letters*, vol. **82**, pp. 1999-2001, 2003.

[115] W. Suh, O. Solgaard, and S. Fan, "Displacement sensing using evanescent tunneling between guided resonances in photonic crystal slabs," *Journal of Applied Physics*, vol. **98**, pp. 033102, 2005.

[116] http://www.soitec.com/en/index.php.

[117] S. Wolf and R. N. Tauber, Silicon Process for the VLSI Era: Process Technology (Lattice Press, 1986), vol. **1**.

[118] M. A. Vyvoda, H. Lee, M. V. Malyshev, F. P. Klemens, M. Cerullo, V. M. Donnelly, D. B. Graves, A. Kornblit, and J. T. C. Lee, "Effects of plasma conditions on the shapes of features etched in Cl2 and HBr plasmas. I. Bulk crystalline silicon etching," *Journal of Vacuum Science & Technology A*, vol. **16**, pp. 3247-3258, 1998.

[119] Y. Xia and G. M. Whitesides, "SOFT LITHOGRAPHY," *Annual review of materials science*, vol. **28**, pp. 153-184, 1998.

[120] H. Yang, P. Deschatelets, S. T. Brittain, and G. M. Whitesides, "Fabrication of High Performance Ceramic Microstructures from a Polymeric Precursor Using Soft Lithography," *Advanced Materials*, vol. **13**, pp. 54-58, 2001.

[121] E. J. Staples and S. Viswanathan, "Ultrahigh-speed chromatography and virtual chemical sensors for detecting explosives and chemical warfare agents," *Sensors Journal, IEEE*, vol. **5**, pp. 622-631, 2005.

[122] F. L. Dorman, J. J. Whiting, J. W. Cochran, and J. Gardea-Torresdey, "Gas Chromatography," *Analytical Chemistry*, vol. **82**, pp. 4775-4785, 2010.

[123] G. A. Eiceman, J. Gardea-Torresdey, F. Dorman, E. Overton, A. Bhushan, and H. P. Dharmasena, "Gas Chromatography," *Analytical Chemistry*, vol. **78**, pp. 3985-3996, 2006.

[124] P. R. Lewis, R. P. Manginell, D. R. Adkins, R. J. Kottenstette, D. R. Wheeler, S. S. Sokolowski, D. E. Trudell, J. E. Byrnes, M. Okandan, and J. M. Bauer, "Recent advancements in the gas-phase MicroChemLab," *Sensors Journal, IEEE*, vol. **6**, pp. 784-795, 2006.

[125] http://www.defiant-tech.com/canarythree.php.

[126] M. Penza, P. Aversa, G. Cassano, W. Wlodarski, and K. Kalantar-Zadeh, "Layered SAW gas sensor with single-walled carbon nanotube-based nanocomposite coating," *Sensors and Actuators B: Chemical*, vol. **127**, pp. 168-178, 2007.

[127] M. Penza and G. Cassano, "Application of principal component analysis and artificial neural networks to recognize the individual VOCs of methanol/2-propanol in a binary mixture by SAW multi-sensor array," *Sensors and Actuators B: Chemical*, vol. **89**, pp. 269-284, 2003.

[128] M. C. Lonergan, E. J. Severin, B. J. Doleman, S. A. Beaber, R. H. Grubbs, and N. S. Lewis, "Array-based vapor sensing using chemically sensitive, carbon black-polymer resistors," *Chemistry of Materials*, vol. **8**, pp. 2298-2312, 1996.

[129] M. A. Ryan, A. V. Shevade, H. Zhou, and M. L. Homer, "Polymer–Carbon Black Composite Sensors in an Electronic Nose for Air-Quality Monitoring," *MRS bulletin*, vol. **29**, pp. 714-719, 2004.

[130] E. Covington, F. I. Bohrer, C. Xu, E. T. Zellers, and C. Kurdak, "Densely integrated array of chemiresistor vapor sensors with electron-beam patterned monolayer-protected gold nanoparticle interface films," *Lab on a Chip*, vol. **10**, pp. 3058-3060, 2010.

[131] T. Someya, J. Small, P. Kim, C. Nuckolls, and J. T. Yardley, "Alcohol Vapor Sensors Based on Single-Walled Carbon Nanotube Field Effect Transistors," *Nano Letters*, vol. **3**, pp. 877-881, 2003.

[132] J. Hodgkinson and R. P. Tatam, "Optical gas sensing: a review," *Measurement Science and Technology*, vol. **24**, pp. 012004, 2013.

[133] C.-S. Cheng, Y.-Q. Chen, and C.-J. Lu, "Organic vapour sensing using localized surface plasmon resonance spectrum of metallic nanoparticles self assemble monolayer," *Talanta*, vol. **73**, pp. 358-365, 2007.

[134] C. de Julián Fernández, M. G. Manera, G. Pellegrini, M. Bersani, G. Mattei, R. Rella, L. Vasanelli, and P. Mazzoldi, "Surface plasmon resonance optical gas sensing of nanostructured ZnO films," *Sensors and Actuators B: Chemical*, vol. **130**, pp. 531-537, 2008.

[135] Y.-Q. Chen and C.-J. Lu, "Surface modification on silver nanoparticles for enhancing vapor selectivity of localized surface plasmon resonance sensors," *Sensors and Actuators B: Chemical*, vol. **135**, pp. 492-498, 2009.

[136] J. M. Bingham, J. N. Anker, L. E. Kreno, and R. P. Van Duyne, "Gas Sensing with High-Resolution Localized Surface Plasmon Resonance Spectroscopy," *Journal of the American Chemical Society*, vol. **132**, pp. 17358-17359, 2010.

[137] R. P. Podgorsek and H. Franke, "Selective optical detection of aromatic vapors," *Applied Optics*, vol. **41**, pp. 601-608, 2002.

[138] M. Buric, K. P. Chen, M. Bhattarai, P. R. Swinehart, and M. Maklad, "Active Fiber Bragg Grating Hydrogen Sensors for All-Temperature Operation," *Photonics Technology Letters, IEEE*, vol. **19**, pp. 255-257, 2007.

[139] K. Schroeder, W. Ecke, and R. Willsch, "Optical fiber Bragg grating hydrogen sensor based on evanescent-field interaction with palladium thin-film transducer," *Optics and Lasers in Engineering*, vol. **47**, pp. 1018-1022, 2009.

[140] Y. Wu, B. Yao, A. Zhang, Y. Rao, Z. Wang, Y. Cheng, Y. Gong, W. Zhang, Y. Chen, and K. S. Chiang, "Graphene-coated microfiber Bragg grating for high-sensitivity gas sensing," *Optics Letters*, vol. **39**, pp. 1235-1237, 2014.

[141] J. Zhang, X. Tang, J. Dong, T. Wei, and H. Xiao, "Zeolite thin film-coated long period fiber grating sensor for measuring trace organic vapors," *Sensors and Actuators B: Chemical*, vol. **135**, pp. 420-425, 2009.

[142] T. L. Lowder, J. D. Gordon, S. M. Schultz, and R. H. Selfridge, "Volatile organic compound sensing using a surface-relief D-shaped fiber Bragg grating and a polydimethylsiloxane layer," *Optics Letters*, vol. **32**, pp. 2523-2525, 2007.

[143] Y. Wu, B. C. Yao, A. Q. Zhang, X. L. Cao, Z. G. Wang, Y. J. Rao, Y. Gong, W. Zhang, Y. F. Chen, and K. S. Chiang, "Graphene-based D-shaped fiber multicore mode interferometer for chemical gas sensing," *Optics Letters*, vol. **39**, pp. 6030-6033, 2014.

[144] J. D. Gordon, T. L. Lowder, R. H. Selfridge, and S. M. Schultz, "Optical D-fiber-based volatile organic compound sensor," *Applied Optics*, vol. **46**, pp. 7805-7810, 2007.

[145] V. M. N. Passaro, F. Dell'Olio, and F. De Leonardis, "Ammonia Optical Sensing by Microring Resonators," *Sensors*, vol. **7**, pp. 2741-2749, 2007.

[146] S. I. Shopova, I. M. White, Y. Sun, H. Zhu, X. Fan, G. Frye-Mason, A. Thompson, and S.-j. Ja, "On-Column Micro Gas Chromatography Detection with Capillary-Based Optical Ring Resonators," *Analytical Chemistry*, vol. **80**, pp. 2232-2238, 2008.

[147] Y. Sun, S. I. Shopova, G. Frye-Mason, and X. Fan, "Rapid chemical-vapor sensing using optofluidic ring resonators," *Optics Letters*, vol. **33**, pp. 788-790, 2008.

[148] N. A. Yebo, P. Lommens, Z. Hens, and R. Baets, "An integrated optic ethanol vapor sensor based on a silicon-on-insulator microring resonator coated with a porous ZnO film," *Optics Express*, vol. **18**, pp. 11859-11866, 2010.

[149] Y. Sun and X. Fan, "Analysis of ring resonators for chemical vapor sensor development," *Optics Express*, vol. **16**, pp. 10254-10268, 2008.

[150] G. Z. Xiao, A. Adnet, Z. Zhang, F. G. Sun, and C. P. Grover, "Monitoring changes in the refractive index of gases by means of a fiber optic Fabry-Perot interferometer sensor," *Sensors and Actuators A: Physical*, vol. **118**, pp. 177-182, 2005.

[151] K. Reddy, Y. Guo, J. Liu, W. Lee, M. K. K. Oo, and X. Fan, "On-chip Fabry–Pérot interferometric sensors for micro-gas chromatography detection," *Sensors and Actuators B: Chemical*, vol. **159**, pp. 60-65, 2011.

[152] K. Reddy and X. Fan, "Self-referenced composite Fabry-Pérot cavity vapor sensors," *Optics Express*, vol. **20**, pp. 966-971, 2012.

[153] L. Niu, C.-L. Zhao, J. Kang, S. Jin, J. Guo, and H. Wei, "A chemical vapor sensor based on Rayleigh scattering effect in simplified hollow-core photonic crystal fibers," *Optics Communications*, vol. **313**, pp. 243-247, 2014.

[154] J. Villatoro, M. P. Kreuzer, R. Jha, V. P. Minkovich, V. Finazzi, G. Badenes, and V. Pruneri, "Photonic crystal fiber interferometer for chemical vapor detection with high sensitivity," *Optics Express*, vol. **17**, pp. 1447-1453, 2009.

[155] D. Monzón-Hernández, V. P. Minkovich, J. Villatoro, M. P. Kreuzer, and G. Badenes, "Photonic crystal fiber microtaper supporting two selective higher-order modes with high sensitivity to gas molecules," *Applied Physics Letters*, vol. **93**, pp. 081106, 2008.

[156] A. M. R. Pinto and M. Lopez-Amo, "Photonic Crystal Fibers for Sensing Applications," *Journal of Sensors*, vol. **2012**, pp. Article ID 598178, 2012.

[157] F. Yang, W. Jin, Y. Cao, H. L. Ho, and Y. Wang, "Towards high sensitivity gas detection with hollow-core photonic bandgap fibers," *Optics Express*, vol. **22**, pp. 24894-24907, 2014.

[158] D. K. C. Wu, B. T. Kuhlmey, and B. J. Eggleton, "Ultrasensitive photonic crystal fiber refractive index sensor," *Optics Letters*, vol. **34**, pp. 322-324, 2009.

[159] Y. Hoo, W. Jin, H. L. Ho, D. Wang, and R. S. Windeler, "Evanescent-wave gas sensing using microstructure fiber," *Optical Engineering*, vol. **41**, pp. 8-9, 2002.

[160] A. M. Cubillas, M. Silva-Lopez, J. M. Lazaro, O. M. Conde, M. N. Petrovich, and J. M. Lopez-Higuera, "Methane detection at 1670-nm band using a hollow-core photonic bandgap fiber and a multiline algorithm," *Optics Express*, vol. **15**, pp. 17570-17576, 2007.

[161] L. Kornaszewski, N. Gayraud, J. M. Stone, W. N. MacPherson, A. K. George, J. C. Knight, D. P. Hand, and D. T. Reid, "Mid-infrared methane detection in a photonic bandgap fiber using a broadband optical parametric oscillator," *Optics Express*, vol. **15**, pp. 11219-11224, 2007.

[162] T. Ritari, J. Tuominen, H. Ludvigsen, J. C. Petersen, T. Sørensen, T. P. Hansen, and H. R. Simonsen, "Gas sensing using air-guiding photonic bandgap fibers," *Optics Express*, vol. **12**, pp. 4080-4087, 2004.

[163] K. S. Lee, Y. K. Lee, and S. H. Jang, "A Novel Grating Modulation Technique for Photonic Bandgap Fiber Gas Sensors," *Photonics Technology Letters, IEEE*, vol. **23**, pp. 624-626, 2011.

[164] J. Henningsen, J. Hald, and J. C. Peterson, "Saturated absorption in acetylene and hydrogen cyanide in hollow-core photonic bandgap fibers," *Optics Express*, vol. **13**, pp. 10475-10482, 2005.

[165] R. Thapa, K. Knabe, M. Faheem, A. Naweed, O. L. Weaver, and K. L. Corwin, "Saturated absorption spectroscopy of acetylene gas inside large-core photonic bandgap fiber," *Optics Letters*, vol. **31**, pp. 2489-2491, 2006.

[166] W.-C. Lai, S. Chakravarty, X. Wang, C. Lin, and R. T. Chen, "On-chip methane sensing by near-IR absorption signatures in a photonic crystal slot waveguide," *Optics Letters*, vol. **36**, pp. 984-986, 2011.

[167] H. Clevenson, P. Desjardins, X. Gan, and D. Englund, "High sensitivity gas sensor based on high-Q suspended polymer photonic crystal nanocavity," *Applied Physics Letters*, vol. **104**, pp. 241108, 2014.

[168] R. C. Bailey and J. T. Hupp, "Micropatterned Polymeric Gratings as Chemoresponsive Volatile Organic Compound Sensors: Implications for Analyte Detection and Identification via Diffraction-Based Sensor Arrays," *Analytical Chemistry*, vol. **75**, pp. 2392-2398, 2003.

[169] A. M. Cubillas, J. M. Lazaro, O. M. Conde, M. N. Petrovich, and J. M. Lopez-Higuera, "Gas Sensor Based on Photonic Crystal Fibres in the $2\nu_3$ and $\nu_2 + 2\nu_3$ Vibrational Bands of Methane," *Sensors*, vol. **9**, pp. 6261-6272, 2009.

[170] S. Wang, Y. Liu, D. Zhao, H. Yang, W. Zhou, and Y. Sun, "On-chip Chemical-vapor Sensing with Fano Resonance Photonic Crystal Slab," *Optics Letters*, vol., pp. Submitted, 2016.

[171] D. R. Lide, CRC handbook of chemistry and physics (CRC press, 2004).

Biographical Information

Shuling Wang was born in Xuzhou, China, in 1988. She received her Bachelor's degree in Electrical Engineering from University of Shanghai for Science and Technology, China, in 2009. She joined the Department of Electrical Engineering at University of Texas at Arlington in Fall 2010 as a Ph.D. candidate. Shuling got training on the fabrication of optoelectronic device with semiconductor materials in Professor Weidong Zhou's lab from Fall 2010 to Summer 2013, and then she joined Professor Yuze (Alice) Sun's lab in Fall 2013. Her research focused on photonic crystal based optofluidic platform for label-free biochemical detection and gas sensing. Shuling received her Ph.D. degree in Electrical Engineering from University of Texas at Arlington in 2016.

Shuling's research interest includes integrated Si photonics, optoelectronic and optofluidic devices. She is a student member of Optical Society of American. She plans to pursue a career in the product development of novel integrated optoelectronic and optofluidic devices for lab-on-a-chip applications.